GROWTH, CHARACTERIZATION AND DEVICE APPLICATIONS OF
CADMIUM ZINC TELLURIDE THIN FILMS

A THESIS SUBMITTED TO
THE GRADUATE SCHOOL OF NATURAL AND APPLIED SCIENCES
OF
MIDDLE EAST TECHNICAL UNIVERSITY

BY

ÇİĞDEM DOĞRU BALBAŞI

IN PARTIAL FULFILLMENT OF THE REQUIREMENTS
FOR
THE DEGREE OF DOCTOR OF PHILOSOPHY
IN
PHYSICS

MAY 2022

Approval of the thesis:

GROWTH, CHARACTERIZATION AND DEVICE APPLICATIONS OF CADMIUM ZINC TELLURIDE THIN FILMS

submitted by **ÇİĞDEM DOĞRU BALBAŞI** in partial fulfillment of the requirements for the degree of **Doctor of Philosophy in Physics, Middle East Technical University** by,

Prof. Dr. Halil Kalıpçılar
Dean, Graduate School of **Natural and Applied Sciences** _____

Prof. Dr. Seçkin Kürkcüoğlu
Head of the Department, **Physics** _____

Prof. Dr. Mehmet Parlak
Supervisor, **Physics, METU** _____

Examining Committee Members:

Prof. Dr. Ayşe Çiğdem Erçelebi
Physics, METU _____

Prof. Dr. Mehmet Parlak
Physics, METU _____

Prof. Dr. Bülent Akınoğlu
Physics, METU _____

Prof. Dr. Nurdan Demirci Sankır
Materials Science and Nanotechnology Engineering,
TOBB ETU _____

Assoc. Prof. Dr. Tahir Çolakoğlu
Physics Engineering, Ankara University _____

Date: 25.05.2022

I hereby declare that all information in this document has been obtained and presented in accordance with academic rules and ethical conduct. I also declare that, as required by these rules and conduct, I have fully cited and referenced all material and results that are not original to this work.

Name Last name : Çiğdem Doğru Balbaşı

Signature :

ABSTRACT

**GROWTH, CHARACTERIZATION AND DEVICE APPLICATIONS OF
CADMIUM ZINC TELLURIDE THIN FILMS**

Balbaşı Doğru, Çiğdem
Doctor of Philosophy, Physics
Supervisor: Prof. Dr. Mehmet Parlak

May 2022, 150 pages

CdZnTe is an II-VI group semiconductor material with significant properties used in many critical industrial applications, such as photovoltaic devices, photodiodes, photoconductors, room temperature gamma-ray spectroscopy, X-ray imaging, and infrared detectors. In Particular, CdZnTe is a promising material for solar cell application as an absorber layer due to its direct tunable bandgap property, high atomic number with strong absorption, excellent optoelectronic properties, and long-term stability. However, manufacturing CdZnTe-based solar cells has been a challenge, with minimum improvement recorded over the years. Therefore, four main topics about CdZnTe thin films were studied in this dissertation: (a) growth mechanism and material optimization of CdZnTe thin films by using various investigative characterization techniques, (b) understanding the surface and interface chemical compositional properties and optical dielectric response of CdZnTe thin films, (c) fabrication and electrical characterization of CdS/CdZnTe device structure with thin absorber layer (<2.0 μm) deposited at low substrate temperatures with reduced post-deposition processes, and (d) a detailed electrical analysis of the CdZnTe/Si structure for possible device applications.

In this dissertation, high-quality CdZnTe thin films were fabricated using a thermal evaporation method with uniform component distribution, which was controlled by utilizing CdZnTe single crystal pieces as source material. Additionally, post-deposition processes such as annealing and $CdCl_2$ treatment steps were applied. As a result, improved material properties and enhanced device performance of CdZnTe thin films were obtained. After a careful characterization of material and surface properties, thin heterojunction CdS/CdZnTe and CdZnTe/Si devices were fabricated successfully. It is worth noting that semitransparent thin CdZnTe films (≤2.0 µm) had a transmittance value greater than 75% in the near-infrared region, around 1000 nm. Finally, the operation and performance of the CdZnTe-based devices were investigated, and challenges encountered in the development of these devices were explained in detail.

ÖZ

KADMİYUM ÇİNKO TELLÜR İNCE FİLMLERİN BÜYÜTÜLMESİ, KARAKTERİZASYONU VE AYGIT UYGULAMALARI

Balbaşı Doğru, Çiğdem
Doktora, Fizik
Tez Yöneticisi: Prof. Dr. Mehmet Parlak

Mayıs 2022, 150 sayfa

CdZnTe, fotovoltaik aygıtlar, foto diyotlar, fotoiletkenler, oda sıcaklığında çalışan gama ışını spektroskopisi, X-ışını görüntüleme ve kızıl ötesi detektörler gibi birçok kritik endüstriyel uygulamada kullanılmasını sağlayan önemli özelliklere sahip, II-VI grubu yarı iletken malzemedir. Doğrudan ayarlanabilen bant aralığı, güçlü soğurma özelliği, yüksek atom numarasına sahip olması, mükemmel optoelektronik özellikleri ve uzun vadeli dayanıklılığı nedeniyle CdZnTe, özellikle güneş pili uygulamalarında soğurucu katman olarak oldukça umut verici bir malzemedir. Fakat, CdZnTe malzemesinin güneş pili uygulamaları göz önüne alındığında, yıllar içerisinde kaydedilen azami miktardaki gelişmeler ile oldukça zorlayıcı bir çalışma olduğu görülmüştür. Buna bağlı olarak, bu tezde CdZnTe ince filmler ile ilgili dört ana konu incelenmiştir: (a) CdZnTe ince filmlerinin farklı karakterizasyon yöntemleri kullanılarak büyütme mekanizmasının ve malzeme optimizasyonunun incelenmesi, (b) CdZnTe ince filmlerin yüzeyinin ve ara yüzeyin kimyasal bileşim özelliklerinin ve optiksel dielektrik tepkisinin incelenmesi, (c) düşük taban sıcaklıkları altında ve kaplama sonrası uygulanan işlemlerin azaltılmasıyla elde edilen ince (<2.0 μm) soğurucu katmana sahip CdS/CdZnTe aygıtların

karakterizasyonu, ve (d) CdZnTe/Si yapısının üretilmesi ve elektriksel özelliklerinin detaylı analizinin yapılması.

Bu çalışmada, yüksek kaliteye ve homojen bileşen oranlarına sahip CdZnTe ince filmler, CdZnTe tek kristal parçaları kullanılarak termal buharlaştırma yöntemi ile üretilmiştir. Kaplama sonrası, ısıl tavlama ve $CdCl_2$ uygulaması gibi işlemler yapılarak, CdZnTe ince filmlerin malzeme özellikleri ve aygıtların performansları iyileştirilmiştir. Malzeme ve yüzey özelliklerinin detaylı incelemesinden sonra, oldukça ince bir film kalınlığına sahip CdS/CdZnTe ve CdZnTe/Si heteroeklem aygıtların üretimi başarıyla gerçekleştirilmiştir. Yarı geçirgen ince CdZnTe filmlerinin ($\leq$2.0 µm), yakın-kızılötesi bölgede (yaklaşık 1000 nm'de) %75'ten daha yüksek bir geçirgenlik değerine sahip olduğunu belirtmek gerekmektedir. Son olarak, CdZnTe tabanlı aygıtların çalışması ve performansı araştırılmış ve bu aygıtların geliştirilmesi esnasında karşılaşılan zorluklar detaylı bir şekilde açıklanmıştır.

Anahtar Kelimeler: CdZnTe, İnce film, Soğurucu Katman, Güneş Hücresi, Heteroeklem Diyot.

To my father

ACKNOWLEDGMENTS

First and foremost, I would like to express my sincere gratitude to my advisor, Prof. Dr. Mehmet Parlak, for his endless patience, excellent guidance, understanding, cooperation, encouragement, and continuous support throughout this study. Working under his guidance and sharing his knowledge was a great honor and privilege. His trust and confidence in me pushed me to achieve more and forced me to have confidence in myself. I would also like to thank members of the thesis monitoring committee, Prof. Dr. Ayşe Çiğdem Erçelebi and Prof. Dr. Nurdan Demirci Sankır, for their valuable discussions and comments in addition to their support and inspiration. I would like to thank my committee members Prof. Dr. Bülent Akınoğlu and Assoc. Prof. Dr. Tahir Çolakoğlu.

I am blessed with many fantastic people in our group, colleagues of smart and funny people: Dr. Makbule Terlemezoğlu, Dr. Özge Sürücü, Assoc. Dr. Hasan Hüseyin Güllü, Merve Demir, and Tunç Bektaş. Thank you for your sincere friendship, collaboration, valuable discussion, and experimental knowledge. I would also like to thank all other GÜNAM members.

Special thanks to my best friend and love of my life Özden Başar Balbaşı for his infinite love, kindness, and support. He is my rock and has been with me through every step. I thank Özden for sharing everything with me these past ten years. He has read and edited just about everything I have ever written. Özden has always believed in me more than I ever believed in myself and pushed me to achieve more. He is always there for me, believing in me, keeping me motivated, and cheering me up all the time. I am a stronger and better person because of him. I cannot wait to see what our future brings.

Last but not least, I would like to thank my family for their unconditional love, endless support, and encouragement. My parents raised me to be inquisitive and stay ambitious and goal-oriented.

TABLE OF CONTENTS

xii

LIST OF TABLES

LIST OF FIGURES

FIGURES

LIST OF ABBREVIATIONS

CdTe	Cadmium Telluride
ZnTe	Zinc Telluride
CdZnTe	Cadmium Zinc Telluride
CdS	Cadmium Sulfide
Si	Silicon
XRD	X-Ray Diffraction
XPS	X-Ray Photoelectron Spectroscopy
FWHM	Full Width at Half Maxima
AFM	Atomic Force Microscopy
EDS	Energy Dispersive X-ray Spectroscopy
SEM	Scanning Electron Microscope
I-V	Current-Voltage
C-V	Capacitance-Voltage
G-V	Conductance-Voltage
FF	Fill Factor
GD	Gaussian Distribution
TE	Thermionic Emission
C_{HF}-C_{LF}	High-Low Frequency Capacitance
D_{it}	Interface Trap Density
DC	Direct Current

LIST OF SYMBOLS

$\alpha(E)$ Absorption Coefficient

$q\phi_m$ Metal Work function

$q\phi_S$ Semiconductor Work Function

Φ_{B0} Zero-Bias Barrier Height

$\overline{\Phi}_{B0}$ Mean Zero-Bias Barrier Height

σ_0 Zero-Bias Standard Deviation

χ Electron affinity

E_F Fermi Level

E_g Bandgap Energy

ε_0 Vacuum Permittivity

ε_s Semiconductor Dielectric Constant

$n(E)$ Refractive Index

$k(E)$ Extinction Coefficient

$\varepsilon(E)$ Complex Dielectric Constant

I_0 Reverse Saturation Current

J_{sc} Short-Circuit Current Density

V_{oc} Open-Circuit Voltage

R_s Series Resistance

R_{sh} Shunt Resistance

n   Diode Ideality Factor

CHAPTER 1

INTRODUCTION

Semiconductor materials and devices have been extensively utilized in a variety of applications involving science, astronomy, medical, defense, and commercial products, and they have become principal components for modern technologies. The manufacturing of binary and ternary compound semiconductors enables the possibility of tailoring the material properties in accordance with a particular function of a device. A tremendous number of fields that use compound semiconductor devices include photovoltaic solar cells, radiation technology, and electronics.

Among compound semiconductors, II-VI group semiconductor materials have been a focus of interest in terms of solar energy conversion due to their tunable bandgap energy properties and excellent optical conversion efficiencies [1]. In particular, CdTe is a unique II-VI group compound with the highest average atomic number, the largest lattice parameter, the highest ionicity, the minimum negative enthalpy of formation, and the lowest melting point temperature [2], [3]. In addition, CdTe is a direct optical band gap ($E_g = 1.5 \ eV$) semiconductor and has high absorption coefficient ($> 5 \times 10^5 /cm$), resulting with a high quantum yield over a wide range of wavelength in solar spectrum that makes CdTe an ideal candidate for photovoltaic energy conversion in the field of thin films [4], [5]. CdTe-based devices are also suitable for applications beyond terrestrial power conversion, such as space-power generation, gamma radiation detectors, and infrared detectors [5]. Figure 1.1 compares the theoretical solar cell efficiency for CdTe and the absorption coefficient with respect to bandgap energy for photovoltaic thin film materials [5].
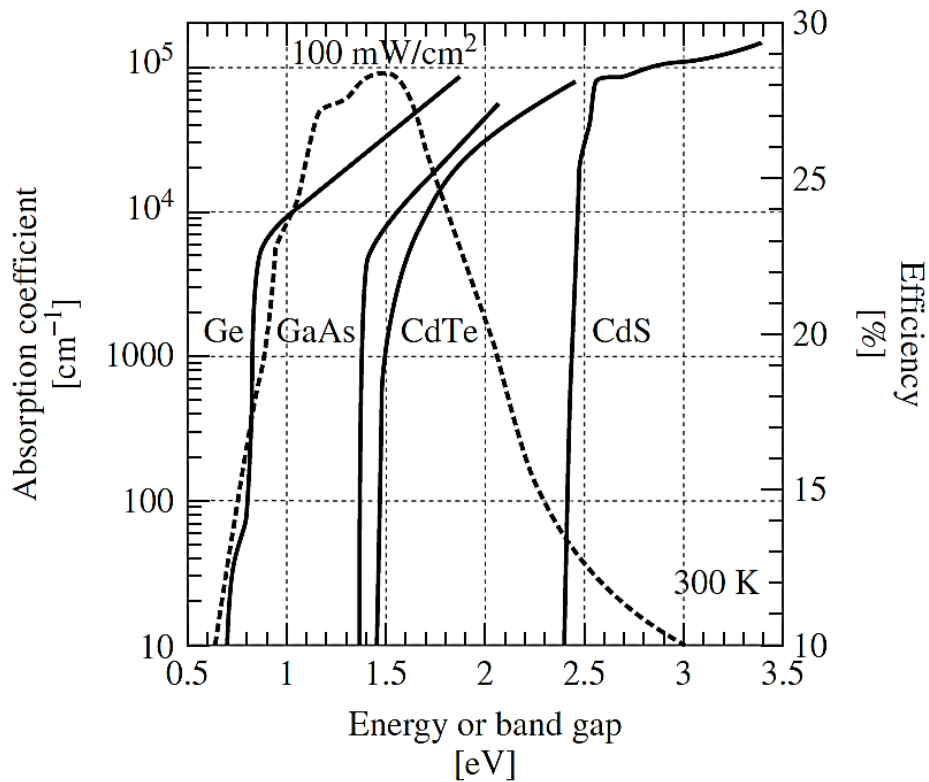
Figure 1.1. The theoretical solar cell efficiency of CdTe (dotted line) for AM1.5 and absorption coefficient vs. bandgap energy for photovoltaic thin film materials, from [5].

CdTe is the prominent material for thin-film-based photovoltaic devices with a major industrial power on energy production. Large-area CdTe thin film solar cells show long-lasting stability, have high conversion efficiency, and attract production-scale investments [6]. Indeed, Figure 1.2 shows the National Renewable Energy Laboratory (NREL) cell efficiency chart for a range of photovoltaic technologies, including CdTe thin film solar cell, which reaches an efficiency record of 22.1% for lab-made solar cells by First Solar [7].
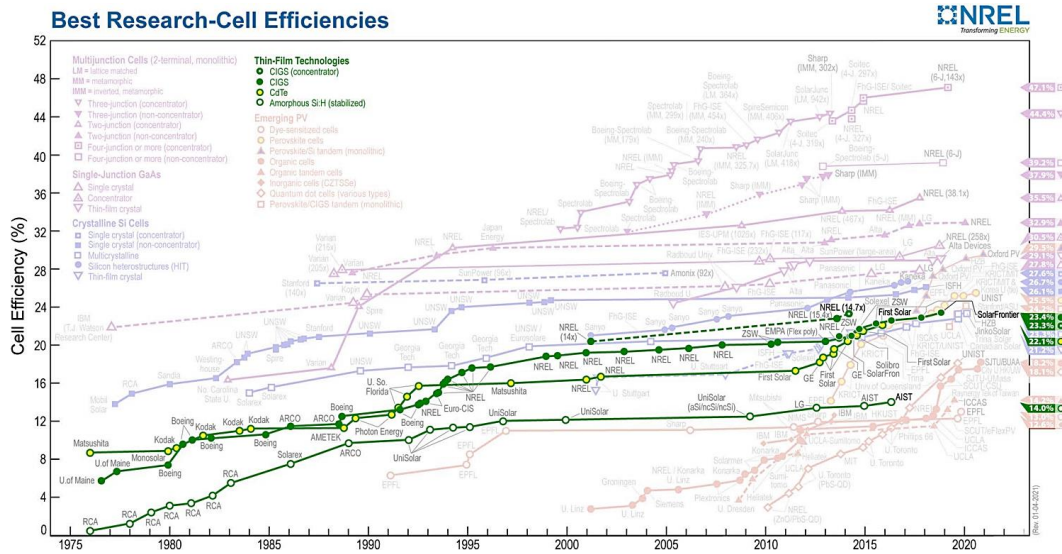
Figure 1.2. NREL cell efficiency chart for thin film technologies, from [7].

Although CdTe is one of the main compounds in the photovoltaic industry, it can also be alloyed with other II-VI semiconductors to tailor its bandgap, which allows it to be used in a wide range of various optoelectronic fields. Different alloy compositions introduce entirely new opportunities [5]. The addition of Zn to CdTe, resulting in the ternary compound cadmium zinc telluride ($Cd_{1-x}Zn_xTe$ or CdZnTe), improves the quality of the material and makes p-type doping much easier [8], [9]. Alloy systems separated by Cd and Zn cation and Te anion substitution in pseudobinary compounds allow a wide range of optical bandgaps by tailoring the material properties, resulting CdZnTe being suitable as absorber layers in terrestrial photovoltaic heterojunction devices. Obtained isostructural Cadmium Zinc Telluride system offers tunable properties with a broad range of band gaps and controllable *p*-type conductivity [5]. CdZnTe has excellent optoelectronic properties and it can be used in many important applications, such as photovoltaic devices [10]–[13], photodiodes [14], photoconductors [15], room temperature gamma-ray spectroscopy [16], [17], X-ray imaging [16], [18], and light-emitting diodes [19].

1.1   Cadmium Zinc Telluride (CdZnTe)

CdZnTe is an iconic II-VI semiconductor material that has extremely important properties enabling it to be used for many critical industrial applications. Its direct tunable bandgap properties (ranging from semi-metallic to wide bandgap), high atomic numbers (Cd:48, Zn:30, Te:52), long-term stability, and the possibilities of various lattice parameters allow CdZnTe to be available for fabrication of both light sources and detectors [20]. In this section, the properties of CdTe, ZnTe, and $Cd_{1-x}Zn_xTe$ are provided in detail, especially the variation of compound parameters regarding the composition parameter "*x*". Structural properties, thermal, optical, and mechanical parameters, and electronic transport properties of CdTe, ZnTe, and $Cd_{1-x}Zn_xTe$ semiconductors are tabulated in Table 1.1.

Table 1.1 The physicochemical and optoelectronic parameters of CdTe, ZnTe, and CdZnTe compound semiconductor materials at 300 K [1], [21], [22].

Material property	*CdTe*	*ZnTe*	*$Cd_{1-x}Zn_xTe$*
Structure	Zincblende	Zincblende	Zincblende
Space group	$F\bar{4}3m$	$F\bar{4}3m$	$F\bar{4}3m$
Lattice constant a (nm)	0.648	0.610	0.648-0.038x
Energy gap Eg (eV)	1.475	2.394	$1.74x^2 - 1.01x + 1.51$
Density g (gm/cm^3)	5.856	5.637	5.856-0.219x
Melting Point (°C)	1092	1295	$1092+30x+173x^2$
Ionicity	0.717	0.609	0.710-0.101x
Specific heat (J/(gK))	0.211	0.258	0.211+0.047x
Thermal conductivity (W//gK))	0.08	0.18	$1/(13.3+61.1x-68.8x^2)$
Static dielectric constant ε_s	10.4	9.4	10.4-1.0x
High-frequency dielectric constant ε_∞	7.1	6.9	7.1-0.2x
Electron Hall mobility μ_e (cm^2/(Vs))	1550	600	1550-950x
Hole Hall mobility μ_h (cm^2/(Vs))	104	100	$104-164x+160x^2$

1.1.1 Crystal Structure

$Cd_{1-x}Zn_xTe$ semiconductor alloy is composed of $(CdTe)_{1-x}$ and $(ZnTe)_x$ materials in a proper ratio according to the application to be used. CdZnTe has a zincblende atomic arrangement, belonging to the $F\bar{4}3m$ cubic space group. The structure involves two combined face-centered cubic (FCC) lattices with a shift of 1/4 of a unit cell body along (111) direction. Figure 1.3 illustrates the CdZnTe zincblende structure where Cd (or Zn depending on composition) atoms are located at vertices and face centers, and Te atoms are located at tetrahedral corners (4 out of 8) [22]. In other words, CdZnTe structure can be defined as CdTe with a random distribution of Zn atoms replacing Cd atoms. Each atom is arranged in a tetrahedral structure sharing four outer electrons with those of the neighbours. One sublattice is occupied by cations (Cd^{2+} and Zn^{2+}) and the other by anions (Te^{2-}) [23].
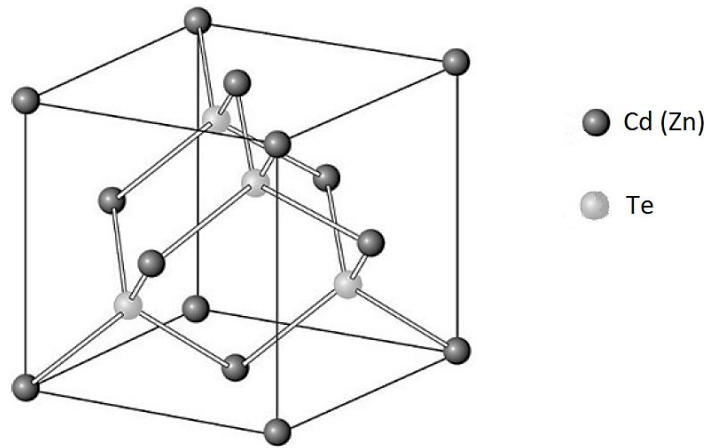
Figure 1.3. CdZnTe Zincblende structure, from [22].

The lattice constant for II-VI semiconductor materials obeys Vegars law and can be expressed as [24],

$$a(x) = a_1(1-x) + a_2x$$
<div align="right">Equation 1.1</div>

where the lattice constants a_1 is for CdTe, and a_2 for ZnTe, with the composition x value.

The lattice constant of $Cd_{1-x}Zn_xTe$ alloy changes from 0.648 nm to 0.610 nm as zinc composition x goes from 0 to 1 [22]. Therefore, the lattice constant for $Cd_{1-x}Zn_xTe$ can be rewritten as,

$$a = 0.64829 - 0.03803x \qquad \text{Equation 1.2}$$

The variation in the lattice constants for $Cd_{1-x}Zn_xTe$ causes small changes in unit cell dimensions due to the Zinc atoms substituting Cd atoms. The change in the lattice constant with respect to compositional parameter x for $Cd_{1-x}Zn_xTe$ is given in Figure 1.4a, while Figure 1.4b shows the near-neighbour distance for $Cd_{1-x}Zn_xTe$ changing from 2.81 Å, which is the bond length of Cd-Te to 2.64 Å (Zn-Te bond length) [21].
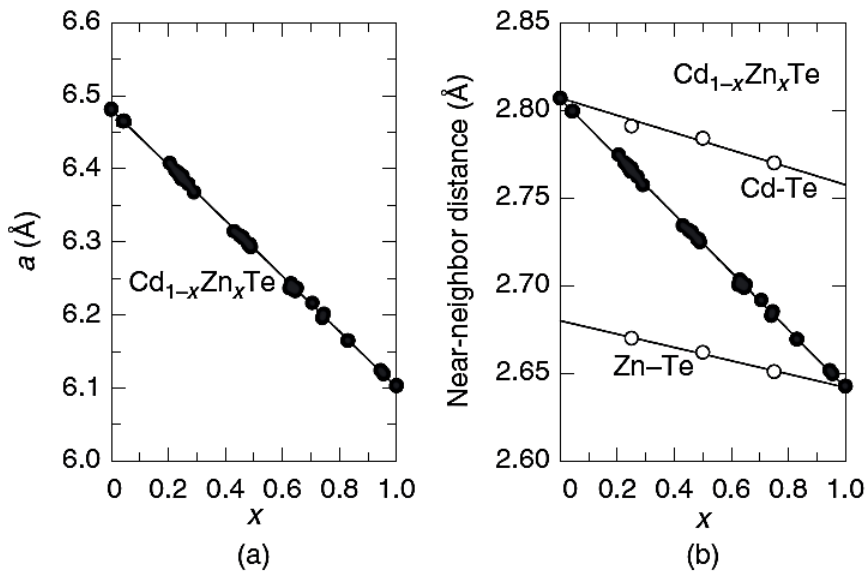
Figure 1.4. a) Change in $Cd_{1-x}Zn_xTe$ lattice constant a with composition x, b) Near-neighbour distance in $Cd_{1-x}Zn_xTe$ at room temperature, modified from [21].

1.1.2   Electronic Energy - Band Structure

The optical and electronic structures of CdZnTe material can be described using the electronic band structure and bandgap properties of CdZnTe. The bandgap is obtained from the energy difference between the valance and conduction bands and defined by its crystal lattice structure, including the near-neighbor distance and electronegativities of

6

Cd, Zn and Te atoms. The conduction band occurs at the first unoccupied level of the cation Cd^{2+} and Zn^{2+}, (5s level for Cd, 4s level for Zn), while the valence band contains the highest occupied level of the anion, Te^{2-} (5p level of Te) [3]. CdZnTe has a direct bandgap property which means that the valance and conduction band occurs at the same momentum position, Γ, within the first Brillouin zone, resulting in a direct emission of a photon by an electron [25]. The bandgap energy, E_g, for $Cd_{1-x}Zn_xTe$ material is described as

$$E_g(Cd_{1-x}Zn_xTe) = xE_g(ZnTe) + (1-x)E_g(CdTe) + cx(x-1) \qquad \text{Equation 1.3}$$

where c is the bowing parameter which is around 0.270 eV at 300 K. Additionally, CdTe and ZnTe materials both have direct-bandgap properties with bandgap energies of 1.475 eV and 2.394 eV, respectively. Accordingly, Equation 1.3 becomes

$$E_g(x) = 1.74x^2 - 1.01x + 1.51 \qquad \text{Equation 1.4}$$

According to Equation 1.2 and Equation 1.4, when Zn atoms substitute Cd in accordance with the composition, x, atomic distance decreases while the bandgap increases.

Since the band theory of solids is built on the periodicity of the material, which does not exist in an alloy like $Cd_{1-x}Zn_xTe$ due to the regional composition fluctuations, it is difficult to obtain its exact band structure. However, the band structure of $Cd_{1-x}Zn_xTe$ can be approximated using a linear interpolation between the structure of CdTe and ZnTe binary semiconductor compounds. Moreover, the band structure of CdTe is similar to the band structure of ZnTe semiconductors [24]. Figure 1.5 shows the electronic band structure of CdTe at 0 K with transitions between critical points calculated using the pseudo-potential method [26].
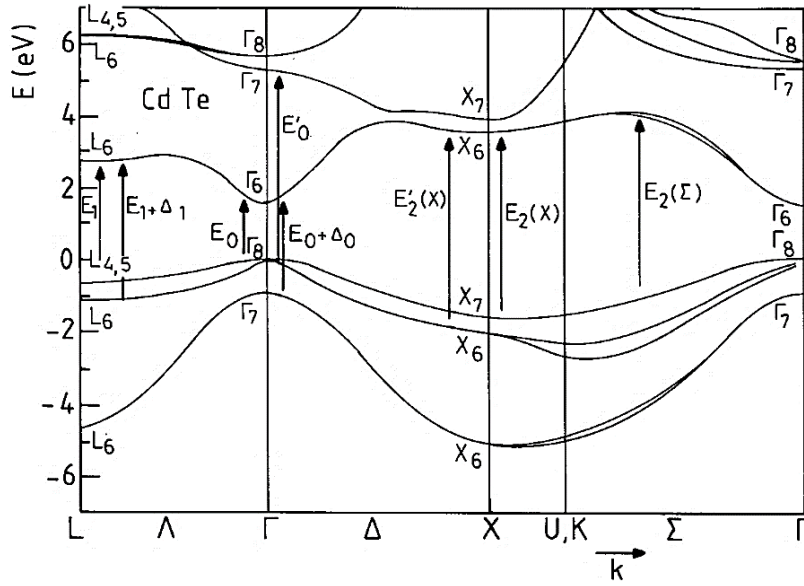
Figure 1.5. Band structure of CdTe at 0 K along with critical transitions located in the Brillouin zone, from [26].

Optical bandgap and transitions between critical points should be carefully analyzed since they define the shape of the optical emission spectrum and solar conversion efficiency. Additionally, the effect of structural variations on the electronic properties can be deduced using critical points [27]. Revealing critical points over a specific energy range provides the electronic band structure of the material and the quality of the crystal, including the lattice strain and defects [28]. According to Figure 1.5, CdTe has distinctive electronic band structure properties at the critical point energies. Among these critical points, transition at the E_0 edge is the optical direct bandgap energy of CdTe. In contrast, $E_0+\Delta_0$ and $E_1+\Delta_1$ gap energies are identified as the weak transitions from the spin-orbit splitting. E_1 is a strong transition at point L in the Brillouin zone [29]. The E_2 energy, which is not well-defined, is the transition at the saddle point [30]. The critical point energies for CdTe, ZnTe and CdZnTe alloys, adapted from [21], are given in Table 1.2.

8

Table 1.2 Energies (eV) for some critical points in CdTe, ZnTe and $Cd_{1-x}Zn_xTe$ alloy at 300 K, from [21].

Parameter	CdTe	ZnTe	$Cd_{1-x}Zn_xTe$
E_0	1.51	2.27	$1.55 + 0.49x + 0.27x^2$
$E_0+\Delta_0$	2.41	3.22	$2.41 + 0.57x + 0.24x^{2c}$
E_1	3.36	3.59	$3.36 - 0.01x + 0.24x^{2c}$
$E_1+\Delta_1$	3.95	4.17	$3.95 - 0.04x + 0.26x^{2c}$
E_2	5.3	5.3	$5.30 - 0.24x + 0.24x^{2c}$

*c is the bowing parameter [21].

1.1.3   Lattice Vibration Properties

Lattice vibrations which are principally initiated by the lattice thermal energy, are called phonons. Phonons have characteristic energies, momentum, frequencies, and wavenumbers like photons and electrons [31]. There exist two optical vibration modes in the phonon dispersion curves for $Cd_{1-x}Zn_xTe$, which are the longitudinal optical (LO) and transverse optical (TO) modes [32]. Optical phonon frequencies of CdTe, ZnTe, and $Cd_{1-x}Zn_xTe$ compounds acquired at low temperatures are presented in Table 1.3 [21]. Crystalline CdTe and its alloys exhibit additional vibration modes from secondary phases, including a Te A1 mode around 127 cm^{-1} caused by Tellurium precipitates [33].

Table 1.3 Optical phonon frequencies of CdTe, ZnTe and $Cd_{1-x}Zn_xTe$ compounds acquired at low temperatures (≤ 80 K), from [21].

Parameter	CdTe	ZnTe	$Cd_{1-x}Zn_xTe$
$\omega_{LO}(cm^{-1})$	175	209	$(175 + 52x - 18x^2)^{*a}$
	169	154	$(169 - 30x + 15x^2)^{*b}$
$\omega_{TO}(cm^{-1})$	175	181	$(175 + 6x)^{*a}$
	146	153	$(146 + 21x - 14x^2)^{*b}$

*[a]ZnTe-like.

*[b]CdTe-like.

1.1.4 Addition of Zinc

The addition of Zinc (Zn) improves the properties of CdTe, resulting in the ternary Cadmium Zinc Telluride ($Cd_{1-x}Zn_xTe$ or CdZnTe) compound semiconductor. The control of the Zn composition ratio, x, enables the adjustment of the optical and physical properties of $Cd_{1-x}Zn_xTe$ for a specific field application. Furthermore, the random substitution of Zn atoms into the CdTe results in a decrease in the lattice constant, an increase in the bandgap energy (from 1.475 eV to 2.394 eV as x goes from 0 to 1), and a reduction in the defect density [23], [25], [34]. Additionally, since Zn-Te has a higher binding and defect formation energy, a stronger bond, and lower ionicity than Cd-Te, the crystal lattice is strengthened by the addition of Zn, which increases the stability and the shear modulus of the material [23]. Furthermore, the reduction of the defect density by adding Zn atoms improves charge transport properties of the compound by eliminating trap sources such as Cd vacancies and Te interstitials in the material [25], [34].

1.1.5   CdZnTe-Based Solar Cells

Cadmium Zinc Telluride ($Cd_{1-x}Zn_xTe$) semiconductor compound has a promising potential as an absorber layer for highly efficient photovoltaic devices due to its tunable direct bandgap properties (from 1.45 to 2.26 eV) and high absorption coefficient ($>5\times10^5$/cm), which means that about 90% of incoming photons (with $hv > E_g$) can be absorbed in CdZnTe thickness of only a few microns [1].

CdZnTe based thin film solar cells were first studied in the late 1980s by several laboratories using the CdS/$Cd_{1-x}Zn_xTe$ device structure. The best cell efficiency was obtained to be around 4%, and devices suffered from low V_{oc} and FF [5]. There are rather few studies conducted to explain the low performance for CdS/$Cd_{1-x}Zn_xTe$ devices. In 2005, CdS/$Cd_{1-x}Zn_xTe$ devices were again the focus of interest by several U.S. universities and national laboratories. Efficiencies of CdS/$Cd_{1-x}Zn_xTe$ solar cells are limited to about 10% [35]–[37]. Since low performance was obtained using the CdS/$Cd_{1-x}Zn_xTe$ structure, a different approach was followed to utilize c-Si for the bottom cell and CdZnTe for the top cell. In this approach, CdZnTe was designed to have a bandgap around 1.70eV–1.80 eV, matching c-Si bandgap (1.1eV), providing a theoretical maximum efficiency of ~40% [38]. In 2010, Carmody [39] showed that $Cd_{1-x}Zn_xTe$/c-Si tandem solar cells fabricated by the MBE method have an efficiency of 17%. According to these results, $Cd_{1-x}Zn_xTe$/c-Si tandem solar cell appears to be an attractive material for its high performance and stability [38].

The structure of the CdZnTe solar cell consists of glass/ITO/CdS/CdZnTe/Au back contact, as demonstrated in Figure 1.6. The CdS/CdZnTe solar cell was manufactured in a superstrate structure where the light enters from the soda-lime glass side. The manufacturing process of a CdZnTe solar cell includes the following steps. First, indium tin oxide (ITO) was deposited on a glass substrate to be used as the front contact. Then, the n-type CdS layer ($E_g \approx 2.4\,eV$) was deposited on ITO as a window layer with 100–300 nm thicknesses. Afterward, the

p-type CdZnTe layer was coated on glass/ITO/CdS. As a result, a heterojunction was created between n-type CdS and p-type CdZnTe layers. Generally, since higher carrier concentration was produced in the CdS layer compared to the CdZnTe layer, a depletion region was mainly formed within CdZnTe. Finally, an ohmic metal back contact layer with a high work function (generally Au) was used to complete the device structure.
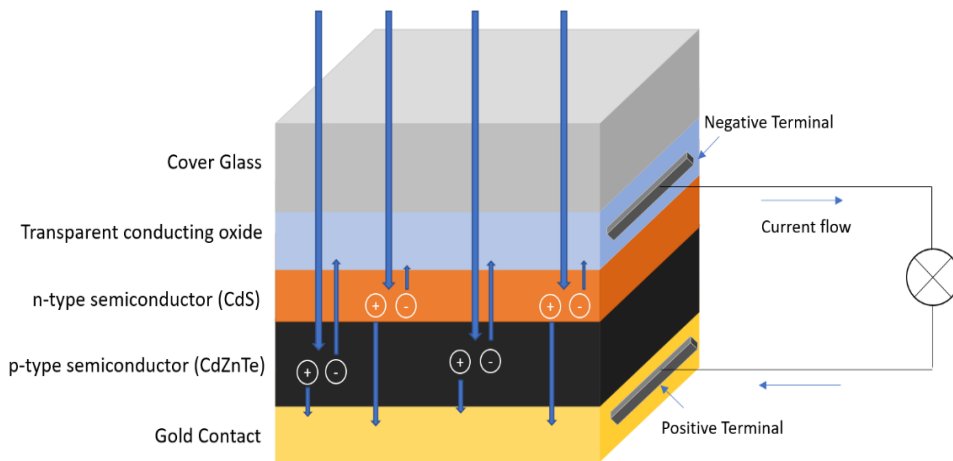
Figure 1.6. CdZnTe solar cell structure in a superstrate configuration.

1.2   Thesis Outline

The aim of this dissertation was to fabricate and characterize thin CdZnTe films (<2 μm) for solar cell applications by thermal evaporation at low substrate temperatures using CdZnTe single crystal pieces as source material. The first goal was to manufacture and thoroughly analyze CdZnTe thin films with high crystalline quality, uniform component distribution, and free of secondary phases, significantly affecting the device's performance. The second goal was to fabricate and characterize CdS/CdZnTe thin film-based photovoltaic devices in the superstrate structure. Finally, the current conduction properties of the CdZnTe/Si, in addition to the behavior of the interfacial layer, were studied in detail for possible device applications. A brief introduction to CdZnTe semiconductor material was already presented in Chapter 1. The rest is structured as follows.

- Chapter 2

Chapter 2 presents the theoretical background and basic descriptions of the physics behind the operation of semiconductor thin film solar cell structure.

- Chapter 3

Chapter 3 focuses on the description of experimental setups used in this study. The chapter is broken into three subsections. The first subsection starts by explaining the deposition system and proceeds with describing the post-deposition processes applied for CdZnTe thin films. The second section discusses the characterization methods utilized to analyze morphological, structural, and optical properties of CdZnTe thin films. Finally, device characterization techniques are discussed to investigate the electrical properties of CdZnTe heterojunction devices.

- Chapter 4

Chapter 4 presents the deposition optimization studies, the effect of post-deposition treatment, and the process for the production of high-quality CdZnTe thin films. The effect of the deposition parameters, including various film thicknesses and substrate temperatures, and post-deposition parameters such as annealing and $CdCl_2$ treatment have also been presented.

- Chapter 5

Chapter 5 discusses the surface characterization techniques, including X-Ray photoelectron spectroscopy (XPS), to analyze the dynamics of native oxide formation, the depth profile of atomic compositions, addition to variable angle spectroscopic ellipsometry (VASE) to examine the optical dielectric response of the CdZnTe thin films.

- Chapter 6

Chapter 6 presents the effects of various CdS and CdZnTe thin film thicknesses and annealing on the electrical properties of glass/ITO/CdS/CdZnTe/Au thin film heterojunction devices utilizing thin (<2 μm) CdZnTe absorber layer.

- Chapter 7

Chapter 7 discusses the current conduction mechanism of the CdZnTe/Si structure using temperature-dependent current-voltage $(I - V)$ measurement, while the nature of the interfacial layer was examined utilizing frequency-dependent capacitance-voltage $(C - V)$ measurement.

- Chapter 8

Chapter 8 summarizes the major findings of this study and introduces suggestions for future works.

CHAPTER 2

THEORETICAL CONSIDERATIONS

This chapter provides fundamental theoretical information about the optical properties of semiconductors, the physics of p-n junction, diode characteristics of heterojunctions, and operation mechanisms of metal-semiconductor junctions. The chapter also includes brief information on solar cell mechanisms and their performance parameters.

2.1   Optical Properties of Semiconductors

When light interacts with a semiconductor material, the characteristic of light is modified by the optical properties of that material. The most commonly known optical properties are reflection, transmission, absorption, and refraction. These properties can be correlated with optical coefficients of semiconductors, such as refractive index, extinction coefficient, and absorption coefficient, along with their dispersion relations [1]. The refractive index and absorption coefficient has the utmost importance in the design and characterization of optical and optoelectronic semiconductor devices. Moreover, the optical constants present substantial information about the semiconductor's electronic energy-band structure [40].

2.1.1   Optical Constants

The refractive index, n, and extinction coefficient, k, are two critical optical constants used to analyze the macroscopical and microscopical features of semiconductor material, including the complex nature of the surface and electronic energy-band properties of the material. The refractive index n is described as

$$n = \frac{c}{\vartheta} \qquad\qquad \text{Equation 2.1}$$

where c and ϑ are the velocities of light in a vacuum and inside the material, respectively. By combing Equation. 2.1 with Maxwell's equations, the refractive index can be rewritten as

$$n = \sqrt{\varepsilon\mu} \qquad\qquad \text{Equation 2.2}$$

where ε is the relative permittivity, μ is the relative magnetic permeability. For nonmagnetic materials, μ is equal to unity ($\mu = 1$), so the refractive index simply becomes

$$n = \sqrt{\varepsilon} \qquad\qquad \text{Equation 2.3}$$

Equation 2.3 reveals the relation between the dielectric and optical features. The dielectric constant, ε, is a frequency (ν) dependent property, so the refractive index also changes with frequency. The correlation between the refractive index and the frequency is called dispersion. On the other hand, the complex dielectric function $\varepsilon(E) = \varepsilon_1(E) + i\varepsilon_2(E)$ is utilized to describe the optical features of material at all photon energies of $E = h\nu$. Therefore, n is also a complex function of frequency when the incident light is attenuated after it passes through the material due to the interactions between photons and electrons [41]. Light loses its energy during these interactions, and the loss mechanisms include phonon and photon generation, absorption, and scattering [1]. Hence, the complex refractive index is stated as

$$\widetilde{N}(E) = n(E) + ik(E) = \sqrt{\varepsilon(E)} = \sqrt{\varepsilon_1(E) + i\varepsilon_2(E)} \qquad \text{Equation 2.4}$$

The optical constants $n(E)$ and $k(E)$ are real and positive numbers and can be obtained by optical measurements. Solving Equation 2.4, one can obtain

$$\varepsilon_1(E) = n(E)^2 - k(E)^2 \qquad\qquad \text{Equation 2.5a}$$

$$\varepsilon_2(E) = 2n(E)k(E) \qquad\qquad \text{Equation 2.5b}$$

and

16

$$n(E) = \sqrt{\frac{(\varepsilon_1(E)^2 + \varepsilon_2(E)^2)^{1/2} + \varepsilon_1(E)}{2}}$$ Equation 2.6

$$k(E) = \sqrt{\frac{(\varepsilon_1(E)^2 + \varepsilon_2(E)^2)^{1/2} - \varepsilon_1(E)}{2}}$$ Equation 2.7

Other critical optical features, including absorption coefficient $\alpha(E)$ and normal-incidence reflectivity $R(E)$ is also derived using this dispersion relation between the dielectric function and optical coefficients [40]. As a result, $\alpha(E)$ and $R(E)$ can be calculated as

$$\alpha(E) = \frac{4\pi}{\lambda} k(E)$$ Equation 2.8

$$R(E) = \frac{[n(E) - 1]^2 + k(E)^2}{[n(E) + 1]^2 + k(E)^2}$$ Equation 2.9

As stated in the equation above, the absorption coefficient $\alpha(E)$ varies with wavelength, λ, and extinction coefficient, $k(E)$ of the material [42]. Additionally, α is also experimentally obtained using the transmittance (T) and reflectance (R) spectrum, and thickness, t, of a material:

$$T = \frac{(1 - R)^2 \, exp(-\alpha t)}{1 - R^2 \, exp(-2\alpha t)}$$ Equation 2.10

For large αt values, the above equation can be rewritten as

$$\alpha = \frac{1}{t} ln\left(\frac{(1 - R)^2}{T}\right)$$ Equation 2.11

2.1.2   Optical Absorptions

Several possible absorption processes may occur in a crystalline semiconductor, such as free carrier absorption, impurity absorption, lattice absorption, exciton absorption, and fundamental absorption [1]. The energy of the incident photons determines which type of absorption process will occur. Fundamental absorption is possibly the

17

most crucial absorption type, which involves a process of photon absorption with the energy of $hv \geq E_g$. In this process, electrons are photoexcited directly from valence band (VB) to conduction band (CB) [43]. The fundamental absorption appears in two basic transition processes in semiconductors which are direct and indirect band-to-band transitions. The conservation of energy and momentum is a must during the absorption process for both transitions. Figure 2.1 illustrates the basic illustration of a photon absorption process in a direct and indirect band gap.
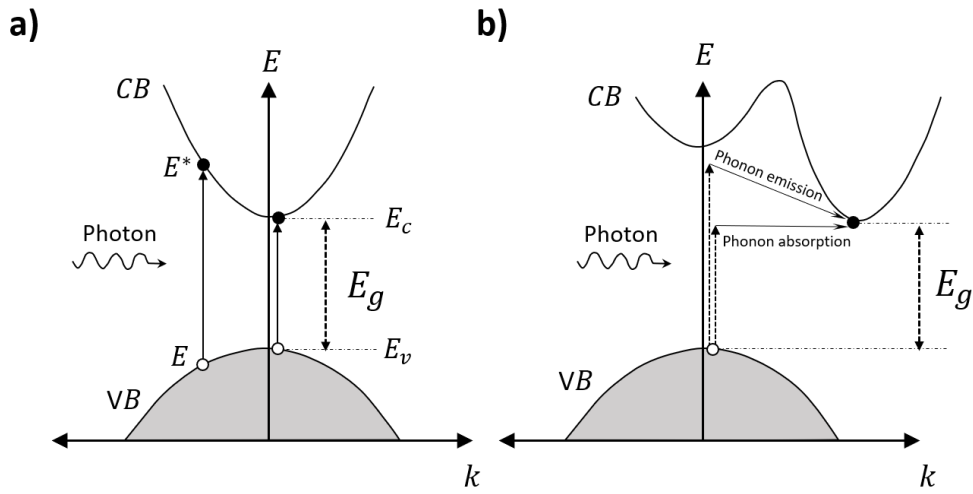
Figure 2.1. The schematic diagram for (a) a direct transition of excited electrons by absorption of a photon with an energy of $hv \geq E_g$, from VB to CB and (b) an indirect transition of an electron by photon absorption. The energy and momentum are conserved by either the absorption or emission of a phonon.

As shown in Figure 2.1 (a), since there is no phonon involved in the absorption process for a direct bandgap transition and the photon momentum is negligibly smaller than the electron momentum, the electron's wavevector k does not shift during a vertical transition. Using quantum mechanics probability for a direct transition, absorption coefficient α is derived as

$$\alpha hv = A(hv - E_g)^{1/2} \qquad \text{Equation 2.12}$$

where the constant is $A \approx (e^2/nch^2m_e^*)[2m_e^*m_h^*/(m_e^* + m_h^*)]^{3/2}$ in which m_e^* is reduced electron and m_h^* is hole effective masses. The energy band gap can be determined from this equation by extrapolation to zero photon energy.

18

Figure 2.1 (b) shows the transition in an indirect semiconductor, which is shifted so that the momentum is not conserved. When the electron is photoexcited from the VB to the CB, some of the momentum is transferred to the lattice heating and energy losses. So, the indirect transition has a relatively smaller absorption coefficient than the direct transition. As a result, radiation penetrates deeper into the indirect bandgap semiconductors, making absorption or emission activities less efficient than direct semiconductors [43].

2.2   Physics of p-n Junction

Since most semiconductor devices have a minimum of one junction between p- and n-type semiconductors, p-n junctions impose significant importance not only for optoelectronic applications but also for understanding semiconductor device characteristics and operations. Therefore, comprehending the physics behind the p-n junction is crucial in studying semiconductor technology.

2.2.1   Depletion Layer and Built-in Potential

Semiconductors can be classified with respect to their majority carrier concentration. If the majority carriers are electrons, the material becomes n-type while the majority carriers are holes, then it becomes p-type. A semiconductor can be modified to be n- or p-type with controlled doping of donor or acceptor impurities, respectively. When a p-type semiconductor is brought together with an n-type semiconductor, the formation of a p-n junction is ensured. Junction formation initiates hole diffusion from the p region into the n region, leaving a negatively charged region on the p-side near the junction. Additionally, electrons diffuse from the n region into the p region, leaving a positively charged region on the n-side near the junction. Since the region near the junction is depleted of the majority carriers (both holes and electrons), it is called the depletion region or space charge region (SCR). The outer regions for both sides, excluding the depletion region, are essentially neutral and is referred to as

quasi-neutral region (QNR). As shown in Figure 2.2. (a), positive and negative charges (donors and acceptors) are separated in the depletion region, creating an electric field directed from positive to negative charges or from the n- to p- region, which results in an electrostatic potential difference in the junction named the built-in potential, V_{bi}. Figure 2.2 (b) reveals the energy-band diagram and the resulting built-in potential for the p-n junction in an equilibrium state.
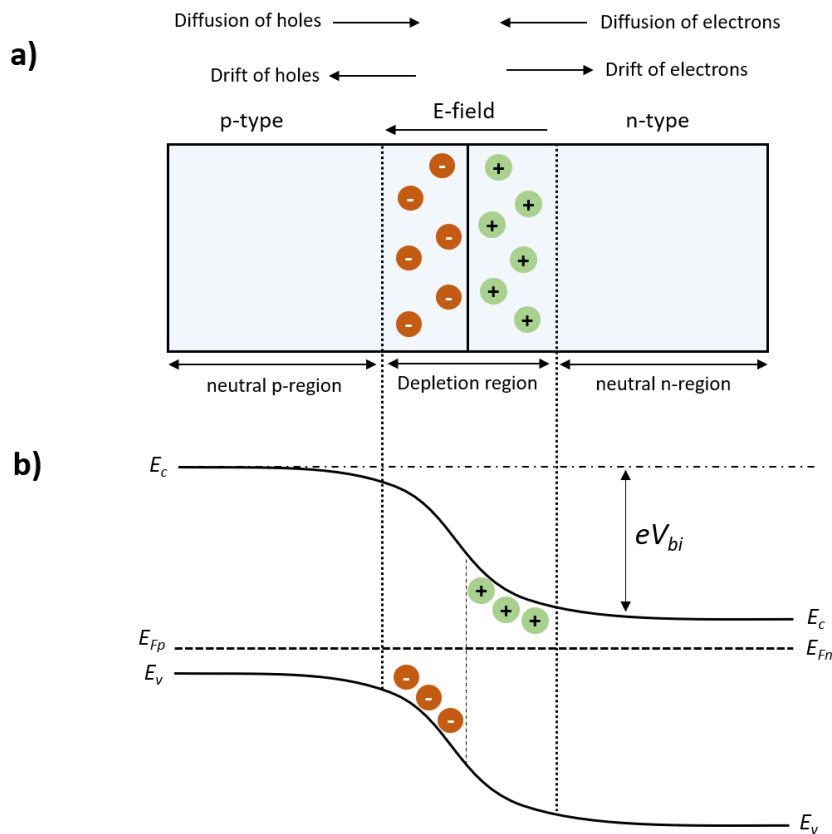
Figure 2.2. Illustration of (a) a p-n junction showing space charges (donors and acceptors) in the depletion region, the resulting electric field and current directions, and (b) the energy-band alignment profile of a p-n junction in equilibrium and resulting built-in potential, adopted from [44].

Owing to the potential difference that exists in the depletion region, equilibrium is sustained. There will be no further current flow of majority carriers, so the diffusion

current of electrons will be canceled with the drift current of electrons. The same phenomenon applies to the current of holes.

$$J_n(diffusion) + J_n(drift) = 0 \qquad \text{Equation 2.13}$$

$$J_p(diffusion) + J_p(drift) = 0 \qquad \text{Equation 2.14}$$

Using Equation 2.13 and Equation 2.14, a quantitative relation between built-in potential, V_{bi} and doping (donor N_d and acceptor N_a) concentrations under equilibrium conditions can be obtained. Let's consider the diffusion and drift currents for holes at equilibrium:

$$J_p = q \left[\underbrace{\mu_p p(x) E(x)}_{\text{drift}} - \underbrace{D_p \frac{dp(x)}{dx}}_{\text{diffusion}} \right] = 0 \qquad \text{Equation 2.15}$$

Then, using $E(x) = -dV(x)/dx$, the equation now becomes

$$\frac{\mu_p}{D_p} E(x) = -\frac{\mu_p}{D_p} \frac{dV(x)}{dx} = \frac{1}{p(x)} \frac{dp(x)}{dx} \qquad \text{Equation 2.16}$$

Finally, using the Einstein relation for μ_p and D_p $\left(\mu_p / D_p = q/kT \right)$ and by integrating over appropriate limits, the built-in potential V_{bi} can be obtained as

$$V_{bi} = \frac{kT}{q} ln \frac{N_a N_d}{n_i^2} \qquad \text{Equation 2.17}$$

where n_i is the intrinsic carrier concentration. Another important parameter, the depletion layer width, W, is also calculated by Poisson's equations using the depletion region approximation under equilibrium conditions:

$$W = \left[\frac{2\varepsilon_s V_{bi}}{q} \frac{(N_a + N_d)}{N_a N_d} \right]^{1/2} \qquad \text{Equation 2.18}$$

If an abrupt junction with p$^+$-n or n$^+$-p formation is of concern, the variation in the built-in potential and depletion region will be mainly inside the lightly doped region. So, under equilibrium conditions, Equation 2.18 reduces to

$$W = \left[\frac{2\varepsilon_s V_{bi}}{qN}\right]^{1/2}$$

<div align="right">Equation 2.19</div>

where N can be N_d or N_a relying on $N_a \geq N_d$ or vice versa.

2.2.2   Junction Capacitance

The capacitance associated with a p-n junction arises from two regions of charge, which are the junction capacitance and the diffusion (storage) capacitance. The junction capacitance is called depletion layer capacitance, resulting from splitting (+) and (-) charges in the depletion region. In contrast, diffusion capacitance arises from the excess charges outside the depletion region due to the infusion of minority carriers. Junction capacitance is predominant in the reverse bias conditions, whereas diffusion capacitance is predominant under forward bias conditions [44].

Since there is a splitting of (+) and (-) charges in the depletion region, capacitance arises within the depletion region. Increasing reverse bias voltage results in a widening of the depletion region, which yields extra (+) charges in n region and extra (-) charges in the p region. Junction capacitance is identified as

$$C_j = \frac{dQ_j}{dV} = \frac{\varepsilon_s}{W}$$

<div align="right">Equation 2.20</div>

For one-sided abrupt junction approximation for reverse bias conditions, junction capacitance is given as

$$C_j = \frac{\varepsilon_s}{W} = \sqrt{\frac{q\varepsilon_s N}{2}}\left[V_{bi} - V - \frac{kT}{q}\right]^{-1/2}$$

<div align="right">Equation 2.21</div>

Junction capacitance for a one-sided abrupt junction is related to the doping (donor N_d and acceptor N_a) concentration in the low doped region. Rearranging this equation, one can get

$$\frac{1}{C_j^2} = \frac{2}{q\varepsilon_s N}\left(V_{bi} - V - \frac{kT}{q}\right)$$

<div align="right">Equation 2.22</div>

$$\frac{d\left(1/C_j^2\right)}{dV} = -\frac{2}{q\varepsilon_s N} \qquad \text{Equation 2.23}$$

Considering the equations and Figure 2.3, if one plot $1/C^2$ vs. V graph, a straight line will be obtained for an abrupt junction. The slope is inversely proportional to the doping concentration (or impurity concentration), N, and extrapolating to $1/C^2 = 0$ gives the built-in potential, $V_{bi} - kT/q$ [45].
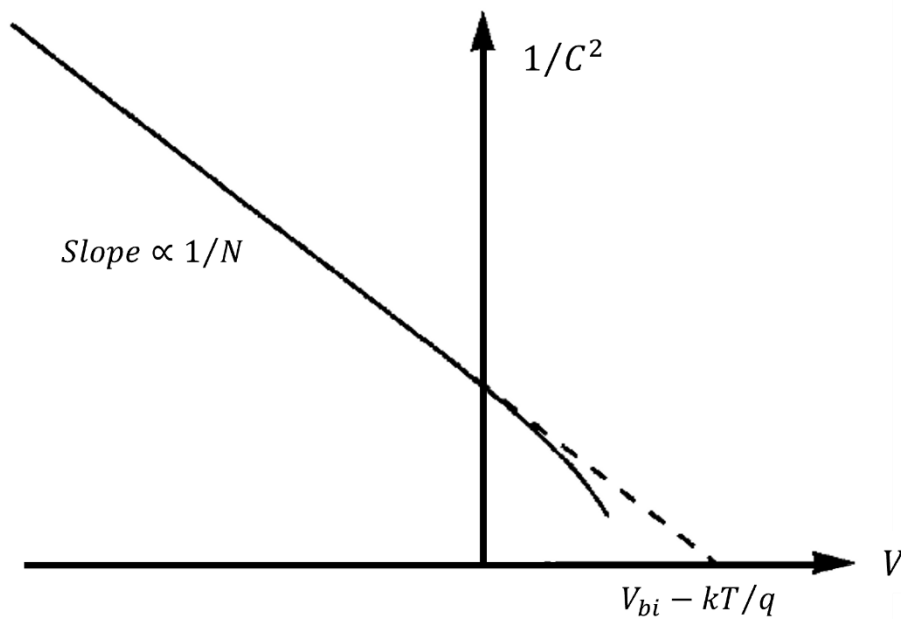
Figure 2.3. The plot of $1/C^2$-V gives both built-in potential and doping concentration N, from [31].

On the other hand, under forward-biased conditions, the total p-n junction capacitance is the sum of both depletion and diffusion capacitance. Diffusion capacitance also contributes significantly to the total capacitance due to the charge injections by minority charges. The main properties of the diffusion capacitance are the fact that it depends both on the frequency and the forward DC current. It decreases as frequency increases, and it is related to the DC current $\left[\propto e^{qV/k_B T}\right]$ [31].

2.3   Heterojunctions

Semiconductor heterojunctions utilize the junction formation between two different semiconductor materials with different energy bandgaps for various device applications, including solar cells, as shown in Figure 2.4 [31]. The goal for an efficient heterojunction formation is to have a well-matched lattice property. Mismatch of the lattice introduces dislocations at the junction interface, resulting in interface states (interface traps) [46]. The work function of a semiconductor, ϕ_s, is described as the energy needed to excite an electron from the Fermi level (E$_F$) to the vacuum level (E$_{vac}$), while semiconductor electron affinity, χ_s, is the energy necessary to excite an electron from CB to E$_{vac}$. The difference between electron affinities of semiconductors causes spikes and notches at the interface junction.
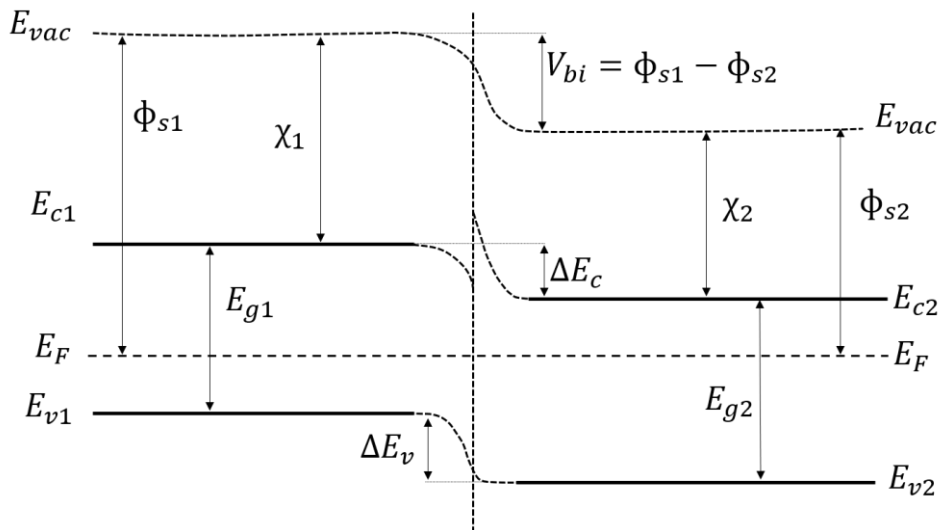
Figure 2.4. Equilibrium energy band diagrams after the formation of an abrupt p-n heterojunction.

As demonstrated in Figure 2.5, the heterojunction can be composed of two active layers, which can either be an absorber layer joint with a window layer (p-CdZnTe/n-CdS) or two absorber layers (p-CdZnTe/p$^+$-Si) depending on the application that the heterojunction device is used [46]. The window material has a wider bandgap property which is used to create the heterojunction and to assist the

carrier transport. The junction between the window layer and absorber is an abrupt junction. Additionally, the heterojunction components have not only different energy band gaps and work functions but also have unique electron affinities and various carrier concentrations, which results in a discontinuity at the CB of the junction interface in the energy band diagram.
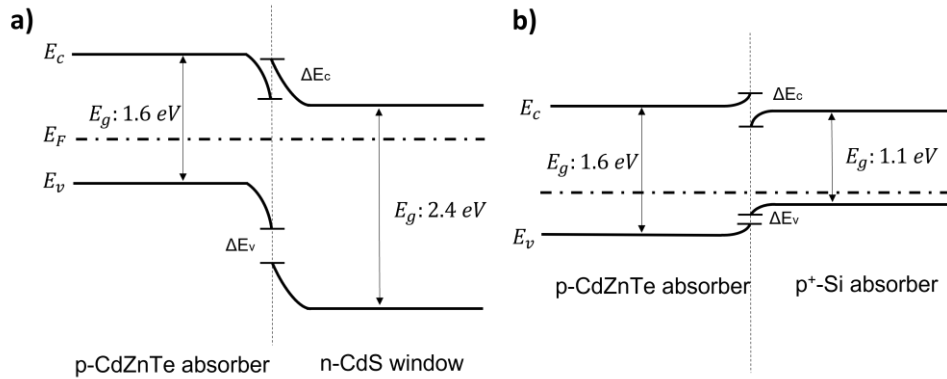
Figure 2.5. Band diagram configurations for (a) p-CdZnTe/n-CdS absorber-window structure and (b) p-CdZnTe/p$^+$-Si absorber-absorber structure (excluding the metal contacts).

2.4   Metal-Semiconductor Junctions

Metal-semiconductor junctions exist in every semiconductor device; therefore, it is important to understand their formation and operation mechanisms. It can behave either as a nonrectifying (ohmic contact) or rectifying (Schottky contact or Schottky barrier).

2.4.1   Ohmic Contact

A Nonrectifying junction or ohmic contact is formed between a metal and a semiconductor in which current can flow freely across the junction in both directions. In other words, there is no barrier formation when carriers flow through the junction in either direction under the applied electric field. The only parameter limiting the

flow of the current is the resistance of the semiconductor outside the contact region. Additionally, ohmic contact has nonrectifying, linear current-voltage characteristics. For solar cell devices, at least one of the contacts should be ohmic, which is necessary to obtain the external connections. Therefore, the formation of a suitable ohmic contact with a good adhesion property is necessary so that the contact will not degrade the performance of the device. The energy band diagrams for ohmic contact formation of n- and p-type semiconductors are given in Figure 2.6. The energy band diagram of a metal and semiconductor material is aligned at the Fermi energy level at equilibrium.
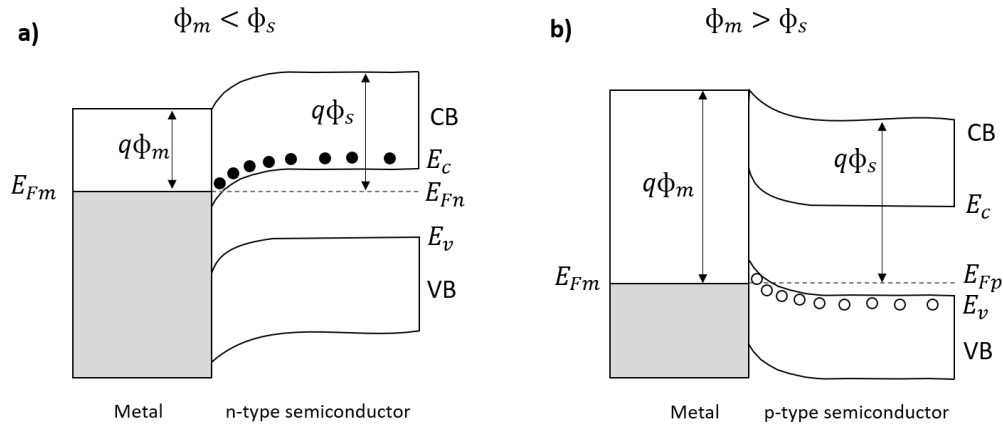
Figure 2.6. Energy band diagram for an ohmic contact formation between (a) metal and n-type semiconductor and (b) metal and p-type semiconductors.

Metal is described only by its chemical potential, which is also known as the work function ϕ_m. As shown in Figure 2.6 (a), to form a good ohmic contact with n-type semiconductors, ϕ_m of the metal must be smaller than n-type semiconductor resulting in an accumulation of electrons. On the other hand, ohmic contact with p-type semiconductors can be obtained using metals with larger work functions (Figure 2.6 (b)). The accumulation region is formed near the junction with excess majority carriers (electrons in CB for n-type or holes in VB for p-type). The equilibrium is reached when Fermi levels of both sides are lined up by tunneling of accumulated carriers from metal into the semiconductor.

For p-type semiconductors with high work functions, it is challenging to obtain suitable ohmic contacts because of the complexity of finding a metal with high ϕ_m. In this condition, the general technique to obtain suitable ohmic contact requires forming a more heavily doped surface layer.

2.4.2 Schottky Contact

Schottky contact or Schottky barrier junction that is formed with a metal and a semiconductor only allow current to flow in one direction by establishing a potential barrier at the junction and exhibiting a rectifying behavior. The current transport mechanism in a Schottky contact is dominated by thermionic emission of majority carriers, unlike p-n junction, which is due to minority carriers [47]. In a Schottky contact, barrier height, $q\Phi_B$, is identified by the difference between the metal Fermi energy and the band edge of the semiconductor where the majority carriers (electron or holes) reside [48]. For n-type semiconductors, $q\Phi_B$, can be obtained by

$$q\Phi_B = q\phi_m - q\chi_s \qquad \text{Equation 2.24}$$

For p-type semiconductors, $q\Phi_B$, can be defined as:

$$q\Phi_B = E_g - (q\phi_m - q\chi_s) \qquad \text{Equation 2.25}$$

Additionally, built-in potential, V_{bi}, obtained from the energy difference between the metal work function, ϕ_m, and the work function of the semiconductors, ϕ_s:

$$qV_{bi} = q\phi_m - q\phi_s \qquad \text{Equation 2.26}$$

Rectifying properties for a metal-semiconductor junction not only depend on ϕ_m but also on the conductivity type of the semiconductor. Therefore, to form a Schottky contact with a particular semiconductor material, ϕ_m should be selected properly. Hence, Schottky contact can be formed with an n-type semiconductor if ϕ_m is larger, while for a p-type semiconductor, ϕ_m should be less than ϕ_s.
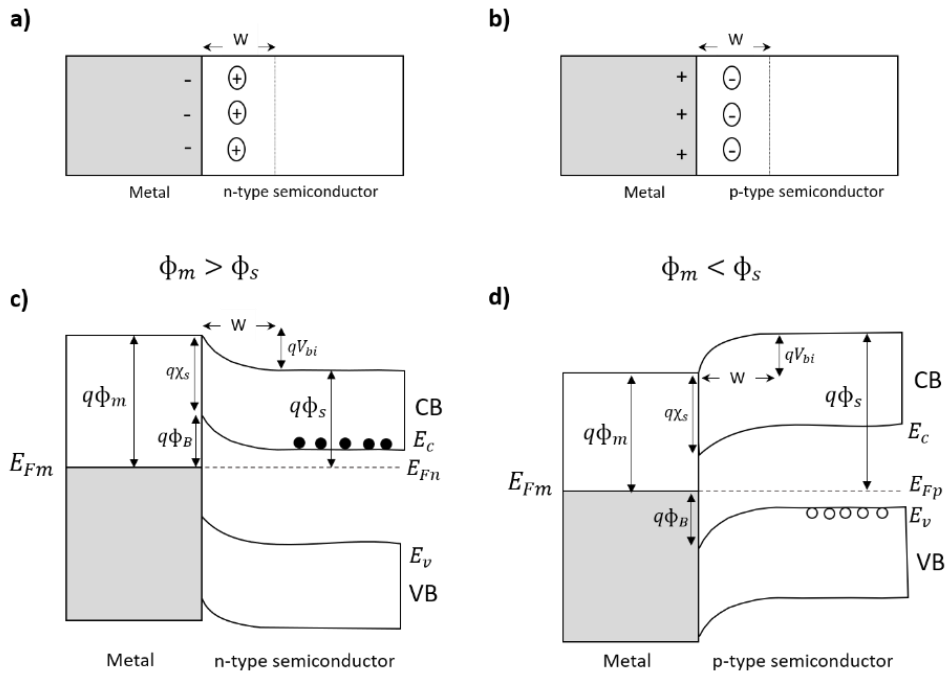
Figure 2.7. Energy band diagram for a Schottky contact formation between (a)-(c) metal and n-type semiconductor and (b)-(d) metal and p-type semiconductor.

Figure 2.7 illustrates energy band diagrams for a Schottky junction formation between metal and n-type and p-type semiconductors. The potential barrier between the metal and the semiconductor, $q\Phi_B$, is also identified on the energy band diagram. As shown in Figure 2.7, when a Schottky junction is formed, the free carriers (electrons or holes) flow until the fermi levels line up at equilibrium. The flow of free carriers from semiconductors leaves behind a depleted region in the semiconductor. The depletion region has been depleted of free carriers, and an electric field is formed from positive charges to negative charges on the interface of the metal semiconductor. Therefore, a contact potential, namely built-in potential, is obtained. Eventually, the built-in potential blocks further flow of charges, and equilibrium is achieved. The built-in field in the depletion region of the Schottky junction allows Schottky diodes to be widely used in photovoltaic devices and also as photodetectors. Schottky diodes exhibit rectifying current-voltage characteristics, and the diode equation is given as

28

$$I = I_0\left(e^{qV/nk_BT} - 1\right) \qquad\qquad \text{Equation 2.27}$$

where I_0 is the reverse saturation current, n is the diode ideality factor, k_B is the Boltzmann constant, and T is the absolute temperature. The current transport mechanism in an ideal diode is purely thermionic with a near-unity value for the ideality factor. However, a real diode does not have a uniform junction formation over its entire area, resulting in patchiness of its barrier height which leads to $n > 1$. The ideality factor can be obtained using

$$n = \frac{q}{k_BT}\frac{dV}{d(lnI)} \qquad\qquad \text{Equation 2.28}$$

Accordingly, the diode ideality factor is obtained from the slope of the straight-line under forward bias in the current-voltage plot. Additionally, using Equation 2.27, the reverse saturation current I_0 is acquired by extrapolating the semi-log $I - V$ curve at $V = 0$. Finally, using reverse saturation current I_0 value, the zero-bias barrier height Φ_{B0} can be calculated from

$$\Phi_{B0} = \frac{k_BT}{q}\,ln\left(\frac{AA^*T^2}{I_0}\right) \qquad\qquad \text{Equation 2.29}$$

where A^* is the Richardson constant and A is the device area.

2.5   Solar Cells

Solar cells are carefully designed semiconductor diodes that efficiently absorb and transform light into electrical energy [43]. The process of a p-n junction solar cell is demonstrated in Figure 2.8. After junction illumination, the absorption of photons activates the transition of electrons from VB to CB, so electron-hole pairs are created. After the separation of carriers by the electric field before they recombine, electrons flow into the n region, while holes are separated into the p region. Finally, the separated carriers, which are collected by the electrodes, generate a current that powers an external load.
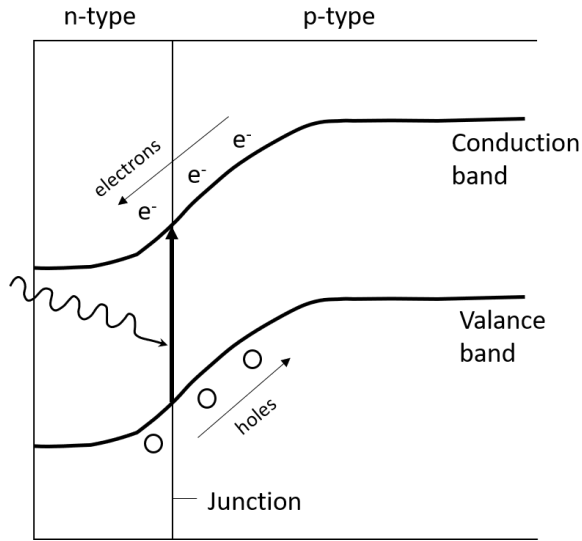
Figure 2.8. The operation of p-n junction solar cell. Junction illumination creates electron-hole pairs. The separation of carriers generates a current flow that powers the external circuit.

The current for an ideal solar cell which is described by the Shockley equation as a shift in the current from the photo-generated current I_{ph}, is given as

$$I = I_{ph} - I_0\left[e^{(qV/k_BT)} - 1\right]$$
<div align="right">Equation 2.30</div>

where I_0 is the diode saturation current. Real solar cells can deviate from ideal case solar cells due to power dissipations from the contact resistance and current losses. Figure 2.9 (a) gives the equivalent circuit of a real case solar cell. Current for real case solar cells is described as

$$I = I_{ph} - I_0\left[e^{(q(V+IR_s)/nk_BT)} - 1\right] - \left[(V + +IR_s)/R_{sh}\right]$$
<div align="right">Equation 2.31</div>

where R_s is the series resistance arising from the contacts and semiconductor while R_{sh} is the parallel or shunt resistance resulting from the leakage current through the solar cell. The quantities R_s and R_{sh} values can be obtained from the slopes of the current-voltage curve given in Figure 2.9 (b), at $V = 0$ and at $I = 0$, respectively.
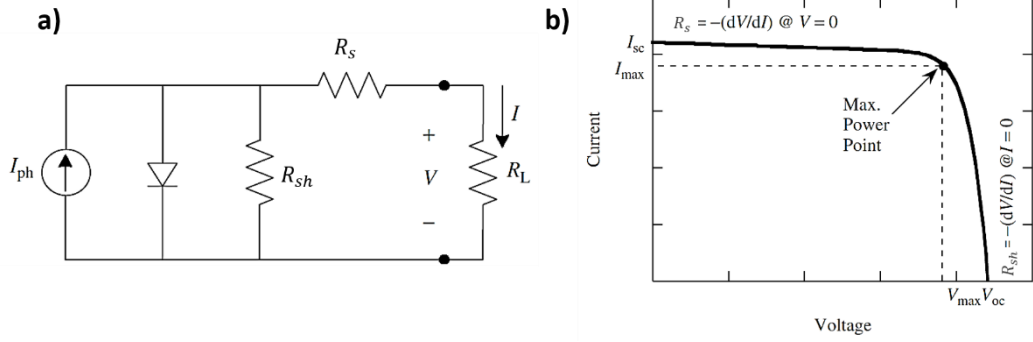
Figure 2.9. (a) Solar cell equivalent circuit. R_s and R_{sh} are parasitic resistances in series and parallel connection, respectively. (b) Current-voltage characteristic of a solar cell. The maximum power output for the cell is also indicated, adopted from [49].

The performance of a solar cell can be described using three parameters which are the short-circuit current, I_{sc}, the open-circuit voltage, V_{oc}, and the fill factor, FF [1]. In an ideal solar cell, I_{sc} is equal to the photo-generated current, I_{ph}. However, for real case solar cells, given in Figure 2.9 (b), I_{sc} can be obtained when voltage across the cell is zero. The relationship between V_{oc} and I_{ph} is given as

$$V_{oc} = \frac{nk_BT}{q} \ln\left(\frac{I_{ph}}{I_0} + 1\right) \qquad \text{Equation 2.32}$$

Moreover, the open-circuit voltage, V_{oc}, can also be obtained from the current-voltage plot where the illuminated current is zero.

The fill factor, FF, which is used to measure the quality of a solar cell, describes the rectangular property in the $I - V$ plot where the maximum power output per unit area ($P_{max} = V_{max}I_{max}$) is available from a cell, as demonstrated in Figure 2.9 (b). The fill factor of a solar cell can be obtained by using Equation 2.33 and should be less than unity, $FF \leq 1$.

$$FF = \frac{P_{max}}{V_{oc}I_{sc}} = \frac{V_{max}I_{max}}{V_{oc}I_{sc}} \qquad \text{Equation 2.33}$$

31

Finally, the conversion efficiency of a solar cell is defined as

$$\eta = \frac{V_{oc}I_{sc}FF}{P_{in}}$$
Equation 2.34

where P_{in} is the incident illumination power.

CHAPTER 3

METHODOLOGY

The deposition technique and post-deposition processes performed to develop high-quality CdZnTe thin films were explained in detail. The growth mechanism and material properties of CdZnTe thin films and heterojunction devices were analyzed using a variety of investigative techniques. Therefore, a thorough explanation of experimental setups with their working principles and operations was introduced.

3.1 Deposition Process for CdZnTe Thin Films

Various techniques can be used for deposition of CdZnTe thin films, such as magnetron sputtering [50], molecular-beam epitaxy [51], closed-space sublimation [52], and thermal vacuum evaporation [53], [54]. However, to reduce the power consumption and satisfy the desired film quality on variable substrates, low-temperature methods must be used [55]. Among low-temperature techniques for manufacturing CdZnTe thin films, the most suitable one is the thermal vacuum evaporation technique due to its controllable deposition rate, high efficiency, good reproducibility, low material expenditure, and low-cost operation [56]. It also allows various possibilities to adjust preparation requirements, which assist in studying the relation of physical features of deposited films and deposition parameters. The advantages of using the thermal vacuum evaporation technique can be listed as; avoiding impurities during film growth, reducing the formation of oxides, and providing slow rate deposition to form high-quality films. Therefore, in this study, a low-temperature thermal evaporation technique has been used to fabricate CdZnTe thin films for large-scale solar cell applications.

Thermal vacuum evaporation is essentially the transition of material from a solid phase to a vapor phase by heating the source to sufficiently high temperatures under

high vacuum conditions. The thermal evaporation system used for CdZnTe thin film deposition is schematically illustrated in Figure 3.1. The deposition rate and uniformity were controlled by adjusting the source temperature and arranging the distance between source and substrate. According to the deposition area and the required film thickness homogeneity, the substrate holder was located 12 cm above the source material. Film homogeneity was controlled using single crystal CdZnTe pieces as source material with a highly uniform component distribution. The CdZnTe single crystal pieces were obtained from the ingots produced by the VGF method in METU-CGL with a purity of 99.999%. Additionally, to eliminate the formation and incorporation of oxides during the deposition process, high vacuum conditions with a chamber pressure of 1×10^{-6} mbar were satisfied. The evaporation rate and film thickness were checked by an InficonXTM/2 quartz crystal monitor. CdZnTe thin films with different thicknesses were deposited at 650-700 °C source temperature with 5 Å/s evaporation rate. The substrate was heated during deposition to improve the crystallinity of the film. The substrate and source temperatures were measured during the thin film deposition using type K (Nickel-Chromium/Nickel-Alumel) thermocouples.
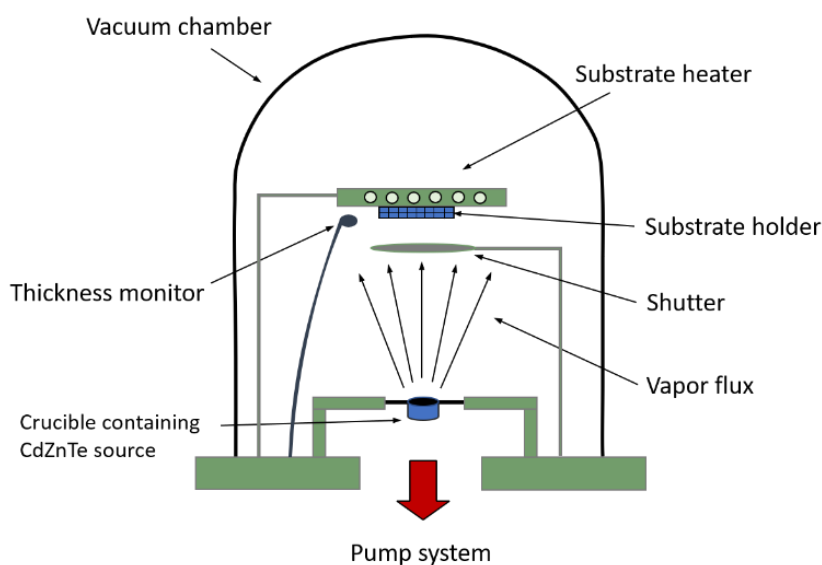
Figure 3.1. Thermal vacuum evaporation system for CdZnTe thin film deposition.

3.2 Post-Deposition Process for CdZnTe Thin Films

The annealing process and $CdCl_2$ treatment steps are the two main post-deposition processes performed to improve the structural properties of CdZnTe thin film and its device parameters. The main goal was not only to optimize the properties of the CdZnTe layer but also to activate the junction at the device interface.

Annealing is a temperature-based process that induces recrystallization and grain growth within material [57]. In this study, an annealing process was applied after every deposition step, including the CdS window layer, CdZnTe absorber layer, and Au back contact layer, to enhance the physical and chemical properties of deposited films. As-deposited CdZnTe samples were placed into the horizontal Lindberg type furnace and heated up to the predetermined temperatures changing from 100 °C to 300 °C for a time interval of 30 minutes under a nitrogen (N_2) gas atmosphere, which was maintained throughout the process to minimize the possible contamination from the ambient. After that, a gradual cooling procedure was performed to eliminate cracking or oxidations of the film surface. Additionally, Au contacts completing the device structure were annealed at 100 °C for 30 minutes to increase their ohmicity and adhesion properties.

In this study, $CdCl_2$ treatment followed by a post-annealing process was also performed to activate the junction between the CdS window and CdZnTe absorber layer, initiate recrystallization and grain growth of CdZnTe film, and reduction of the interface defects. Additionally, $CdCl_2$ treatment enhanced the p-type conductivity of CdZnTe film by forming Te rich surface and passivates the surface prior to metal formation. $CdCl_2$ treatment includes the following steps respectively: (1) immersing of glass/ITO/CdS and glass/ITO/CdS/CdZnTe thin films in a solution of 2.08 g $CdCl_2$ in 100 ml methanol for a few seconds; (2) annealing of the $CdCl_2$ treated glass/ITO/CdS/CdZnTe films both in N_2 atmosphere and air atmosphere at 350 °C for 10 minutes; (3) rinsing in water to eliminate $CdCl_2$ residues.

Several methods for wet CdCl$_2$ treatment have been suggested, including dipping the films into CdCl$_2$ solution or dropping CdCl$_2$ solution on the film surface, followed by an annealing process that can be performed at different temperatures for different periods of time in various atmospheres (air, vacuum, N$_2$, O$_2$, etc.) [58]. Oxygen usage in CdCl$_2$ treatment is highly encouraged for CdTe films since it enhances structural and electrical properties by incorporation of Cl and O [59]. However, when CdZnTe thin film is in concern, a careful investigation should be carried out due to the high affinity of Zn to O$_2$, resulting in n-type ZnO formation on the surface [60]. Furthermore, the complex reaction between CdZnTe and CdCl$_2$, which introduces a mixture on the surface having a low melting point, promotes a high degree of recrystallization and grain growth [59]. CdCl$_2$ treatment initiates three main reactions, including diffusion of Cd atoms into the material surface, converting Te precipitates into CdTe [61], and migration of Cl through grain boundaries. The complex chemical reactions when CdCl$_2$ is introduced into the system can be described by the following equations.

$$2Te + CdCl_2 \rightarrow CdTe + TeCl_2 \qquad \text{Equation 3.1}$$

$$Cd_{1-x}Zn_xTe + yCdCl_2 \rightarrow Cd_{1-x+y}Zn_{x-y}Te + yZnCl_2 \qquad \text{Equation 3.2}$$
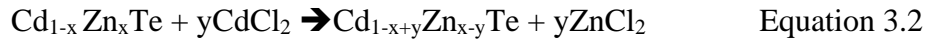
As a result, CdCl$_2$ treatment initiates ZnCl$_2$ formation, having a low melting point of 318 °C and high vapor pressure of 400 °C, resulting in an out-diffusion of Zn [62].

3.3   Back-Contact formation

The main problem correlated to CdTe and, consequently, CdZnTe is the complexity of achieving low-resistance stable ohmic contact [3]. The most used metals for non-rectifying contact are Cu/Au alloy and Au metal. Since Cu diffusion causes instabilities by extending deeply into the thin absorber layer [63], only Au metal was deposited as the back electrical contact to complete the device. Au metal was deposited as a back contact using thermal evaporation. After the deposition process, annealing at 100 °C was performed to initiate a chemical reaction and improve the

adhesion properties of Au [64]. Prior to metal deposition, $CdCl_2$ treatment was performed to generate Te rich surface, which resulted in a p-type conductive layer.

3.4 Thin Film Characterization Techniques

The growth mechanism and material properties of as-deposited, annealed, and $CdCl_2$ treated CdZnTe thin films were studied using various characterization techniques. In the following subsections, a general description of characterization techniques used to analyze CdZnTe thin films is described with their relevant working principles.

3.4.1 Thickness measurement

The exact determination of the film thickness plays a crucial role in data analysis of optical and electrical features. The thickness of the CdZnTe thin films was measured in-situ by monitoring the deposition rate via InficonXTM/2 quartz crystal monitor. After the deposition, the film thickness was also measured by Veeco DEKTAK 6M profilometer as a contact measuring system and ellipsometry as a non-contact measurement system. Particularly, the surface profilometer method is one of the most appropriate and advanced techniques to precisely establish film thickness. On the other hand, ellipsometry is a non-destructive tool that was employed not only to obtain the thickness of the film but also to determine the oxide thickness on the surface.

3.4.2 X-Ray Diffraction (XRD) Measurement

X-ray diffraction (XRD) technique was employed to uniquely identify crystalline phases and to determine the structural properties of a material, including preferred orientation, atomic spacing, phase composition, lattice constant, crystalline size, and dislocation density [65]. XRD identifies the crystalline phases of a material by comparing the measured diffraction pattern with known standards or International

Centre for Diffraction Data (ICDD) information cards. X-ray diffraction (XRD) measurement was performed using Rikagu Miniflex with Cu-Kα X-ray with a wavelength of λ=1.54 Å to verify crystallographic properties and structural parameters for CdZnTe thin film samples. All measurements were utilized using the same parameters with a diffracted 2θ-angle from 10 to 80° with a 4°/min scan speed. X-ray diffraction (XRD) study was performed on CdZnTe thin films, and various crystallographic aspects, including d-spacing, lattice constant, crystallite size, and dislocation density, have been calculated.

3.4.3   UV-Vis Spectrophotometer

Transmission measurement is a contactless and non-destructive optical analysis primarily employed to ascertain the absorption coefficient and bandgap energy of a material [49]. Optical transmission measurements were carried out using a Perkin-Elmer LAMBDA 45 UV/Vis spectrophotometer between 300 and 1000 nm. During the transmission measurements, reference measurement using glass substrate for background correction was essentially utilized.

3.4.4   Raman Spectroscopy

Raman spectroscopy is an optical scattering method employed to obtain information about the vibrational behaviors of the optical phonons in a crystalline lattice [66]. Raman scattering is detected by the shift in frequency between incident light and inelastically scattered light from the surface [67]. During the scattering, the dominant process, called Rayleigh scattering, is an elastic scattering process where there is no frequency difference between the incident and the scattered light from the sample. However, there is also an inelastic scattering process in which there is a vibrational frequency shift between incident light and molecule or molecule and scattered light. This inelastic scattering process describes the Raman scattering [66]. Raman scattering is expressed as a shift in frequency in wavenumbers (cm^{-1}). Various crystal

phases possess unique molecular vibrational behaviors, raising certain Raman shifts, which provide exceptional information about crystal structure, phonon dispersion, composition, and electronic states [32]. Horiba-Jobin Yvon iHR550 imaging spectrometer system, which was equipped with a three-grating monochromator, Mpc6000 power supply, Peltier CCD camera, and Ventus532 laser source, was used to study lattice vibrations of CdZnTe thin films.

3.4.5   Spectroscopic Ellipsometry

Ellipsometry is a nondestructive, effective tool that is employed to obtain the optical properties, including refractive index, extinction coefficient, complex dielectric functions, absorption coefficient, roughness, and layer thickness [1]. The working principle of ellipsometry involves generating a light beam and reflecting it from the material and assessing variation in the polarization of the reflected beam as a function of wavelength [68][69]. The measured data are traditionally expressed as two ellipsometric angles (ψ, Δ) or the equivalent quantities α and β, ($\alpha = \cos 2\psi$, and $\beta = \sin 2\psi \cos \Delta$). These ellipsometric parameters contain the information related to the optical properties of the material. In our experiment, ellipsometric spectra, α and β, are acquired as a function of photon energy. When measured α and β are fitted to a physical model of the layer, detailed material properties is determined [70]. To acquire optical constants of the CdZnTe thin films, a surface model was employed. Values of both dielectric functions of CdZnTe and its native oxides were finetuned in the final LMA (The Levenberg-Marquardt algorithm) fitting process of the analysis. Ellipsometer experiments were completed at room temperature with energy range of 1.23–3.49 eV by SOPRA GES-5E ellipsometer. The ellipsometer measurements were carried out at incidence angle, $\phi \approx 69°$ (Si Brewster angle, increase sensitivity in film parameters) [71].

3.4.6   X-ray Photoelectron Spectroscopy (XPS)

X-ray photoelectron spectroscopy (XPS) allows for identifying elemental composition, chemical states, and chemical bonding and determining the binding states of the elements from the surface of a material [49]. Additionally, XPS is also used for depth profiling by counting elements as a function of depth. PHI 5000 VersaProbe system equipped with Mg Kα X-ray source in ultra-high vacuum condition was used in METU Central Laboratory. To eliminate the energy shift in the binding energies due to the charging effect, XPS data was adjusted by correcting the C 1s photoelectron peak at 284.8 eV as a reference. First, a survey measurement was performed by scanning the surface of the CdZnTe thin films up to 1150 eV to obtain a general picture of the XPS spectra. After that, the acquired elements in these spectra were scanned in more specific energy ranges for further comprehensive data. Additionally, depth profiling was performed using an Ar ion gun by sputtering the surface of the film to obtain the atomic compositions and stoichiometry of the subsurface regions of CdZnTe thin films.

3.4.7   Scanning Electron Microscopy (SEM)

SEM enables not only to obtain images of specific locations on the surface of the thin film down to the nanometer scale but also to examine the microstructure properties of the film. Additionally, SEM is equipped with an energy-dispersive X-ray detector, utilized for exploring regional elemental compositions in thin films [72]. In this work, the surface morphology of CdZnTe thin films was investigated using Quanta 400F FE-SEM in METU Central Laboratory and Zeiss EVO HD SEM in GÜNAM Laboratory. SEM analysis also provided the possibility to investigate grains and grain boundaries, voids, and cracks on the surface of CdZnTe.

3.4.8 Energy Dispersive X-ray Spectroscopy

EDS was employed to reveal the elemental composition of CdZnTe films by bombarding the surface with a high-energy electron beam. Due to the collision of electrons with atoms from the subsurface region, X-rays whose wavelength is distinctive for each element in concern are produced. Generated X-rays are then collected and evaluated in terms of their energies and intensities. In this study, the Ametek EDAX system was employed to comprehend the effect of deposition parameters and post-deposition processes on the chemical composition of CdZnTe.

3.4.9 Atomic Force Microscopy (AFM)

AFM was employed for a detailed characterization of the surface morphology of CdZnTe thin film samples, which had nonuniform surface topography involving grains, grain boundaries, defects, impurities, voids, and cracks at the submicron scale. Nanomagnetics ambient AFM system was used to analyze the surface morphology of the CdZnTe thin films. The advantage of using AFM as a surface characterization tool is that it can provide 3D topographic images with a high resolution of surface morphology.

3.4.10 Hall Effect Measurement

The most essential feature of a semiconductor material is that it could be doped with different types and concentrations of impurities (donors or acceptors) to modify its electrical conduction mechanism for a specific application. Charge carriers (electrons and holes) in a semiconductor material and the density of these carriers is a crucial parameter as the current is mainly defined by the number of electrons in CB and holes in VB [45]. Measuring resistivity, carrier density, carrier type, and mobility of the semiconductor material is a critical step necessary for exploring the electrical characteristics properties [73]. Therefore, the Hall effect measurement was

41

employed utilizing Van der Pauw geometry. The Hall effect phenomenon results from the forces exerted on moving charges by the applied magnetic field perpendicular to the surface of the semiconductor sample [45]. When the charges are deflected by the Lorentz force, a Hall voltage is induced between the opposite sides of the semiconductor sample. In this study, Hall effect measurements were utilized at room temperature conditions using the Nanomagnetics Hall Effect system. The current was applied, and the resulting voltage was measured. Hall voltage was measured along the diagonals of the CdZnTe thin film samples (current through contacts 2 and 4, voltage measured between 1 and 3, and vice versa) by applying a constant current under two conditions: with and without magnetic field. The Hall coefficient can be calculated at the end of the measurements by the differences between the voltages along the diagonals measured with and without magnetic. The Hall coefficient between the opposite sides of the semiconductor sample is given as

$$R_H = \frac{t}{B}\frac{V_H}{I} \qquad\qquad \text{Equation 3.3}$$

where t is the film thickness, V_H is the Hall coefficient, B is the applied magnetic field, I is the applied constant current [31]. Additionally, the polarity of R_H gives the conductivity type of the semiconductor as $R_H > 0$ for holes, $R_H < 0$ for electrons. Using the Hall coefficient, both the concentration of charge carriers and the Hall mobility of a semiconductor can be calculated. Therefore, the charge carrier concentration, N, is determined by

$$N = \frac{1}{qR_H} \qquad\qquad \text{Equation 3.4}$$

The Hall mobility can also be deduced by

$$\mu = \frac{R_H}{\rho} \qquad\qquad \text{Equation 3.5}$$

where ρ is the resistivity of the semiconductor. Hence, once V_H and resistivity ρ are established, N and μ of the semiconductor can be obtained.

3.5 Device Characterization Techniques

To fully understand the device performance of CdZnTe thin film-based heterojunctions, device characterization methods, including temperature-dependent dark current-voltage (I-V), frequency-dependent capacitance-voltage (C-V), and solar cell measurements, have been employed.

i. Current-Voltage

Temperature-dependent dark current-voltage analyses were performed to study the rectifying behaviors of CdZnTe/Si heterojunction and to investigate the current conduction mechanism of the device. These measurements were conducted at a temperature between 220-340 K for bias voltage interval at $\pm$ 3 V.

ii. Capacitance-Voltage

Admittance measurements enable measuring important physical parameters and analyzing the quality and junction properties of the semiconductor materials. It was utilized to ascertain material and process parameters, including doping concentration, the density of interface traps, series resistance, and barrier height [2]. Room temperature C-V and G-V measurements for CdZnTe/Si heterojunction devices were employed for frequencies from 1 kHz to 1000 kHz.

iii. Solar Cell Measurements

The performance of the CdS/CdZnTe heterojunction solar cells was measured by using the Newport Solar Simulator system with a high-intensity Xenon Arc lamp of AM1.5 condition. The main solar cell parameters include open-circuit voltage (V_{oc}), short circuit current (I_{sc}), series resistance (Rs), shunt resistance (Rsh) and fill factor (FF) of CdS/CdZnTe solar cells were obtained.

CHAPTER 4

OPTIMIZATION AND CHARACTERIZATION OF CADMIUM ZINC TELLURIDE THIN FILMS

Substrate temperature, film thickness, post-deposition annealing process, and Cadmium Chloride ($CdCl_2$) treatments are crucial optimization parameters for manufacturing CdZnTe thin film solar cells. These parameters have significant effects on the physical properties of CdZnTe used as an absorber layer. Accordingly, CdZnTe thin films were fabricated using a thermal evaporation technique with two different substrate temperatures. It was observed that crystalline quality was enhanced with elevating substrate temperatures. Additionally, various film thicknesses have been investigated. Good structural and optical properties have been achieved for films with less than 2.0 µm thickness. Semitransparent thin films (≤2.0 µm) had a transmittance value greater than 75% in the near-infrared region, around 1000 nm. Different annealing treatments were also carried out to determine their effect on the film properties. The quality of the film was examined to improve with increasing annealing temperature. Finally, $CdCl_2$ treatment has been studied, which is considered a vital process for the re-crystallization of the film. A significant change in structural, morphological, optical, and electrical transport properties was observed with $CdCl_2$ treatment. Structural properties such as lattice constant, inter-planar spacing, average crystalline size, dislocation density, and strain were also calculated and found to be strongly dependent on the parameters, which were the substrate temperature, film thickness, annealing, and $CdCl_2$ treatment. Therefore, optimization studies have been conducted, and CdZnTe thin films have been characterized regarding their structural, optical, morphological, and electrical transport properties.

4.1 Introduction

The growth mechanism and material properties of CdZnTe thin films have been studied using various investigative characterization techniques. The optimization process for CdZnTe thin films is the most critical aspect of controlling material processing and standardized device performance. Before using CdZnTe thin films in device applications, characterization of the films must be completed to achieve optimum performance.

The thermal evaporation technique was used to produce CdZnTe thin films for solar cell application thanks to its efficiency, good reproducibility, and low cost. It also poses several options to adjust preparation parameters. The effect of the deposition parameters, including various film thicknesses and substrate temperatures, was investigated. Additionally, the effect of post-deposition parameters such as annealing and $CdCl_2$ treatment was also studied. The complete characterization of CdZnTe thin films included compositional characterization, phase, and structural analysis, surface characterization, optical and electrical analysis were carried out by X-ray diffraction (XRD), Raman spectroscopy, Energy Dispersive X-ray Spectroscopy (EDS), scanning electron microscope (SEM), Atomic force microscope (AFM), UV-Vis Spectroscopy and Hall effect measurement.

4.2 Experimental Details

CdZnTe thin films were deposited on glass substrate using copper shadow masks by thermal evaporation technique with beneficial optical and electrical properties and accurate surface morphology. The deposition conditions, including substrate temperature and thickness of the films with an optimized evaporation rate, have been investigated in detail. Glass cleaning is essentially required for the fabrication of high-quality CdZnTe thin films. Therefore, prior to deposition, glass substrates were cleaned in an ultrasonic bath using acetone, isopropyl alcohol, and distilled water

and dried under N_2 gas. The dimension of all substrates was 20mm$\times$20mm and attached to the substrate holder.

The first study investigated the variation of the substrate temperature while keeping all other deposition parameters constant. Therefore, CdZnTe thin films were deposited at different substrate temperatures, room temperature and 150 °C. The thickness of CdZnTe thin films was 2 µm. The second study analyzes the effect of the thickness of the films on the physical parameters of CdZnTe. The investigated films, deposited at room temperature under the same vacuum pressure conditions, had thicknesses of approximately ~0.5, ~1.0, ~2.0, and ~4.0 µm measured by the Dektak profilometer. Afterward, to study annealing treatment, as-deposited films with ~1.0 µm thickness were annealed at 100 °C, 200 °C, and 300 °C in a furnace for 30 min under a Nitrogen atmosphere. Finally, 1.0 µm thick CdZnTe films with relatively poor physical properties were dipped into a solution of 2.08 g $CdCl_2$ in 100 ml methanol solution for a few seconds and annealed at 350 °C for 10 min under both Air and N_2 atmosphere. In addition, Hall effect measurement was utilized to determine the type of charge carriers, carrier concentration, electrical conductivity, and resistivity of CdZnTe films.

4.3   Result and Discussion

4.3.1   Effect of Substrate Temperature

To investigate the effect of substrate temperature on CdZnTe thin films, two different substrate temperatures have been employed at room temperature (RT) and 150 °C while keeping all other deposition parameters constant. The effect of substrate temperature on the phases and structure's parameters was studied by X-ray diffraction (XRD) analysis. Figure 4.1 reveals the X-ray diffraction pattern of CdZnTe films which are polycrystalline with a predominant cubic zinc blende structure having a preferred (111) orientation (ICDD database: $Cd_{0.96}Zn_{0.04}Te$ PDF card no.; 00-053-0555) [74]–[76]. The intensity of (111) peak was noticed to increase

with increasing substrate temperature, attributed to improvement in crystallinity. The other diffraction peak was located at ~76.6 °, corresponding to CdZnTe (333) orientation. An additional small peak was observed at ~21.5° for both films, corresponding to CdTeO$_3$ and/or TeO$_2$ secondary phases (ICDD database: CdTeO$_3$ PDF card no.; 00-036-0890 or TeO$_2$ PDF Card No.:00-041-0945) probably due to the oxidation of the surface after the deposition process [77]. Sharp and symmetrical peaks indicated high homogeneity and good crystal quality of CdZnTe thin films [75].
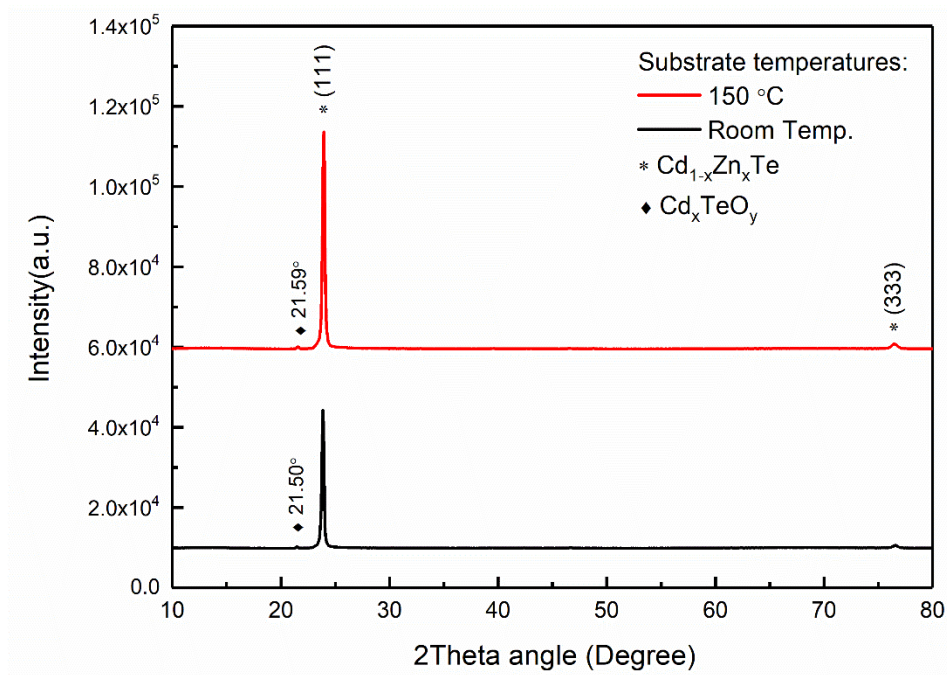
Figure 4.1. XRD patterns of CdZnTe films deposited at different substrate temperatures, room temperature, and 150 °C.

Moreover, the XRD spectral analysis allows obtaining valuable information about several crystallographic properties of CdZnTe thin films, including crystal phases, crystalline size evolution, lattice constants, and dislocation densities. Accordingly, the general relationship between the inter-planar spacing, d, wavelength of the incident X-ray, λ, and the angle of incident, θ, which is known as Bragg's law

$$n\lambda = 2d_{hkl} \sin \theta_{hkl} \qquad \text{Equation 4.1}$$

48

where n is the order of reflection, $\lambda = 1.54$ Å is the wavelength of the incident X-rays, d_{hkl} is the interplanar spacing of the crystal and θ_{hkl} is the angle of incidence. The lattice constant for Cubic crystal systems can be calculated from

$$a = d_{hkl}\sqrt{h^2 + k^2 + l^2} \qquad \text{Equation 4.2}$$

The average crystalline size can be obtained by the Debye-Scherrer equation as

$$D = \frac{0.94 \times \lambda}{\beta_{(2\theta)} \cos\theta} \qquad \text{Equation 4.3}$$

where $\beta_{(2\theta)}$ is the peak width (Full Width at Half Max (FWHM) in rads). Finally, dislocation density can also be calculated using Williamson and Smallman's relation

$$\delta = \frac{1}{D^2} \qquad \text{Equation 4.4}$$

And the micro-strain resulting from defects and deformation, ε, can be calculated using the following formula

$$\varepsilon = \frac{\beta_{(2\theta)}}{4\tan\theta} \qquad \text{Equation 4.5}$$

Using these relations, various structural parameters, including lattice constant, average crystalline size, dislocation density, and micro-strain values for CdZnTe films deposited at different substrate temperatures, were calculated and tabulated in Table 4.1. The angular 2θ position for the (111) peak was observed to shift slightly towards the higher side as the substrate temperature increased in addition to the decrease in the corresponding lattice constant of the cubic phase from 6.45 Å to 6.43 Å. Additionally, the average crystalline size was also monitored to improve noticeably from 36.9 nm to 43.7 nm with substrate temperature. As substrate temperature was raised, the adatom mobility and diffusion rate of adatoms also increased [78], resulting in the crystalline formation and increasing crystalline size by producing a dense microstructure [79]. The mobility of the adatoms dominates the nucleation and crystallization process during the deposition, and it could be manipulated by varying substrate temperature, vapor pressure, and thermal

properties of the source material [79]. The decrease in dislocation density and micro-strain at higher substrate temperatures may be due to improvement of crystallinity and reduction of point defects.

Table 4.1 Structural parameters of CdZnTe films deposited at different substrate temperatures.

Parameters	Room temperature	150 °C
2θ *of* (111) *peak degree* (°)	23.9	23.9
d-value (Å)	3.72	3.71
Lattice constant (Å)	6.45	6.43
FWHM (°)	0.24	0.19
Crystalline size (nm)	36.9	43.7
Dislocation density δ ($\times 10^{10}\ cm^{-2}$)	7.4	5.2
Micro-strain ε ($\times 10^{-3}$)	4.8	3.9

Raman analysis was also performed to analyze vibrational modes and to confirm the structure of CdZnTe thin films deposited at room and 150 °C substrate temperatures, which is shown in Figure 4.2. Peaks in the Raman spectrum were associated with CdTe-like transverse (TO_1) optic and longitudinal (LO_1) optic phonon modes of CdZnTe [32], [80], [81], [82] and ZnTe-like LO_2 phonon mode of CdZnTe [82], [83]. Additionally, Raman spectra of CdZnTe thin films also revealed second-order phonons with a quite smaller intensity of CdTe-like $2TO_1$ and ZnTe-like $2LO_2$ resonant overtones [74], [84]. The clear presence of CdTe and ZnTe-related modes of CdZnTe on Raman spectra confirm that CdZnTe thin films had a high degree of crystalline structure, which has also been verified by XRD analysis [82]. Moreover, there was an increase in the intensity of ZnTe-like modes as the substrate temperature increased, indicating a structural change due to the increase in zinc concentration with substrate temperature. The additional peak located at 128 cm^{-1} was associated

with the A_1 mode of Tellurium arising from the movement of the Te atoms in the basal plane [85], [86], [81], [87]. This Te-related mode most likely originated from oxidation of the film surface as TeO_2, which was also detected in the XRD analysis. Another possible source for the A_1 Te mode was the Te precipitates in the structure.
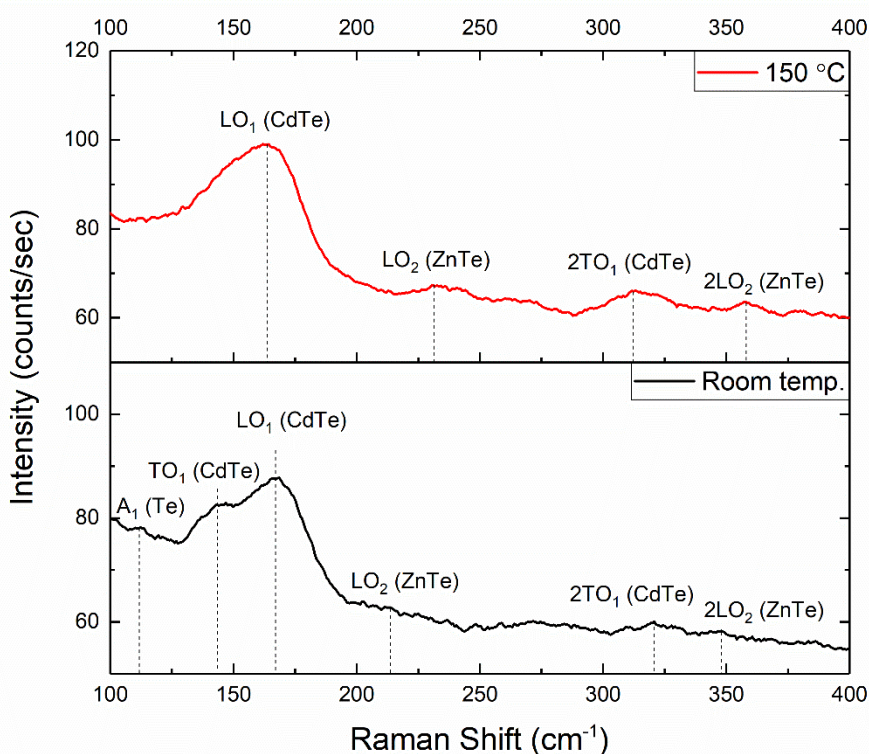
Figure 4.2. Raman spectra for different substrate temperatures using 532 nm laser excitation source.

Identification of phases and chemical composition analysis of deposited CdZnTe films were studied by Energy Dispersive X-ray (EDS) analysis. The elemental content in the film's structure and changes in the atomic percentage of these elements regarding variation in substrate temperature were evaluated in detail and tabulated in Table 4.2. It was observed that as the substrate temperature increased, a slight increase was observed in the atomic percentage of Zn, while a slight decrease was found in the atomic percentage of Cd and Te elements. These changes were usually expected since the vapor pressures and sticking coefficients between these elements were changed with different substrate temperatures.

51

Table 4.2 EDS analysis of CdZnTe films deposited at different substrate temperatures.

Substrate Temperature	*Cd* (at. %)	*Te* (at. %)	*Zn* (at. %)	*x* Zn/(Zn+Cd)
Room temperature	42.11	52.79	5.10	0.11
150 °C	41.73	52.54	5.73	0.12

EDS results show minor changes in the concentration of elements with increasing substrate temperature. Zn concentration slightly increased with increasing substrate temperature, which can be explained by the difference in lattice constant. The Zinc concentration of $Cd_{1-x}Zn_xTe$ thin films, assigned as '*x*' was determined to be nearly 10% by EDS analysis. The lattice constant obtained from EDS analysis was calculated to be 6.44 Å and 6.43 Å for CdZnTe thin films deposited at RT and 150 °C substrate temperatures, respectively. The decrease in the calculated lattice constants with increasing substrate temperature was nearly consistent with the results acquired by the XRD analysis. Both XRD, Raman, and EDS analyses revealed the highly crystalline quality of CdZnTe thin films with increasing Zinc concentration as the substrate temperature raised up.

Morphological characterization for CdZnTe thin films deposited at RT and 150 °C substrate temperatures was conducted using SEM analysis. The SEM images of CdZnTe thin films were presented in Figure 4.3, revealing that both films with different substrate temperatures were found to be homogenous and uniform with a smooth surface morphology and defects like pinholes and cracks were not observed. Figure 4.3 indicates the recrystallization of CdZnTe and grain growth with increasing substrate temperatures which was consistent with the trend in crystalline size as illustrated by the XRD analysis.
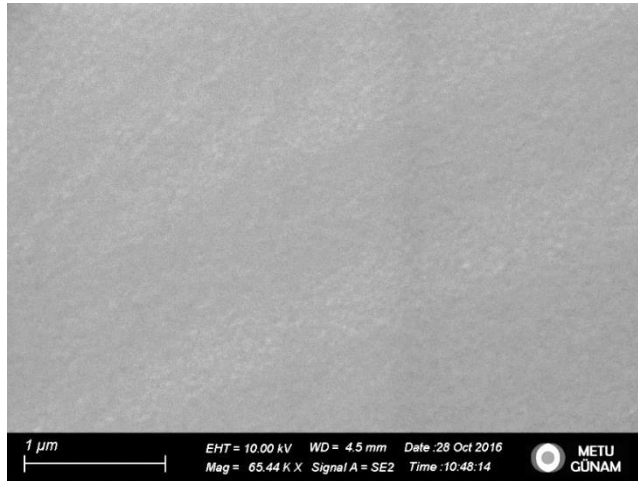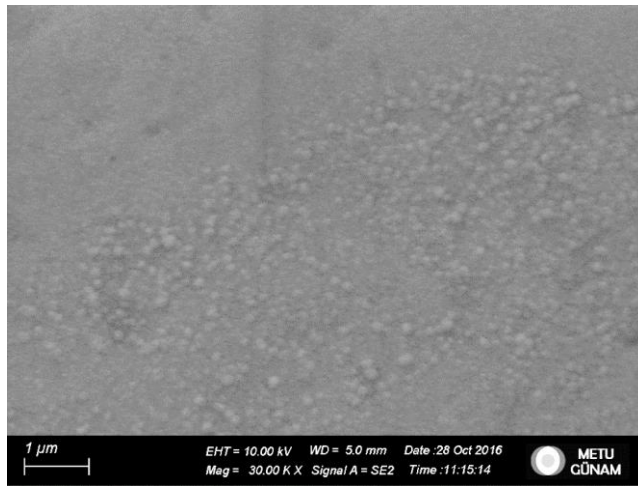
Figure 4.3. SEM images of CdZnTe films deposited at substrate temperatures of a) room temperature and b) 150 °C.

In order to analyze the optical features of the CdZnTe thin films at various substrate temperatures, transmittance measurements were carried out. Accordingly, the band gaps and absorption coefficients of the films were obtained in addition to the wavelength dependence of the transmittance spectrum. Figure 4.4 (a) illustrates the transmittance behavior of CdZnTe thin films. A slight decrease was detected in the transmission for CdZnTe deposited at 150 °C. Both films were highly transparent between 850-1000 nm with maximum transmittance of 90% and had a sharp cut-off at about 800 nm. Interference fringes were also detected in the transmittance measurements with subsequent uniform maxima and minima, revealing the optical

uniformity and thickness equality of the CdZnTe thin films [88]. The energy bandgap was verified by extrapolating the Tauc plot, $(\alpha h\nu)^2$ vs. $h\nu$, for zero absorption and indicated in the inset of Figure 4.4. The bandgap energies were found as 1.55 eV and 1.54 eV for the CdZnTe thin films deposited at RT and 150 °C, respectively. The optical energy bandgap was monitored to decrease slightly for elevated substrate temperature, attributed to a slight stoichiometric deviation. A comparable reduction in bandgap with an increase in substrate temperature has also been documented in CdTe thin films fabricated using thermal evaporation [89].
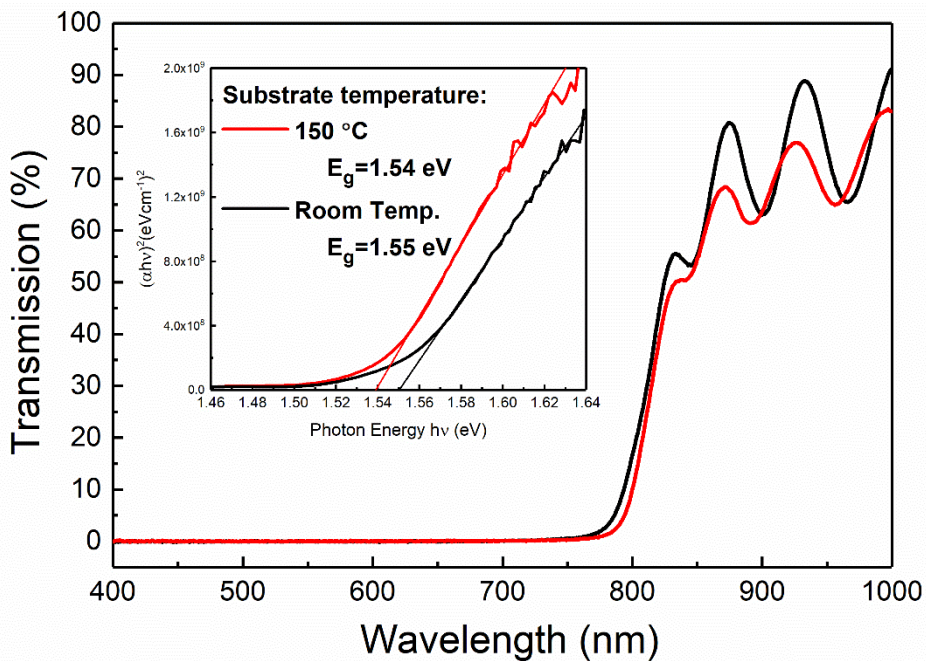
Figure 4.4. Transmission spectra and $(\alpha h\nu)^2$ vs. $h\nu$ plots for CdZnTe films deposited at room temperature and 150 °C.

4.3.2   Thickness Analysis

Four different depositions have been conducted to investigate the thickness variation of CdZnTe thin films. All deposition parameters, including deposition rate, chamber pressure, source temperature, and the distance between the source and substrate holder, were identical except for the deposition time to reach the desired thickness.

Accordingly, CdZnTe thin films having thicknesses of ~0.5, ~1.0, ~2.0, and ~4.0 μm were investigated regarding structural and optical analysis using XRD and transmission measurements. The phases and structural parameters of CdZnTe thin films with different thicknesses have been studied in detail. Figure 4.5 illustrates XRD patterns of as-deposited CdZnTe thin films for various thicknesses.
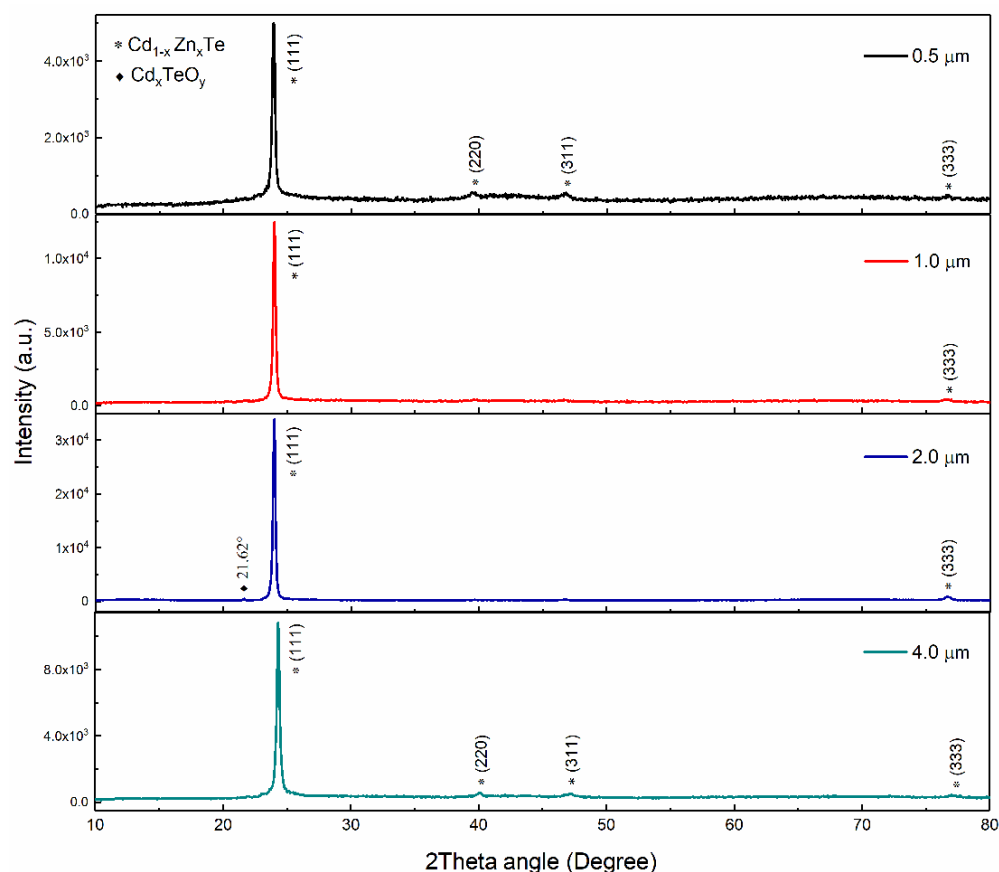
Figure 4.5. XRD pattern for various thicknesses of CdZnTe thin films.

As illustrated in Figure 4.5, the XRD pattern revealed that each film has polycrystalline nature with the preferred CdZnTe (111) orientation of zinc blend structure. Another diffraction peak with a much lower intensity was observed at a 2θ position of ~76.8°, corresponding to CdZnTe (333) orientation. It was noticed that the angular positions of (111) peaks shift slightly to the upper side as the film thickness increases. An additional insignificant peak was observed for all thicknesses of CdZnTe thin films at ~21.6°, corresponding to $CdTeO_3$ and/or TeO_2 secondary

phases, indicating the oxidation of the surface after deposition probably due to the storage conditions. Furthermore, CdZnTe thin films with 0.5 µm and 4.0 µm thicknesses had additional diffraction peaks at ~39.4° and 46.5°, corresponding to CdZnTe (220) and CdZnTe (311) orientations, respectively.
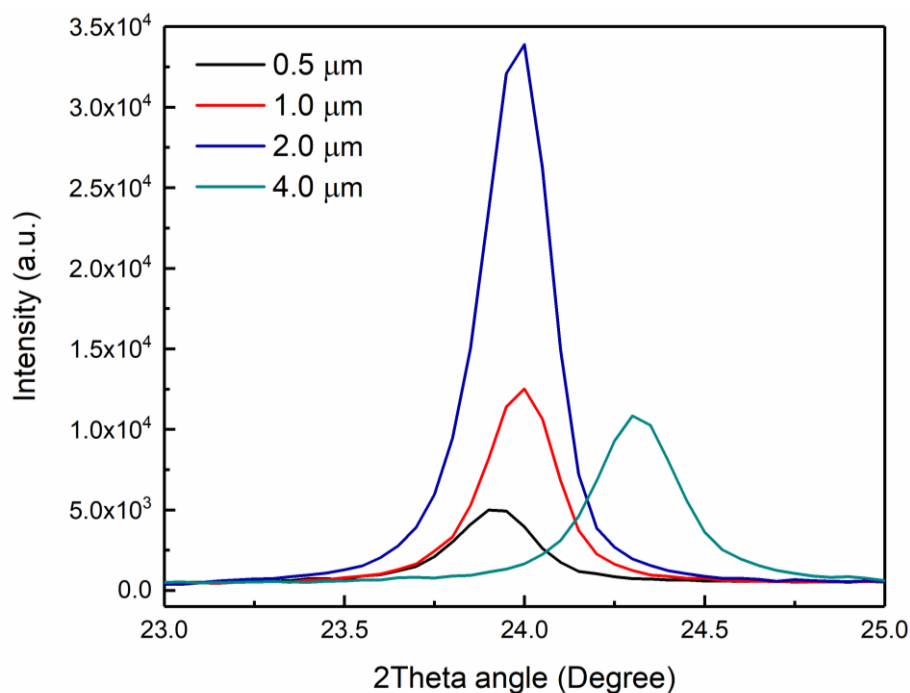
Figure 4.6. Preferred (111) orientation for various thicknesses of CdZnTe thin films.

Moreover, Figure 4.6 shows the peak intensity of the preferred (111) orientation, increasing for higher thicknesses up to 2.0 µm with successful deposition. On the other hand, in the film with 4.0 µm thickness, the intensity of the (111) peak decreased, revealing poor crystallinity. CdZnTe thin film with 4.0 µm thickness also exhibited poor adhesion properties.

The XRD analysis was also employed to obtain crystallographic features of CdZnTe thin films with different thicknesses, such as the crystalline size evolution, the lattice constants, the dislocation densities, and micro-strain. The calculated structural parameters using XRD spectra are given in Table 4.3. The results indicated that 1.0 µm thick CdZnTe thin film had similar structural properties to 2.0 µm thick CdZnTe thin film. The crystalline size slightly increased as the film thickness increased.

Additionally, a slight decrease was observed in dislocation density and micro-strain values up to 2.0 μm thickness, thanks to the improved crystallinity and increased crystalline size. Deterioration in structural parameters was noticed for CdZnTe thin film with 4.0 μm thickness, probably due to the poor adhesion properties.

Table 4.3 Structural parameters of various CdZnTe thin film thicknesses.

Parameters	0.5 μm	1.0 μm	2.0 μm	4.0 μm
2θ of (111) peak degree (°)	23.9	24.0	24.0	24.3
d-value (Å)	3.72	3.71	3.71	3.66
Lattice constant (Å)	6.44	6.42	6.42	6.34
FWHM (°)	0.23	0.22	0.22	0.25
Crystalline size (nm)	36.7	38.2	38.5	33.9
Dislocation density δ ($\times 10^{10}\ cm^{-2}$)	7.4	6.9	6.7	8.7
Micro-strain ε ($\times 10^{-3}$)	4.8	4.6	4.5	5.1

The effect of various thicknesses of CdZnTe thin films on optical properties was investigated using transmittance measurements. Figure 4.7 illustrates the transmittance behavior of CdZnTe films of different thicknesses, and transmittance spectra show sensitivity to the disparity in the film thickness. The transmittance was monitored to decrease as the thickness of the film increased, and the appearance of interference fringes revealed the homogenous nature of CdZnTe thin films. Semitransparent thin films (≤2.0 μm) had a transmittance value higher than 75% in the near-infrared region, around 1000 nm. The approximate bandgaps of the films were obtained by extrapolating the Tauc plot of $(\alpha h\nu)^2$ vs $(h\nu)$ for zero absorption and demonstrated in Figure 4.8. The bandgap energies were 1.57, 1.53, 1.56, and 1.54 eV for the ~0.5, ~1.0, ~2.0, and ~4.0 μm thick CdZnTe thin films, respectively. Variation in the optical energy bandgap with respect to thickness showed no apparent relation, probably due to the deviation in the stoichiometry of the films.
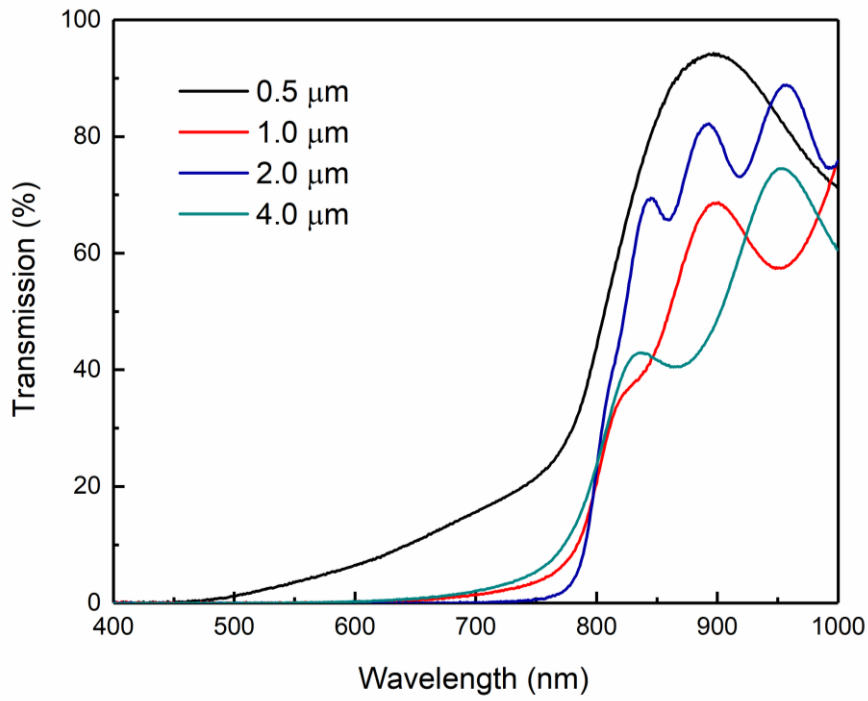
Figure 4.7. Transmission spectra of various CdZnTe thin film thicknesses.
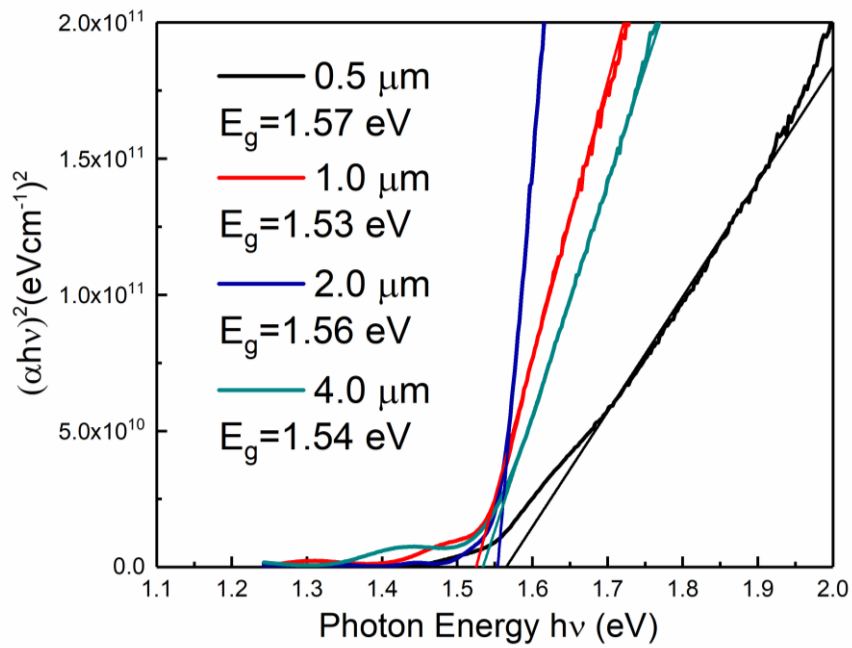
Figure 4.8. (αhν)² vs. hν plots for various thicknesses of CdZnTe thin films.

4.3.3 Annealing Treatment

Post-deposition annealing treatment was conducted at 100, 200, and 300 °C temperatures for 30 min under a Nitrogen atmosphere. Structural analysis of as-deposited and annealed CdZnTe thin films was performed by XRD measurement. As shown in Figure 4.9, all CdZnTe films were polycrystalline with a preferred (111) orientation. Additional diffraction peaks were also observed at angular positions of 39.4°, 46.5°, and 76.2°, corresponding to cubic CdZnTe (220), (311), and (333) orientations, respectively. The small peak at ~21.5° corresponds to $CdTeO_3$ and/or TeO_2 secondary phases. The annealing process at 300 °C initiates new diffraction peaks appeared at 56.9°, 62.6°, and 71.4°, corresponding to cubic CdZnTe (400), (331), and (422) orientations, respectively. These new diffraction peaks might be a sign of phase variation at high annealing temperatures. Additional peaks at ~21.5°, 23.1° corresponded to $CdTeO_3$, while 38.4° to TeO_2 secondary phases due to oxidation of the surface.

Figure 4.10 illustrates a significant change in the position and intensity of the (111) diffraction peak after 200 °C annealing. This considerable increase in the intensity of the preferred (111) orientation showed the change in the composition and the high degree of crystallinity of CdZnTe thin film at 200 °C annealing temperature. Additionally, using XRD spectra, the lattice constants, average crystalline size, and dislocation densities for CdZnTe thin films were calculated and presented in Table 4.4. A significant decrease was observed in the FWHM, which indicated the reduction in the lattice imperfections. A minor decrease in dislocation density and micro-strain after annealing was attributed to the lattice strain relaxation, improved crystallinity, and increase in crystalline size. The average crystalline size has increased noticeably from 32.7 nm to 47.6 nm with increasing annealing temperature. The XRD analysis has revealed that the annealing procedure enhances the crystalline quality of CdZnTe thin films.
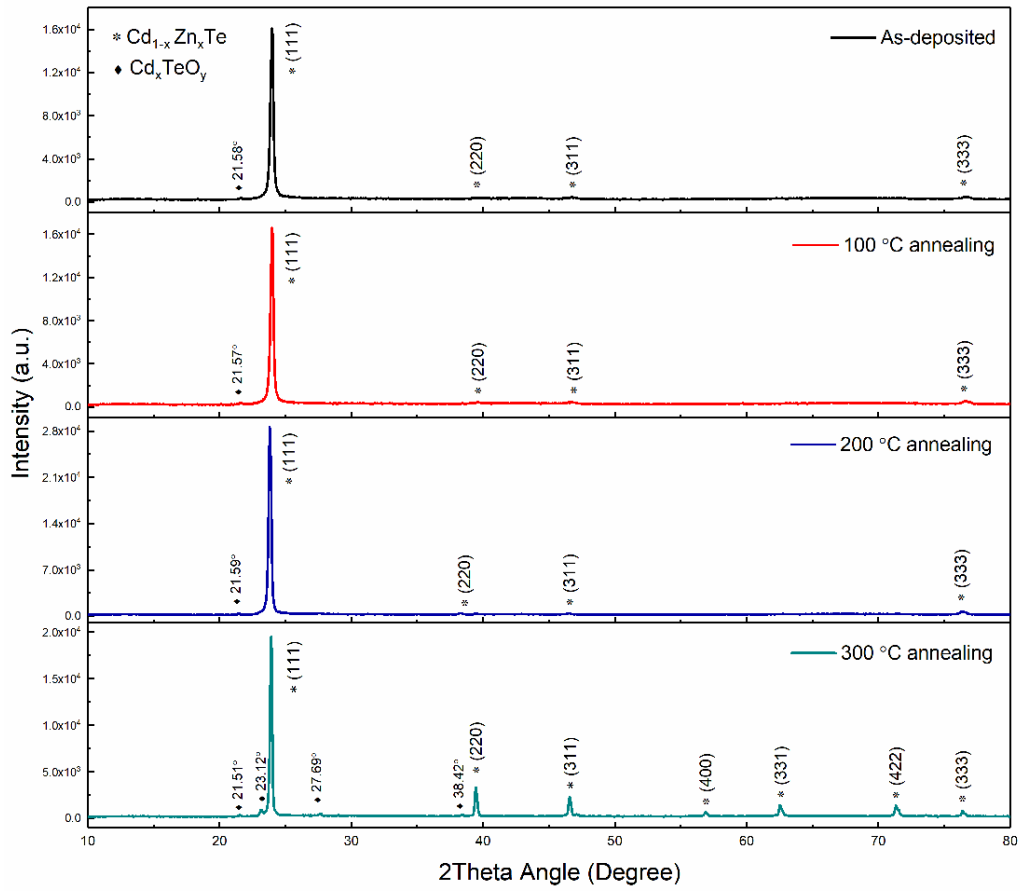
Figure 4.9. XRD patterns of CdZnTe films for different annealing temperatures.
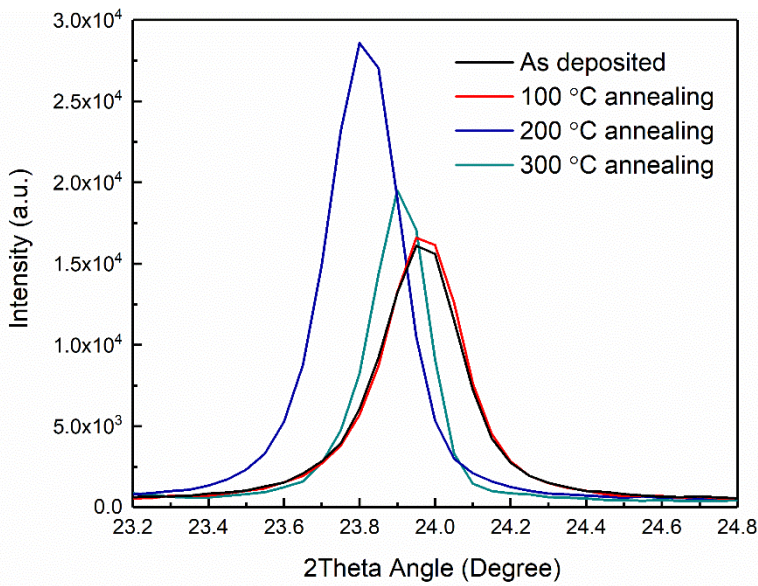
Figure 4.10. Preferred (111) orientations for different annealing temperatures.

60

Table 4.4 Structural parameters of CdZnTe thin films for different annealing temperatures.

Parameters	As deposited	100 °C annealing	200 °C annealing	300 °C annealing
2θ of (111) peak degree (°)	24.0	24.0	23.8	23.9
d-value (Å)	3.71	3.71	3.73	3.72
Lattice constant (Å)	6.43	6.43	6.47	6.44
FWHM (°)	0.26	0.24	0.23	0.18
Crystalline size (nm)	32.7	35.3	37.7	47.6
Dislocation density δ ($\times 10^{10}$ cm^{-2})	9.3	8.0	7.1	4.4
Micro-strain ε ($\times 10^{-3}$)	5.3	4.9	4.7	3.7

Figure 4.11 shows the Raman analysis, which was also performed to analyze the change in the vibrational modes and the CdZnTe structure with the annealing process. As-deposited and 100 °C annealed films have a broad peak located at ~162 cm^{-1}, associated with CdZnTe longitudinal optical (LO) phonon. For high annealing temperatures, i.e., 200 and 300 °C, two additional sharp and intense peaks were observed. The first peak was located at ~123 cm^{-1}, related to the A1 mode of the Tellurium Raman peak. The A1 mode of Te peaks was considered to be a result of Te precipitates inside and along the surface of the films, which were initiated by aggregation of the Te$_2$ molecules during the annealing process at high temperatures. Te precipitates were randomly initiated as nanocrystallites, and they had a larger scattering cross-section resulting in a higher Raman intensity, which did not show comparable material content for Te and CdZnTe in the film. The intensity of this peak has decreased sharply after annealing for a higher temperature of 300 °C, which

means that the oxidation reaction started to occur, also confirmed by XRD analysis. The additional Raman peaks at ~290 and ~393 cm^{-1} were assigned to the bending vibrations of the Te–O–Te in TeO$_2$ [61]. The second intense peak at ~141 cm^{-1} was related to the transversal optic (TO) phonon of CdZnTe. Raman spectra of CdZnTe thin films have also revealed the ZnTe-like TO$_2$ and LO$_2$ phonon modes in addition to second-order phonons CdTe-like 2TO$_1$ and ZnTe-like 2TO$_2$ and 2LO$_2$ resonant overtones with quite smaller intensities when compared to CdTe-like phonon modes [74], [82], [84]. The sharp increase in the intensity of CdTe and ZnTe-related modes of CdZnTe with increasing annealing temperatures confirms that films have a high degree of crystalline structures, which was verified by XRD analysis [82]. Moreover, there was an increase in the intensity of ZnTe-like TO$_2$ and LO$_2$ modes as the temperature increased, indicating a structural change probably due to the increase in zinc concentration with annealing.
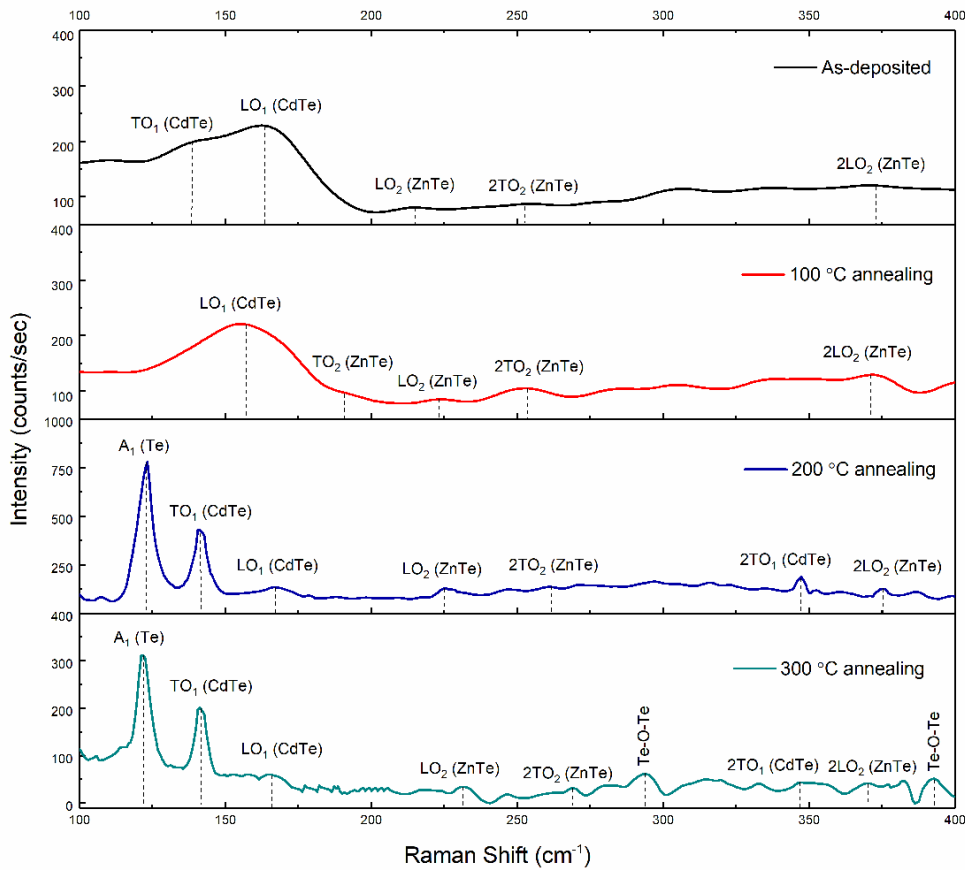
Figure 4.11. Raman spectra of CdZnTe films for different annealing temperatures.

62

EDS analysis was performed to detect elemental content in the film structure and analyze the change in the atomic percentage of the detected elements for as-deposited and annealed CdZnTe thin films. Table 4.5 presents a slight increase in the atomic percentage of Zn after annealing processes, probably due to the segregation and interdiffusion of Zn to the front surface and grain boundaries [74]. These variations are usually expected since the vapor pressures and sticking coefficients between these elements are changed. EDS results show that the surfaces of all CdZnTe thin films were Te rich which enhances the p-type conductivity, as seen in Table 4.5.

Table 4.5 EDS analysis of CdZnTe films for different annealing temperatures.

Annealing Temperature	Cd (at. %)	Te (at. %)	Zn (at. %)	x Zn/(Zn+Cd)
As deposited	43.08	55.26	1.65	0.04
100 °C annealing	42.26	55.84	1.90	0.04
200 °C annealing	43.07	54.83	2.10	0.05
300 °C annealing	43.47	54.61	1.92	0.04

The morphological characterizations of annealed CdZnTe films were investigated by SEM and AFM analysis, revealing that all films had relatively small grains and insignificant grain growth after annealing. This result suggests that only recrystallization occurred during the annealing process without changing the composition, which was also confirmed by XRD and EDS analysis. However, the surface of the film deteriorated after 300 °C and some voids appeared, indicating a sublimation from the surface of the film. Although the melting point of CdZnTe was significantly higher than the annealing temperatures, the presence of oxides drastically lowered the melting point of the mixture of CdZnTe and oxides, which were densely present on the surface of the film [61].
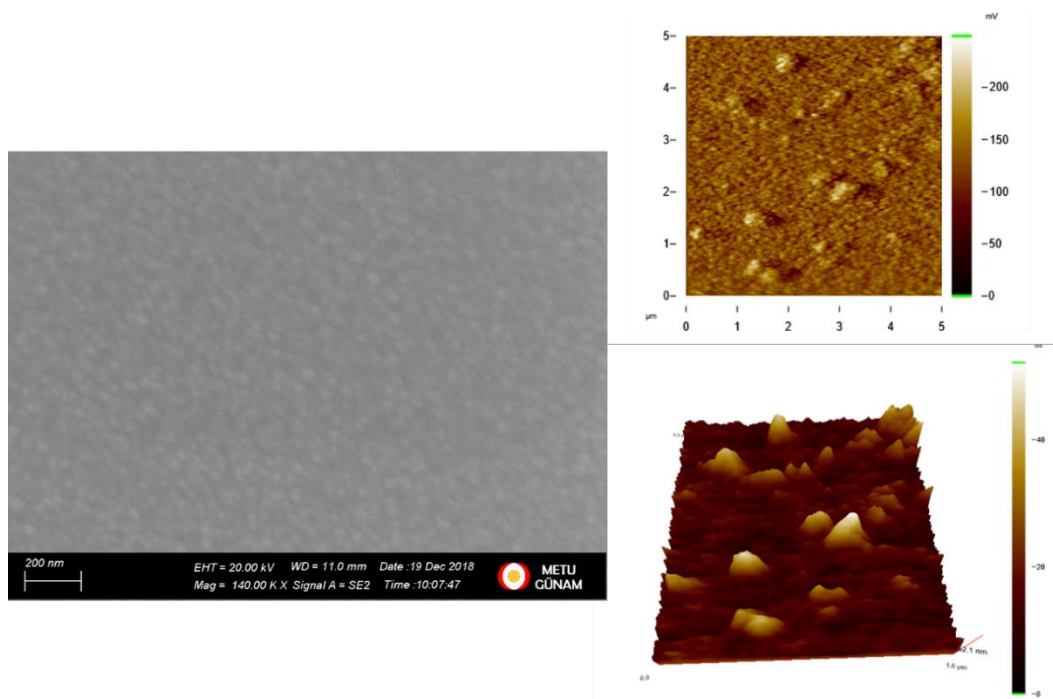
Figure 4.12. SEM and AFM images of as-deposited CdZnTe thin film.
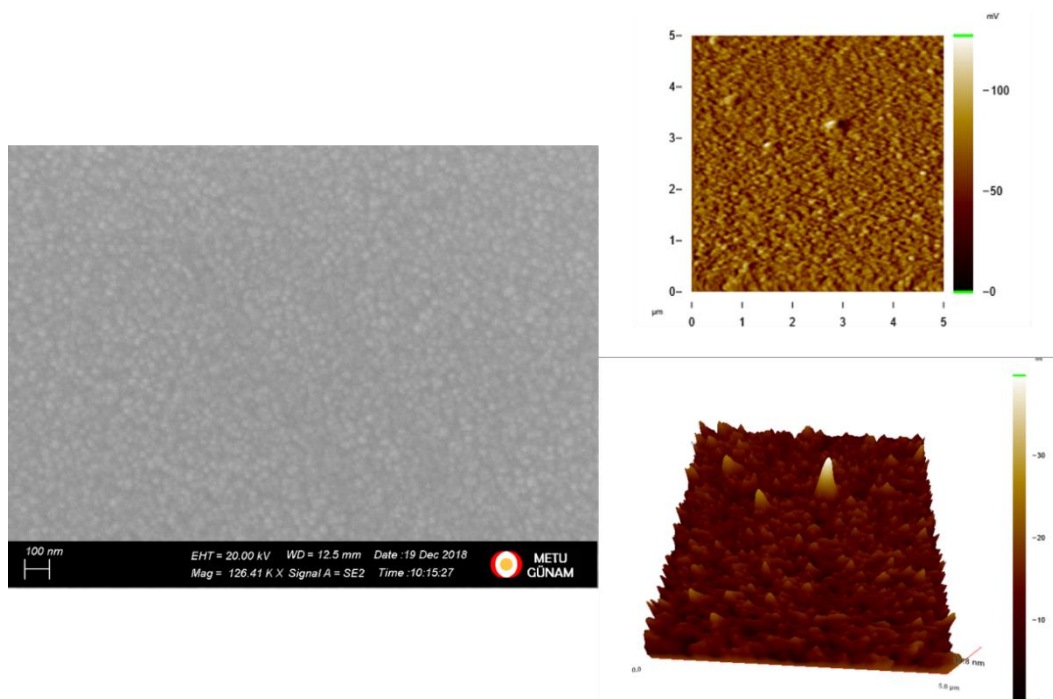
Figure 4.13. SEM and AFM images of CdZnTe thin film annealed at 100 °C.
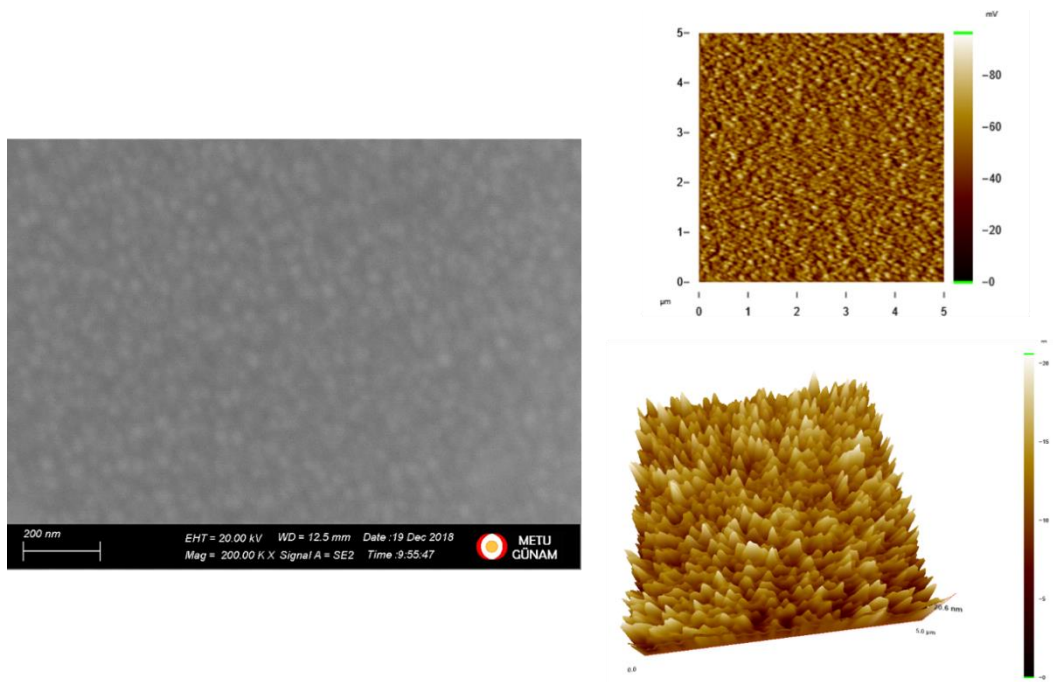
Figure 4.14. SEM and AFM images of CdZnTe thin film annealed at 200 °C.
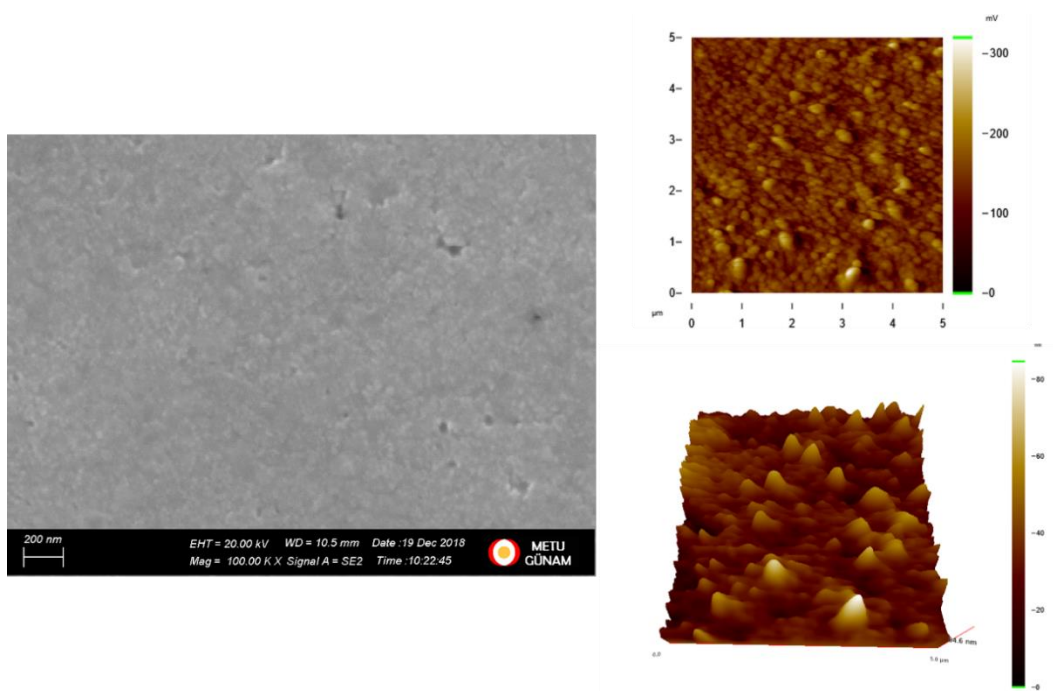
Figure 4.15. SEM and AFM images of CdZnTe thin film annealed at 300 °C.

Optical characteristics of as-deposited and annealed CdZnTe thin films were examined using transmittance measurements. The bandgap energies and absorption coefficients were calculated utilizing the transmittance spectrum. Figure 4.16 reveals the change in the transmittance behavior of CdZnTe thin films with the annealing process. A significant decrease was detected in the transmission spectra as the annealing temperature increased, attributed to the improved crystalline quality of the CdZnTe films, confirmed by XRD analysis. Another reason for the decrease in the transmission probably resulted from the formation of Te-rich surfaces with an annealing process, verified by Raman analysis. It is also possible that an increase in Zn concentration can trigger a decrease in film transmittance [90]. The bandgap energies were obtained by extrapolating the Tauc plot for zero absorption, illustrated in Figure 4.17. The bandgap energy sharply decreases after annealing at 300 °C temperature, which may be attributed to the change in the composition, the decrease in strain, and a great interaction of substrate and film [91].
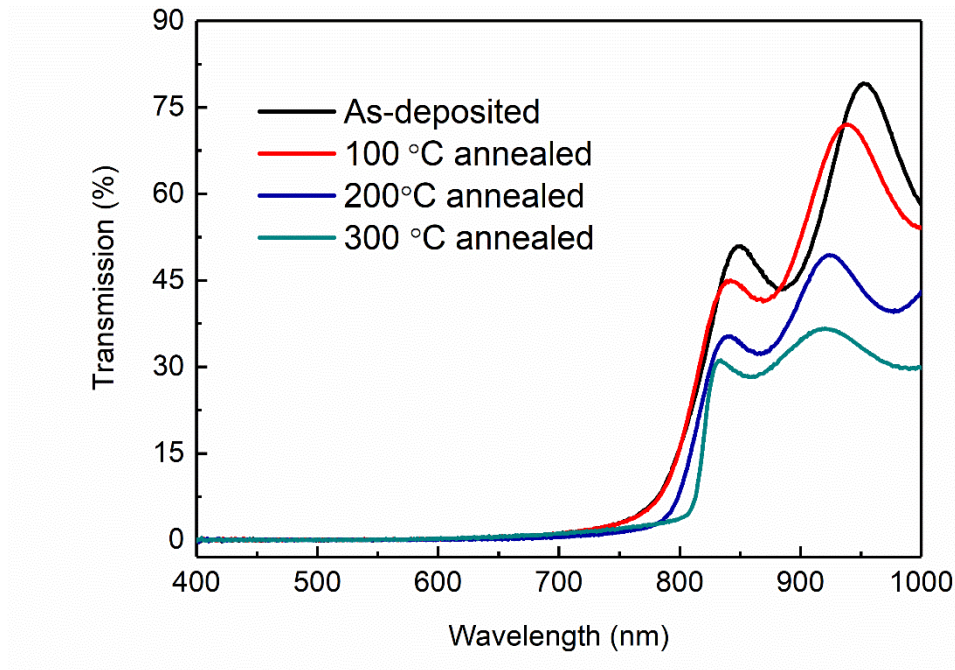
Figure 4.16. Transmittance spectra of as-deposited and annealed CdZnTe thin films.
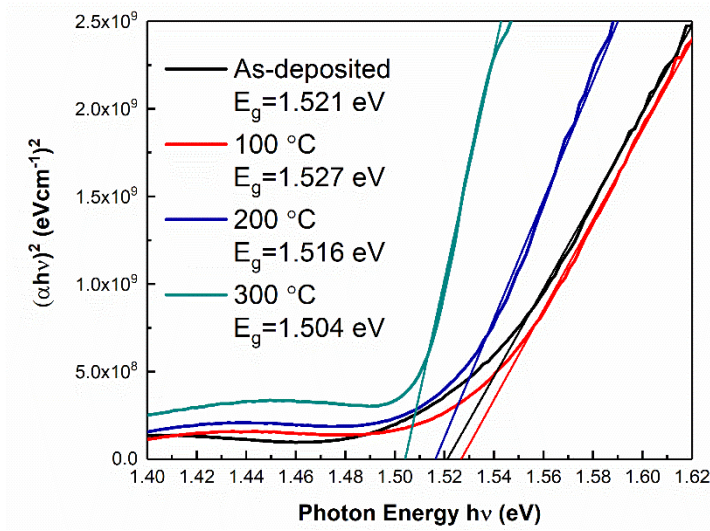
Figure 4.17. $(\alpha h\nu)^2$ vs. $h\nu$ plot of as-deposited and annealed CdZnTe thin films.

4.3.4   Cadmium Chloride Treatment

Cadmium chloride ($CdCl_2$) treatment is a critical step applied to enhance device performance and passivate the surface of the CdZnTe thin film. $CdCl_2$ treatments followed by the post-annealing process under both nitrogen and air ambient were performed to initiate the recrystallization and grain growth of CdZnTe thin films and reduce the interface defects [92], [93]. Additionally, $CdCl_2$ treatment enhanced the p-type conductivity of CdZnTe film. In this study, as-deposited CdZnTe thin film with relatively poor crystalline quality was chosen as a reference sample to better compare the enhancement in the structural, morphological, and optical properties with $CdCl_2$ treatment followed by the post-annealing process under both nitrogen and air ambient. Structural analysis of as-deposited, annealed, and $CdCl_2$ passivated CdZnTe thin films was conducted using XRD analysis. As shown in Figure 4.18 (a), all CdZnTe films had polycrystalline cubic zinc-blende structures. As-deposited and N_2 and air annealed CdZnTe films have diffraction peaks at angular positions of ~24.1°, ~39.8°, ~46.7°, ~62.8°, ~71.7°, and ~76.7° corresponding to cubic CdZnTe (111), (220), (311), (331), (422), and (333) orientations, respectively. After annealing processes, additional peaks appear at ~27.7°, and ~38.5°, ~57.0°

67

corresponding to CdTeO$_3$ and/or TeO$_2$ secondary phases [36], [77]. These Te-oxide and CdTeO$_3$ peaks reveal the deterioration of the surface by diffusion of oxygen into the CdZnTe material after the annealing processes. After CdCl$_2$ treatment followed by N$_2$ annealing, these oxide-related peaks disappeared. Additionally, a ZnO peak with a very small intensity was observed at ~67.8° after the annealing process under air ambient, probably due to the high affinity of Zn to O$_2$ [36]. The changes in the intensities of (111) and (220) diffraction planes after CdCl$_2$ treatments were also given in Figures 4.19 (a) and (b). The intensity of (111) diffraction peak increased noticeably after CdCl$_2$ treatment followed by annealing in N$_2$ ambient, attributed to the improvement in crystallinity. However, preferential (111) orientation was lost after CdCl$_2$ treatment followed by annealing in air ambient, and the intensity of the (220) plane orientation was significantly increased. The increase in random orientations could be an indication of phase and stoichiometry changes after annealing in air ambient.
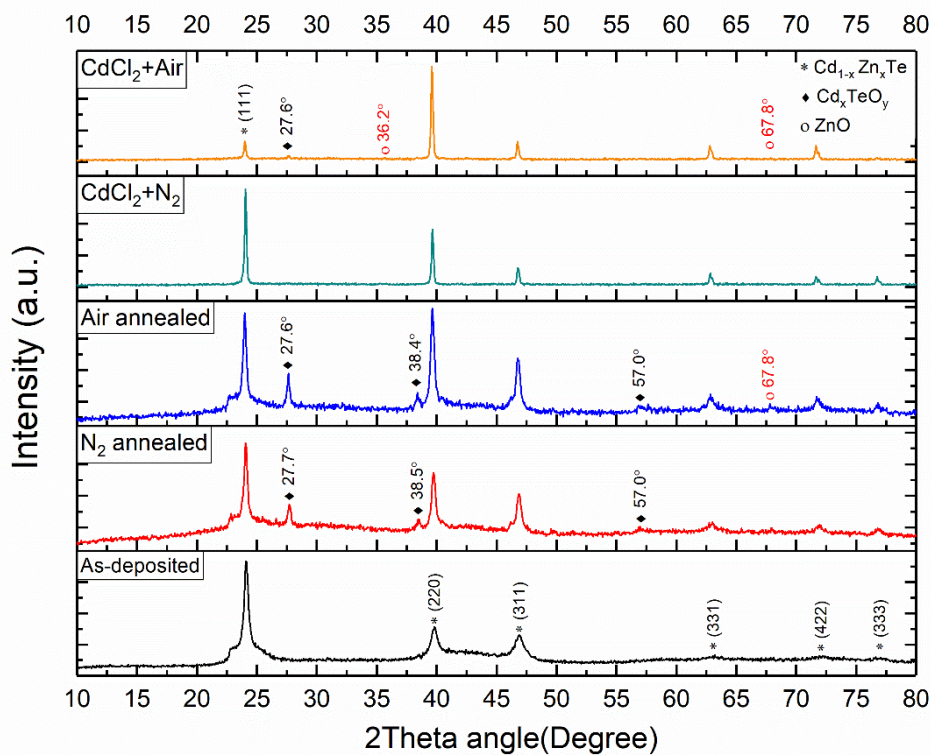
Figure 4.18. XRD patterns of CdZnTe thin films after annealing in N$_2$ and air atmosphere and CdCl$_2$ treatment.
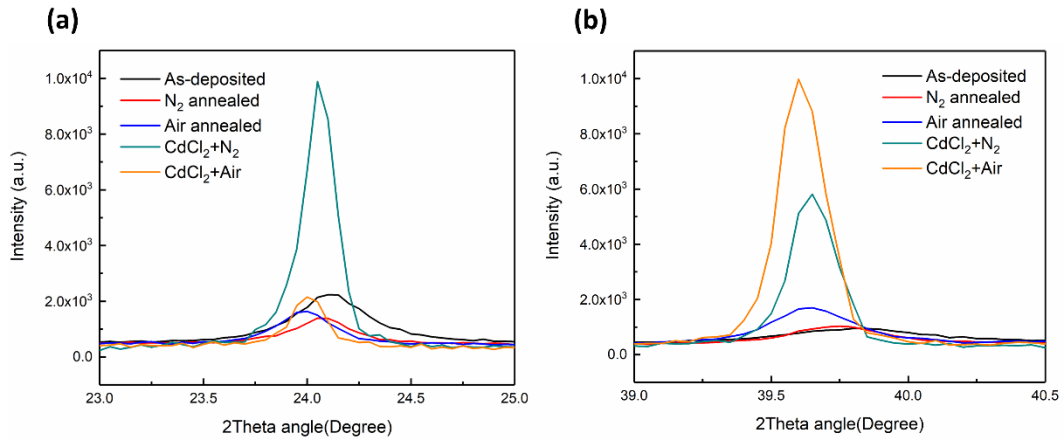
Figure 4.19. (a) The change in the intensity of (111) orientation and (b) The variation in the intensity of (220) orientation.

Significant changes in the lattice constants, average crystalline size, and dislocation densities after $CdCl_2$ treatment and annealing in N_2 and air ambient were tabulated in Table 4.6. First, the (111) planes shifted to a lower diffraction angle suggesting a compositional change in CdZnTe film structure after annealing and $CdCl_2$ treatment. Correspondingly, the lattice parameter of as-deposited CdZnTe thin film increased with annealing and $CdCl_2$ treatment. A significant decrease in the FWHM was detected with $CdCl_2$ treatment, indicating a high degree of improvement in crystalline quality and reduced lattice imperfections. The dislocation density and micro-strain noticeably decreased with $CdCl_2$ treatment due to the lattice strain relaxation, crystallinity improvement, and grain size increase. The average crystalline size rose remarkably from 14.6 to 56.9 nm after $CdCl_2$ treatment. The as-deposited film with small grains had a large crystalline formation after $CdCl_2$ treatments. Therefore, it can be deduced that $CdCl_2$ treatments followed by N_2 and air annealing processes assist dramatic grain growth by reorienting and merging small grains [61]. Additionally, the annealing of CdZnTe thin films under both N_2 and air ambient had almost similar structural properties.

69

Table 4.6 Structural parameters of as-deposited, N_2 and air annealed, and $CdCl_2$ treated CdZnTe films.

Parameters	As-dep.	N_2 ann.	Air ann.	$CdCl_2+N_2$	$CdCl_2+Air$
(111) peak degree (°)	24.1	24.0	23.9	24.1	24.0
d-value (Å)	3.69	3.70	3.71	3.70	3.70
Lattice constant (Å)	6.39	6.41	6.43	6.40	6.41
FWHM (°)	0.58	0.37	0.31	0.15	0.15
Crystalline size (nm)	14.6	22.9	27.2	55.4	56.9
Dislocation density δ ($\times 10^{10}\ cm^{-2}$)	46.8	19.0	13.6	3.3	3.1
Micro-strain ε ($\times 10^{-3}$)	11.9	7.6	6.4	3.1	3.1

Figure 4.20 illustrates Raman analysis used to analyze the variation in the vibrational modes in the CdZnTe structure for annealing in N_2 and air atmosphere and $CdCl_2$ treatment. As-deposited CdZnTe thin film had one broad peak located at ~170 cm^{-1}, associated with the CdTe-like LO_1 phonon. After annealing processes, two intense peaks appeared at ~130 and ~150 cm^{-1}, related to the A1 mode of Tellurium and the CdTe-like TO_1 phonon, respectively. The intensity of the A1 mode of Tellurium peak after air annealing was more intense than the peak that appeared after annealing in the N_2 atmosphere. After $CdCl_2$ treatment, additional peaks with much lower intensities were obtained at ~150, ~180, and ~230 cm^{-1} associated with CdTe-like TO_1 phonon, CdTe-like LO_1 phonon, and ZnTe-like LO_2 phonon, respectively. Raman spectra also have revealed second-order phonons such as CdTe-like $2TO_1$ and ZnTe-like $2LO_2$ resonant overtones after $CdCl_2$ treatment and annealing in both N_2 and air atmosphere. The variation in the phases after $CdCl_2$ treatment can be further confirmed by Raman analysis.

70
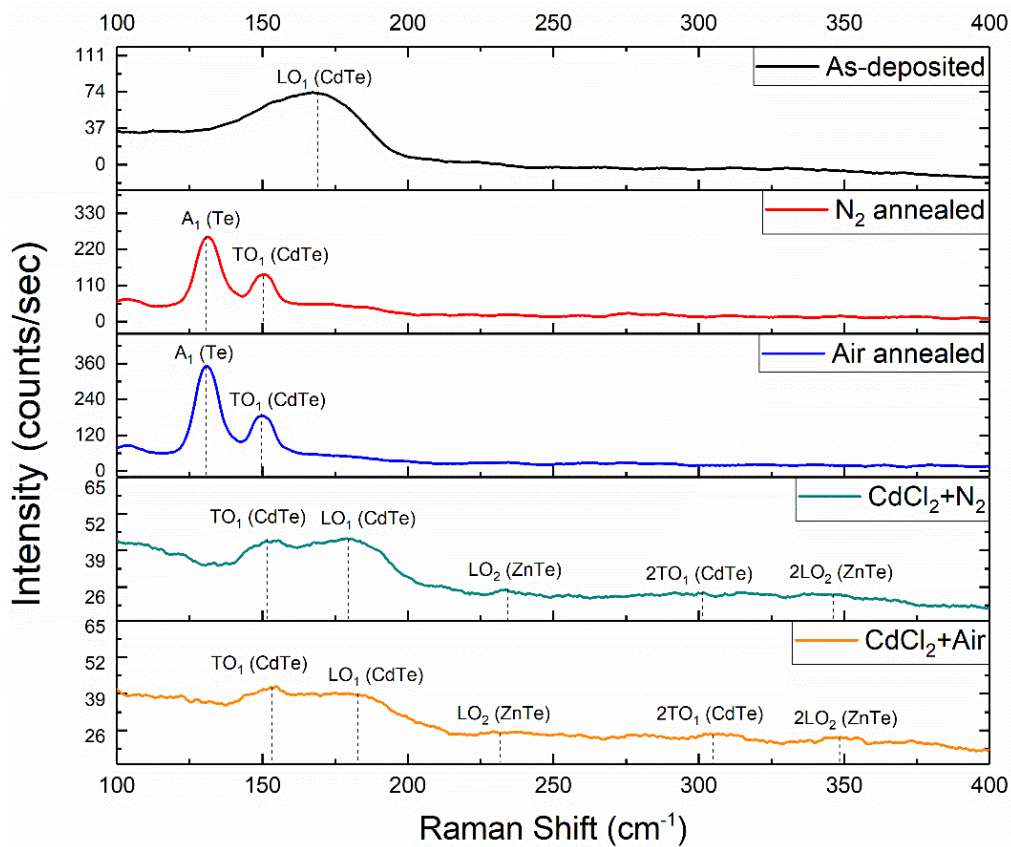
Figure 4.20. Raman spectra of CdZnTe thin film after CdCl$_2$ treatment.

EDS analysis was used to identify the variation in the elemental content of the as-deposited CdZnTe thin film with CdCl$_2$ treatment. As tabulated in Table 4.7, the atomic percentage of Zn and Cd increased with CdCl$_2$ treatment while Te concentration decreased. Cd atoms were most probably diffused from the CdCl$_2$ solution into the film structure, increasing the Cd concentrations [74], while excess Tellurium was resolved into the solution after CdCl$_2$ treatment, and a stoichiometric surface was obtained. Te precipitates were entirely converted into CdTe by providing excess Cd on the surface after CdCl$_2$ treatment [94]. After CdCl$_2$ treatment, an increase in the atomic percentage of Zn indicates interdiffusion of Zn toward the front surface of the sample. Therefore, the reduction of Te due to the resolving of precipitates and the increase in Cd because of the diffusion from CdCl$_2$ in EDS analysis could be explained by the improvement of the stoichiometry with CdCl$_2$ treatment.

Table 4.7 EDS analysis of as-deposited, N_2 and air annealed and $CdCl_2$ treated CdZnTe films.

Samples	Cd (at. %)	Te (at. %)	Zn (at. %)	x Zn/(Zn+Cd)	Te/Cd
As-deposited	42.10	52.77	5.13	0.11	1.25
N_2 annealed	41.84	52.64	5.53	0.12	1.26
Air annealed	42.38	53.00	4.62	0.09	1.25
$CdCl_2$ treatment+N_2	45.26	46.92	7.83	0.15	1.04
$CdCl_2$ treatment+Air	44.04	49.80	6.16	0.12	1.13

The change in the morphology of the as-deposited CdZnTe thin film with $CdCl_2$ treatment was investigated using SEM analysis which illustrates similar surface morphologies for as-deposited, N_2 annealed, and air annealed CdZnTe thin films with smooth, densely packed small grains and free of pinholes. After $CdCl_2$ treatment followed by annealing under N_2 and air ambient, the surface morphology of the films significantly changes. After $CdCl_2$ treatment, a significant increase in grain size was observed. CdZnTe re-crystallized so that some small grains merged into bigger grains and reoriented themselves, introducing an entirely different microstructure, also verified by XRD results. However, a large number of cracks also appeared at the surface with $CdCl_2$ treatment.

The formation of cracks and holes at the interface can be attributed to the decomposition of CdZnTe after interaction with $CdCl_2$, the evaporation of Cd and Te, and the out-diffusion of Zn [61]. Although the complex reaction between CdZnTe-$CdCl_2$-$CdTeO_3$ promotes a high degree of recrystallization and grain growth, the melting mixture of these materials on the surface with lowered melting point and elevated vapor pressure results in hole formation [59]. After $CdCl_2$ treatment followed by annealing, when this liquid mixture was cooled down gradually to room temperature, cracking was introduced on the surface of the films.
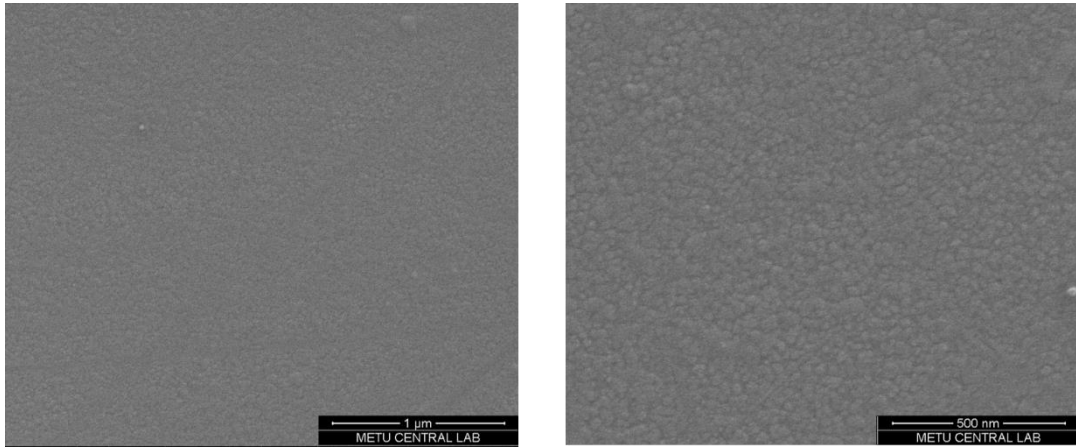
Figure 4.21. SEM images of as-deposited CdZnTe thin film.
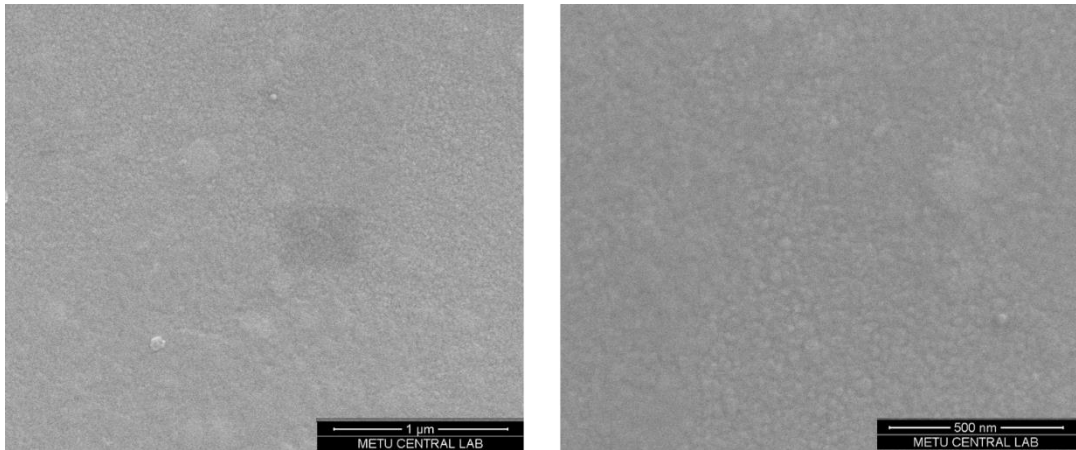
Figure 4.22. SEM images of N$_2$ annealed CdZnTe thin film.
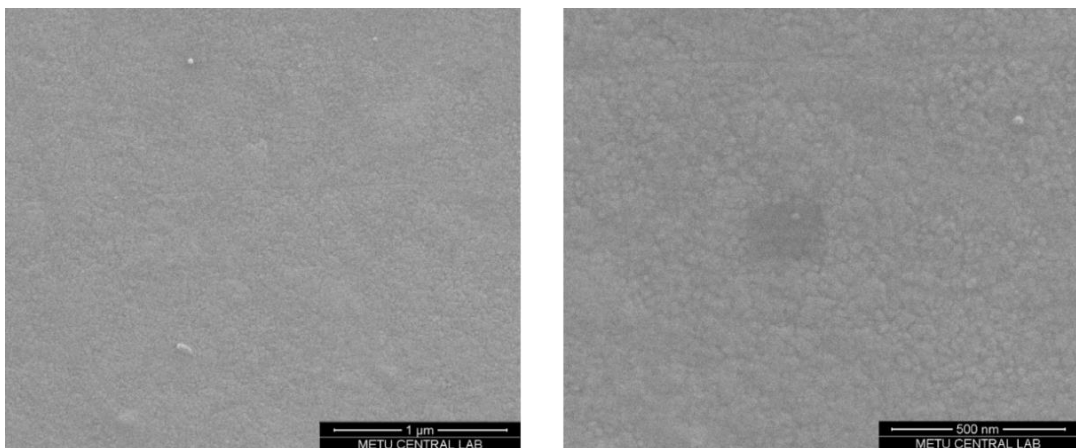
Figure 4.23. SEM images of air annealed CdZnTe thin film.
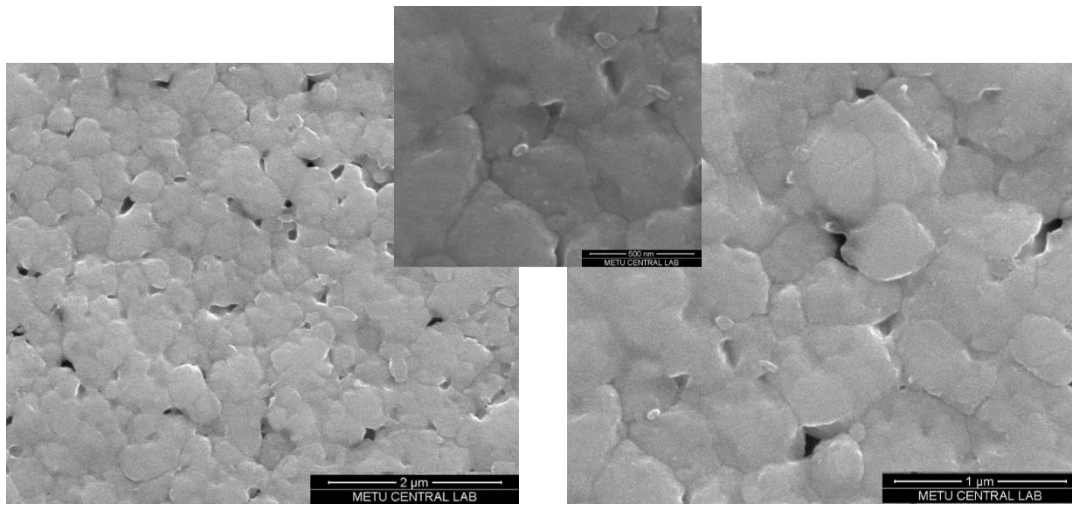
Figure 4.24. SEM images of CdZnTe thin film after $CdCl_2$ treatment followed by N_2 annealing.
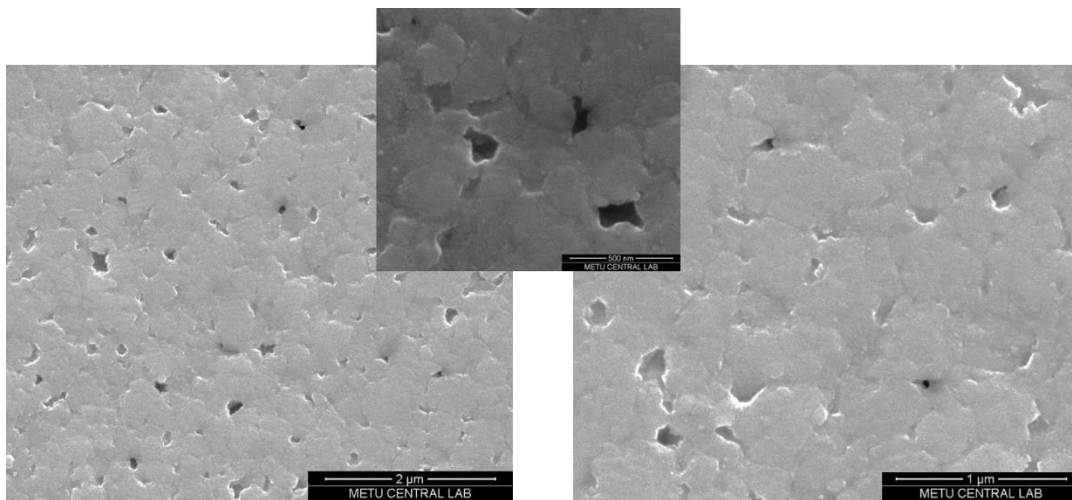
Figure 4.25. SEM images of CdZnTe thin film after $CdCl_2$ treatment followed by air annealing.

Optical transmittance was maximum for $CdCl_2$ treatment and subsequent N_2 annealing, as shown in figure 4.26 (a). Absorption of crystalline defects occurs at a longer wavelength reducing transmittance spectra. Therefore, higher transmittance values indicated lower defect density for $CdCl_2$ treatment and subsequent N_2 annealing. However, with $CdCl_2$ treatment and subsequent air annealing, the transmission of CdZnTe film decreased drastically, while the change in the bandgap

was almost insignificant. Transmission measurement indicated a bandgap shift after annealing processes under both N_2 and air ambient. However, when $CdCl_2$ was introduced and the annealing process was performed, the bandgap shifted in the opposite direction. Figure 4.26 (b) indicates a slight increase in bandgap energy with $CdCl_2$ treatment, which could be ascribed to the diffusion of Cl into the grain boundaries.
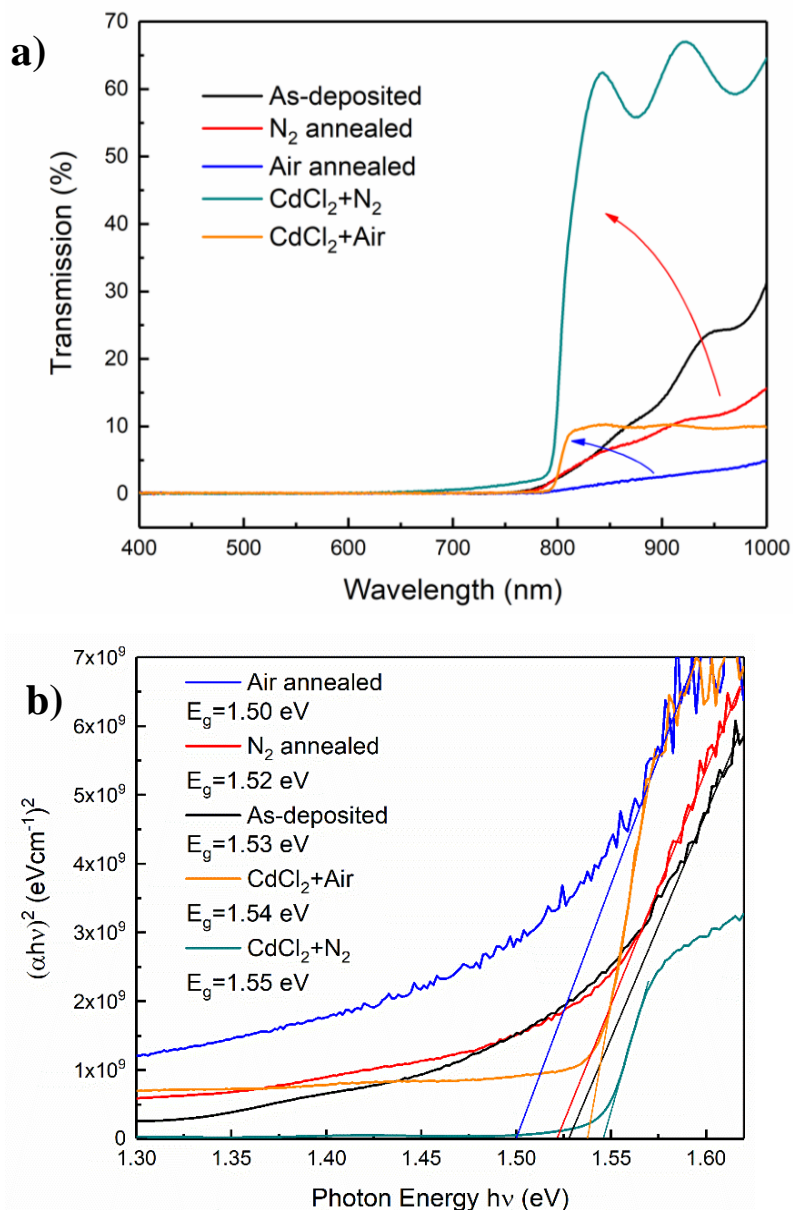
Figure 4.26. (a) Transmission spectra and (b) $(\alpha h\nu)^2$ vs. $h\nu$ plot of as-deposited CdZnTe thin film after annealing in N_2 and air atmosphere and $CdCl_2$ treatment.

Finally, electrical transport properties were investigated after annealing and CdCl$_2$ treatment. The parameters such as conduction type, carrier concentration, electrical conductivity and resistivity were acquired using the Hall effect system. Determination of the conduction type is critical since the type of the absorber layer is a critical parameter for back contact formation. Au metal on the p-type CdZnTe layer produces low-resistive ohmic contacts, while the back-metal contact formation on the n-type CdZnTe layer is more complicated with a high-resistive layer. Therefore, the electrical conduction type of the CdZnTe layer is essentially required for a low resistive back-contact formation. CdZnTe films can result with either p- or n-type according to the material composition changes during growth. The composition can shift from Te-rich to Cd-rich or vice versa, forming related defect structures [95]. CdCl$_2$ treatment followed by an annealing process can radically change defect structure. After deposition of CdZnTe material, it has been reported that both n $\rightarrow$ p and p $\rightarrow$ n transitions are likely [96].

As can be seen from Table 4.8, as-deposited CdZnTe thin film was n-type with a high resistivity of $1.1\text{x}10^4 \ \Omega cm$ and an electron concentration of $1.6\text{x}10^{12} \ cm^{-3}$ at room temperature. Electron Hall mobility was 346.1 $cm^2 Vs$ before annealing and 367.8 $cm^2 Vs$ after annealing, indicating better carrier transport characteristics. However, carrier concentration values for all CdZnTe thin films were significantly low. The low carrier concentration and high resistivity values are the two main factors limiting the efficiency of the solar cell. After annealing at 200 °C for 30 minutes in an N$_2$ atmosphere, a slight decrease in resistivity was observed, but conversion in the type was not noticed. After CdCl$_2$ treatment followed by an annealing process, n-type CdZnTe thin film becomes p-type with relatively lower resistivity and a high hole concentration of $3.5\text{x}10^{13} \ cm^{-3}$. It can be concluded that electrons were predominant (n-type) for as-deposited and annealed CdZnTe thin films, while holes were dominant (p-type) for CdZnTe films after CdCl$_2$ treatment. These results agree with other studies [12], [95]–[97].

Table 4.8 Variation in the electrical transport properties of CdZnTe thin films after annealing process and CdCl$_2$ treatment.

Sample	As-deposited CdZnTe	Annealed CdZnTe	CdCl$_2$ treated CdZnTe
Resistivity $[ohm \cdot cm]$	$1.1x10^4$	$5.0x10^3$	$2.1x10^3$
Conductivity $[1/ohm \cdot cm]$	$9.1x10^{-5}$	$2.0x10^{-4}$	$4.8x10^{-4}$
Carrier Concentration N_H (cm^{-3})	$1.6x10^{12}$	$3.3x10^{12}$	$3.5x10^{13}$
Mobility $[cm^2(V \cdot s)]$	346.1	367.8	85.4
Type	n-type	n-type	p-type

CHAPTER 5

SURFACE CHEMICAL COMPOSITIONAL ANALYSIS AND OPTICAL DIELECTRIC RESPONSE OF CdZnTe THIN FILMS

The surface and interface of CdZnTe thin films are critical properties in characterizing device performance by accurate prediction of the quality of the film. In this study, surface chemical composition and optical dielectric properties of thermally evaporated CdZnTe thin films were investigated. Material characterization of CdZnTe thin films was obtained using X-ray photoelectron spectroscopy (XPS) analysis. XPS analysis was utilized to evaluate native oxide formation on the surface and in bulk, investigate chemical states at the interface, and explore the depth profile of atomic compositions and stoichiometry of the CdZnTe thin films as a function of annealing parameters. Optical characterization was achieved using variable angle spectroscopic ellipsometry (VASE) analysis, a highly surface-sensitive technique. VASE analysis was employed using the Adachi 3D M0 model to determine dielectric functions from 1.23 to 3.49 eV and describe the dielectric response of the CdZnTe thin films. Measured dielectric spectra illustrated distinctive structures at energies corresponding to the interband transitions. The effect of annealing on optical constants, including refractive index, extinction coefficient, absorption coefficient, and normal incidence reflectivity, were also investigated.

5.1   Introduction

Understanding the surface chemical composition and optical features of CdZnTe is vital for the interpretation and enhancement of device performance. XPS analysis is widely used to analyze near-surface or interface and bulk chemical properties of a semiconductor device for a broad range of purposes [98]. XPS analysis is employed to evaluate the dynamics of native oxide formation on the surface of the film, which could deteriorate the performance of the device significantly. The knowledge of these dynamics may assist in understanding the formation of surface oxides, which is necessary for developing proper surface treatments and ensuring long-time stability.

Additionally, the compositional variation with respect to depth analysis from the surface into bulk can also be determined. Variation in the composition and microstructure of the surface/interface also influences dielectric function [99]. Therefore, the optical dielectric response of CdZnTe thin films and optical properties of native oxide on CdZnTe can be determined using ellipsometry. Spectroscopic ellipsometry is an excellent characterization tool to extract thickness, refractive index, and extinction coefficient. Knowledge of the dielectric functions, $\varepsilon = \varepsilon_1 + i\varepsilon_2$, and refractive index, $N = n + ik = [\varepsilon]^{1/2}$, is crucial to utilize and improve solar cell device properties and understand the electronic structure of the material. Ellipsometric measurements allow us to calculate the absorption coefficient and reflectivity at normal incidence for a specific wavelength range [29],[100].

5.2   Experimental Details

Thin CdZnTe films (120 nm) were deposited on glass and Si substrates by thermal evaporation under high vacuum pressure. As-deposited films were annealed at 150 and 300 °C in a furnace for 30 min under a Nitrogen atmosphere. Afterward, the variation of surface properties of CdZnTe thin films after the annealing process was studied. Material characterization was conducted by XPS measurement, while

optical characterization was acquired using transmission and ellipsometry measurements. VASE analysis was performed by SOPRA GES-5E ellipsometer to determine the dielectric functions in 1.23-3.49 eV and describe the dielectric response of CdZnTe. The dispersion law that was employed to model the dielectric function of CdZnTe thin films was the Adachi 3D-M0 model. This model was utilized to define spectral dependence of dielectric constant for diamond and zinc-blende structure semiconductor crystals having direct bandgap properties with high symmetry as three-dimensional (3D) M0 critical points (CP`s) in the band structure. The model structure used in this study consists of Si substrate/CdZnTe thin films with a surface oxide layer in addition to the roughness of the film was presented in Figure 5.1.
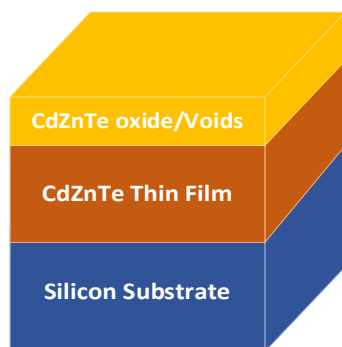
Figure 5.1. An assumption of the layer structure with surface roughness consists of Si/CdZnTe/CdZnTe oxides + roughness applied in the investigated spectral region.

5.3   Result and Discussion

5.3.1   Chemical-Compositional Analysis

XPS analysis was applied not only to examine the depth profile of atomic compositions and stoichiometry of the CdZnTe thin films according to annealing parameters but also to investigate the present chemical states at the interface and define the complex nature of oxides [101]. Obtained XPS survey spectrums CdZnTe thin films were given in Figure 5.2. The relatively high intensity of core-level peaks

obtained for as-deposited CdZnTe thin film indicated a suitably clean surface. In contrast, XPS survey spectra after annealing showed an increase in Carbon and Oxygen contamination which significantly affected the intensities of the core levels on the first layer of the films. For the 150 °C annealed sample, the intensity of Carbon and Oxygen peaks of XPS spectra suppressed the Cd 3d and Te 3d core-level peaks, and their intensities were reduced significantly. When the annealing temperature was increased to 300 °C, Cd 3d and Te 3d peak intensities became visible again. The carbon contamination of the surface after the annealing process could have resulted from the annealing environment at relatively low temperatures even though the annealing process was performed under a nitrogen atmosphere.
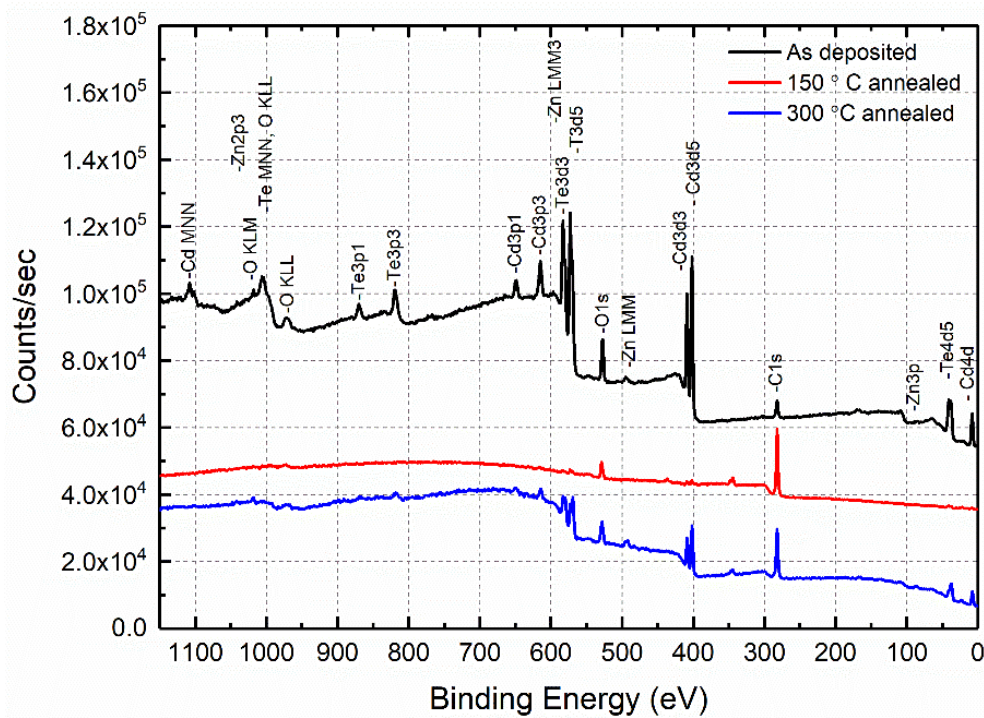
Figure 5.2. The XPS spectrum of the as-deposited and annealed CdZnTe thin films.

As mentioned above, annealing treatment significantly altered the bonding states and chemical composition at the surface. Therefore, depth profiling was carried out by sputtering the surface layer by layer to investigate subsurface regions presented in Figure 5.3. The atomic composition of subsurface regions proved the stoichiometric bulk composition. After sputtering the layers of as-deposited CdZnTe thin film, the

82

Oxygen content was eliminated immediately in the first sputtered layer, suggesting that only the upper surface was oxidized from storage conditions. When the annealing was performed, Oxygen content could not be eliminated even after the 10th sputtered layer, suggesting that the annealing process resulted in a rougher and thicker oxidized surface.
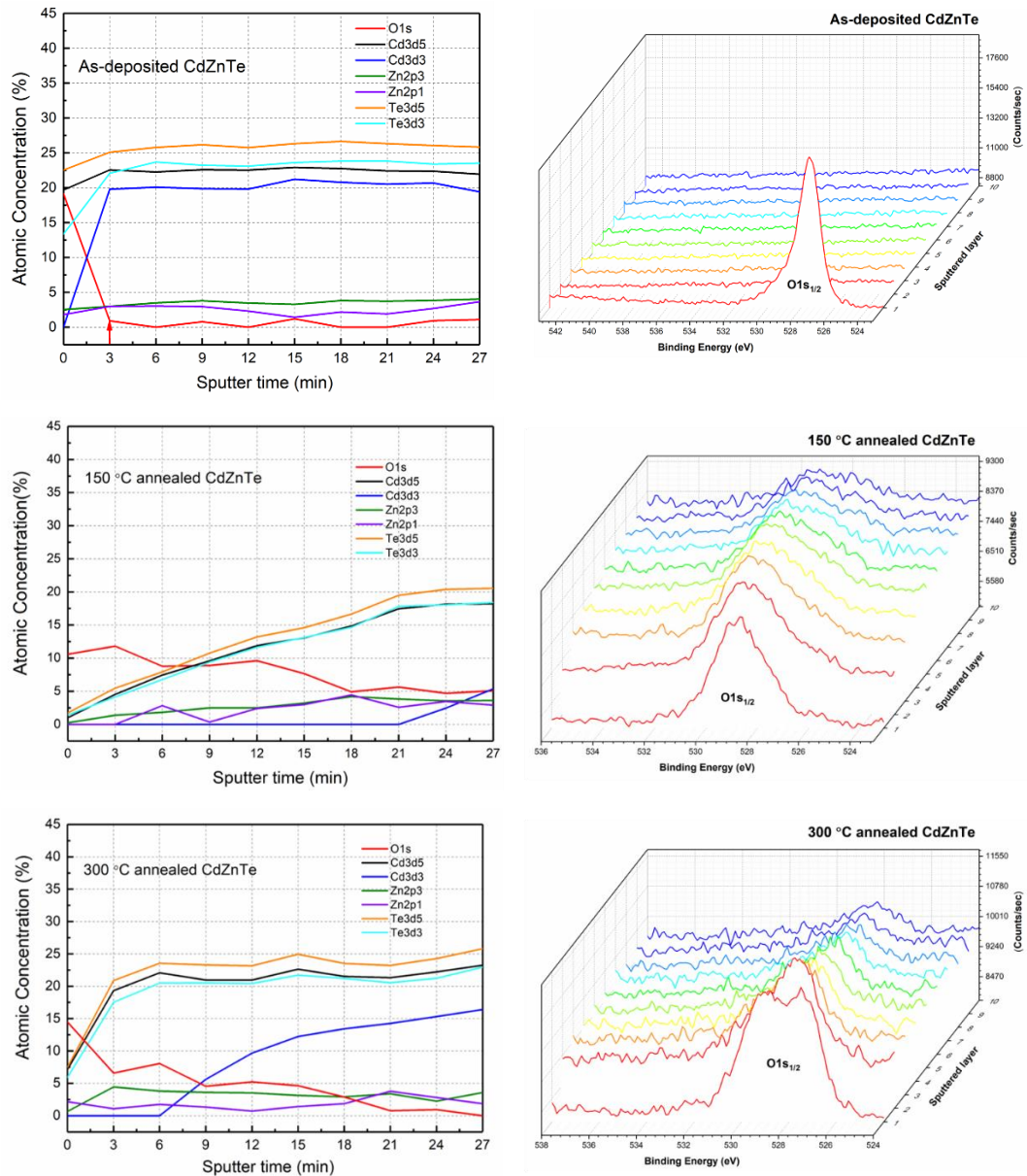
Figure 5.3. XPS depth composition analysis and corresponding Oxygen content for as-deposited, 150 °C and 300 °C annealed CdZnTe thin film surfaces.

Additionally, a detailed investigation was conducted to identify the effect of annealing temperatures on the O 1s peak of the first layer of the CdZnTe thin film. It can be observed from Figure 5.4 that the O 1s peak of the as-deposited film was asymmetrical. As the annealing temperature was increased, more asymmetrical O 1s peaks were observed between 528 and 534 eV revealing the presence of oxygen atoms with different chemical bond formations. In order to achieve oxide components, we have decomposed the peak for as-deposited and annealed samples. O1s peak was resolved into three peaks: one peak at an energy of ~530.2 eV corresponds to $TeO_2/CdTeO_3$, while the higher binding energy component located at ~531.5 eV is associated with C contamination and/or $Cd(OH)_2$. Additionally, According to Dupin et al. [102], the binding energy of ~529.2 eV is characteristic of cadmium oxide (CdO) [103] [104].
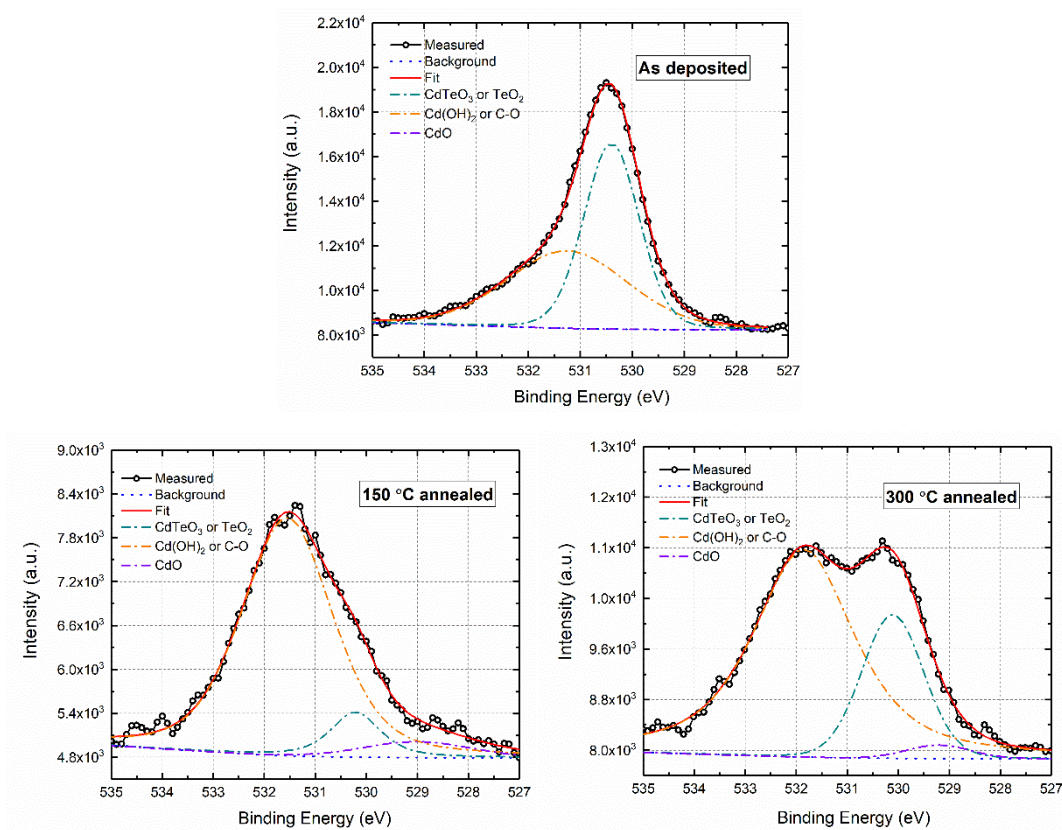
Figure 5.4. XPS core-level spectra of O 1s level for as-deposited, 150 °C and 300 °C annealed CdZnTe thin film surfaces.

84

In addition to XPS depth analysis of the Te 3d core level, a detailed examination of the peak shape of Te 3d for the first layer was examined by decomposing each photoelectron peak of the elements. XPS spectra for Te 3d were given in Figure 5.5. A doublet peak for elemental tellurium was visible at ~572.0 eV for Te $3d_{5/2}$ and ~582.5 eV for Te $3d_{3/2}$, caused by the Te-Cd bonds (Te^{-2} state). An Additional peak doublet correlated with oxygen bound to tellurium was similarly detected in Figure 5.5, associated with O-Te (Te^{+4} state) bonding states in $CdTeO_3$ or TeO_2. Hence, a change in the formation of $CdTeO_3$ or TeO_2 was verified after different annealing temperatures. It has been stated that the formation of TeO_2 triggers an energy shift of ~3.2 eV, and $CdTeO_3$ produces a ~3.5 eV energy shift [76],[105]. As-deposited sample had a chemical shift of ~3.3 eV, indicating TeO_2 formation due to the oxidation of excess Te on the surface. In comparison, annealed samples had a change of ~3.5 eV, suggesting $CdTeO_3$ formation with annealing. The energy shift observed in Te after depth profile analysis resulted from the charge transfer of Te to O atoms [18],[106].
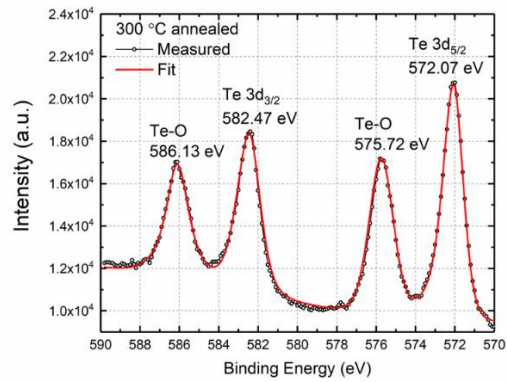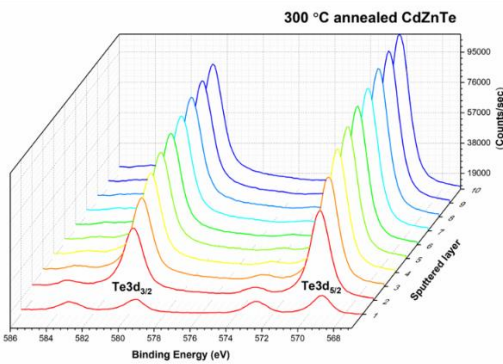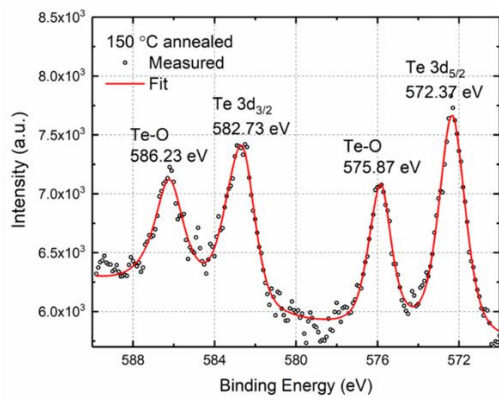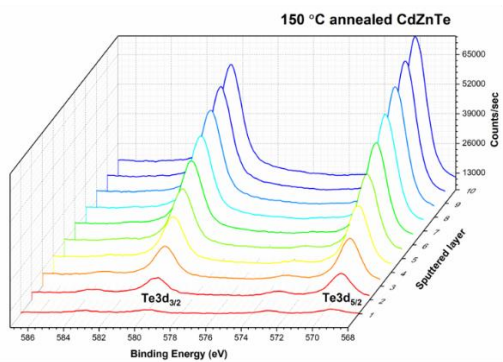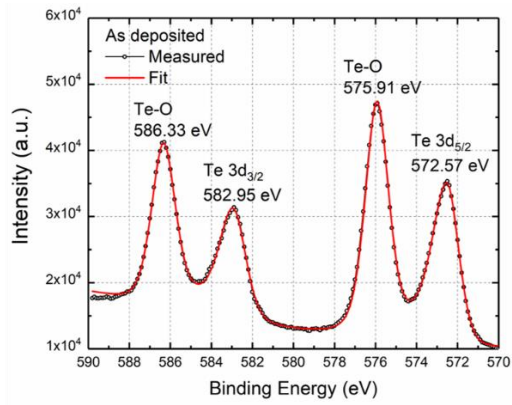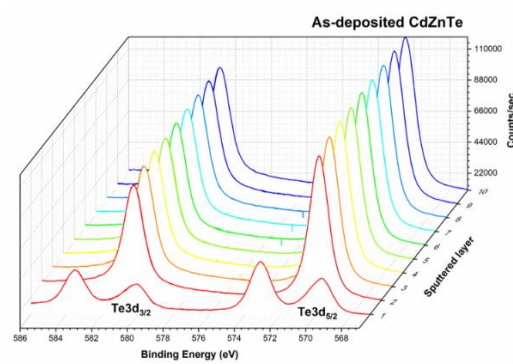
Figure 5.5. XPS depth analysis of core-level spectra of Te 3d level and fitting of the Te 3d level for the first layer of as-deposited, 150 °C and 300 °C annealed CdZnTe thin films.

Figure 5.6 illustrates Cd 3d peaks that were created by the spin-orbit coupling of Cd 3d$_{5/2}$ and Cd 3d$_{3/2}$. Examination of Cd oxides from Cd 3d is impractical because Cd oxides are entirely unclear since CdTeO$_3$, which was formed after the oxidation of Cd, has an almost similar chemical state to Cd. However, linewidth broadening was detected.
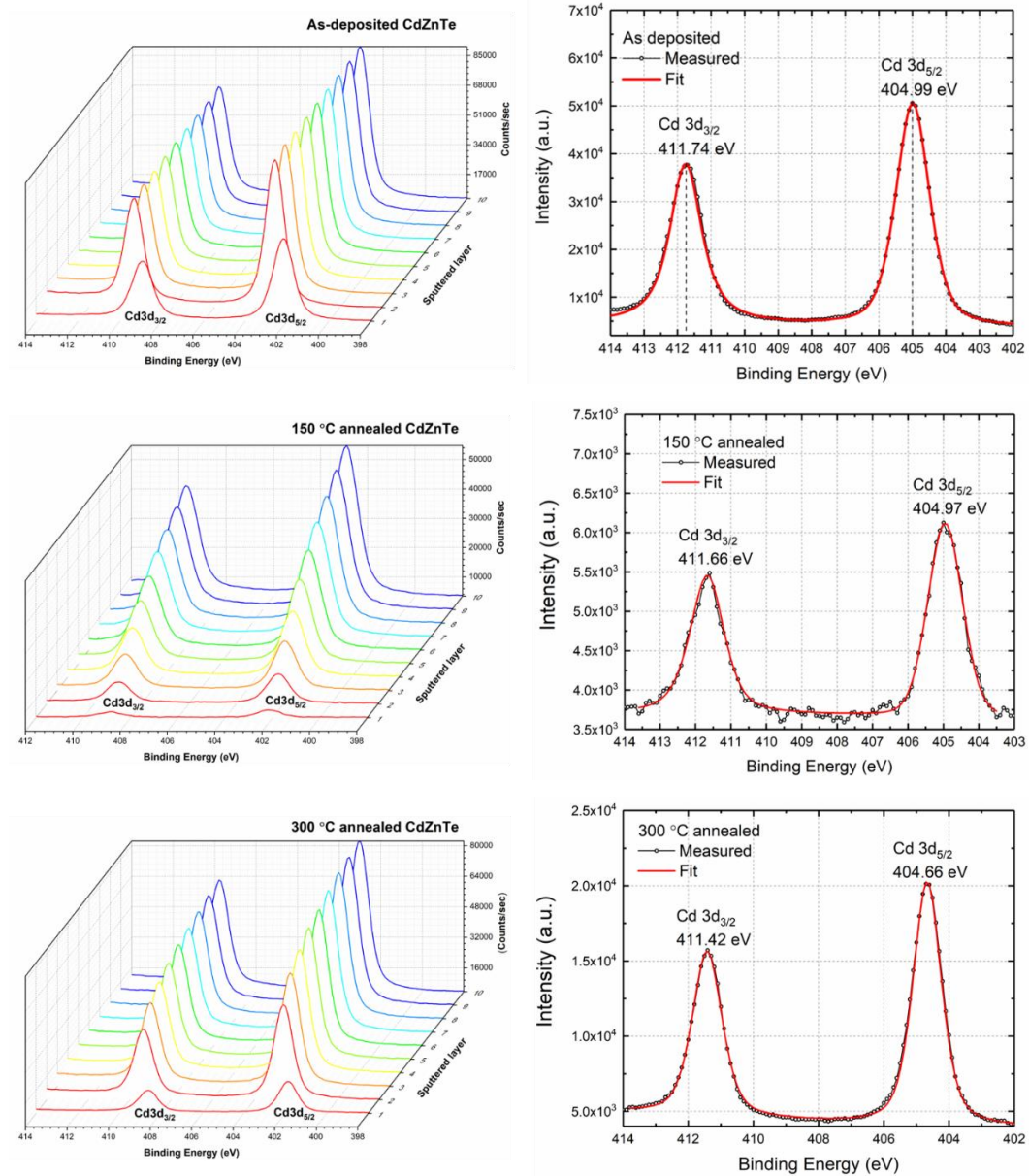
Figure 5.6. XPS core-level spectra of Cd 3d level for as-deposited, 150 °C and 300 °C annealed CdZnTe thin film surfaces.

The XPS depth analysis of the two Zn 2p peaks was given in Figure 5.7. According to the depth analysis, the surface was Zn deficit, while peak intensity was increased considerably into the bulk, implying an increased Zn ratio in the structure. Zn $2p_{3/2}$ and Zn $2p_{1/2}$ peaks with binding energies at 1018.95 and 1041.99 eV were obtained for as-deposited and 150 °C annealed CdZnTe samples. The energies were slightly shifted toward lower energies after annealing at 300 °C.
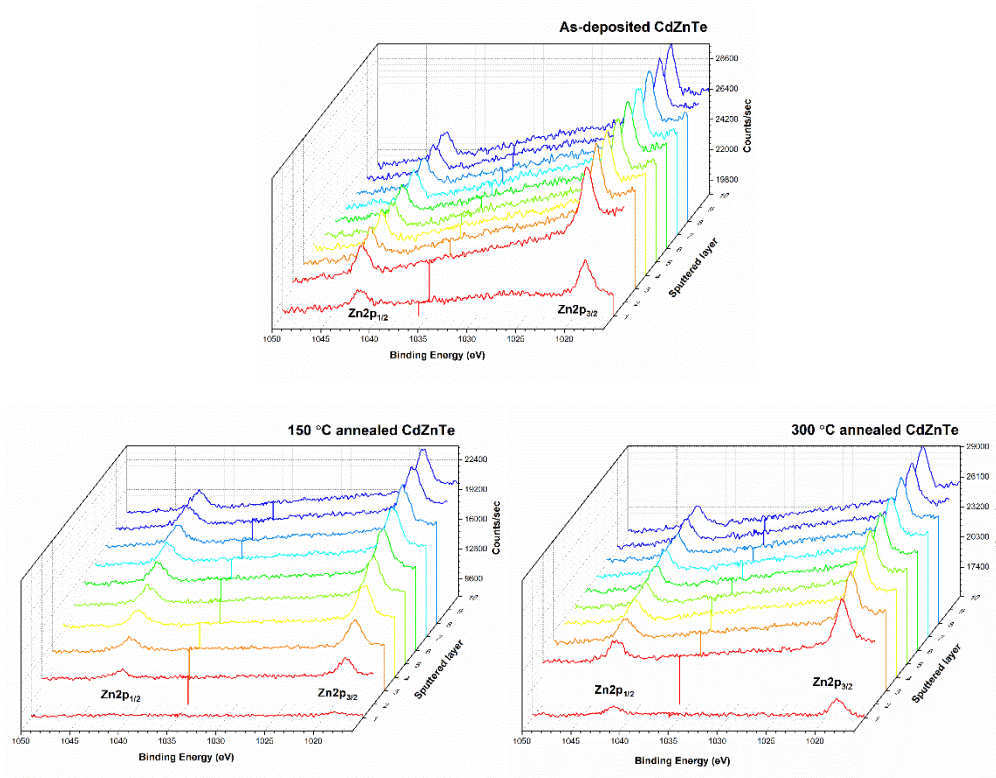
Figure 5.7. XPS core-level spectra of Zn 2p level for as-deposited, 150 °C and 300 °C annealed CdZnTe thin film surfaces.

5.3.2   Optical Dielectric Response Analysis

Variable-angle spectroscopic ellipsometry (VASE) was used to investigate the effect of annealing on the refractive index, extinction coefficient, complex dielectric functions, absorption coefficient, reflectivity, and layer thickness for CdZnTe thin films. The thickness of the as-deposited CdZnTe film obtained by ellipsometry was

~120 nm. However, after annealing at 150 and 300 °C, the film thicknesses were measured as ~116 nm and ~104 nm correspondingly. The thickness of the film was slightly reduced after the annealing process at 300 °C, probably due to the evaporation of the constituent elements in the structure. Furthermore, the thicknesses of oxides layers, including the surface roughness, were measured as ~3.3, ~3.5, and ~4.8 nm for as-deposited, 150, and 300 °C annealed CdZnTe thin film samples, respectively. The oxide thickness and the roughness of the films were observed to increase slightly at higher annealing temperatures. Figure 5.8 shows the evolution of ellipsometric parameters, $\alpha(45°)$ and $\beta(45°)$, as a function of photon energy with post-deposition thermal treatment. Significant changes in the spectra of the $\alpha(45°)$ and $\beta(45°)$ parameters were observed with annealing temperatures which were associated with the absorption of CdZnTe thin films. Variation of these parameters with the post-deposition annealing process suggested certain variations at the surface of the films.
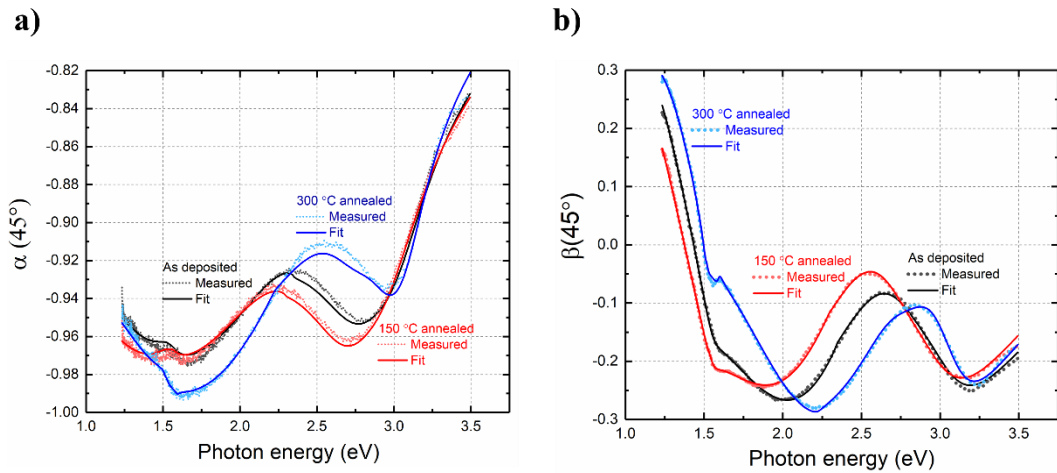
Figure 5.8. Evolution of ellipsometric parameters, (a) $\alpha(45°)$ and (b) $\beta(45°)$, for as-deposited and annealed CdZnTe thin film samples.

Variation of the spectra of real $<\varepsilon_1>$ and imaginary $<\varepsilon_2>$ components with respect to post-deposition annealing treatment was given in Figure 5.9. The measured dielectric function showed discrete structures at specific energies which correspond to inter-band transitions. According to reported Refs. [[21], [29], [107]–[109],[110]], the

position energies of these peaks in the $<\varepsilon>$ spectrum are associated with critical points (inter-band transitions). Identifying the origin of these energy-band structures, including bandgap energy and transitions concerning critical points, is crucial since they define the structure of the optical emission spectrum and reveal the effect of structural and thermal disorder on the material's electronic properties. Figure 5.9 (a) shows two clear peaks and one unclear shoulder in the $<\varepsilon_1>$ spectrum for the 300 °C annealed sample. Additionally, Figure 5.9 (b) shows one clear peak and one unclear shoulder in the $<\varepsilon_2>$ spectrum. The first clear structure originated from transitions at the E_0 edge, which gave the direct bandgap energy of the material. Accordingly, the bandgap energy of as-deposited and 150 °C annealed CdZnTe samples was ~1.54 eV, whereas the bandgap energy was reduced to ~1.52 eV for 300 °C annealed CdZnTe samples. The second structure occurred at ~2.4 eV, related to the $E_0 + \Delta_0$ critical point. The critical point at $E_0 + \Delta_0$ correlated to a week transition at k=0 due to the spin-orbit interaction. Maxima in the $<\varepsilon_2>$ spectrum at the ~3.5 eV spectral region could be attributed to the E_1 transition. The E_1 is a strong transition at point L in the Brillouin zone due to spin-orbit splitting [27].
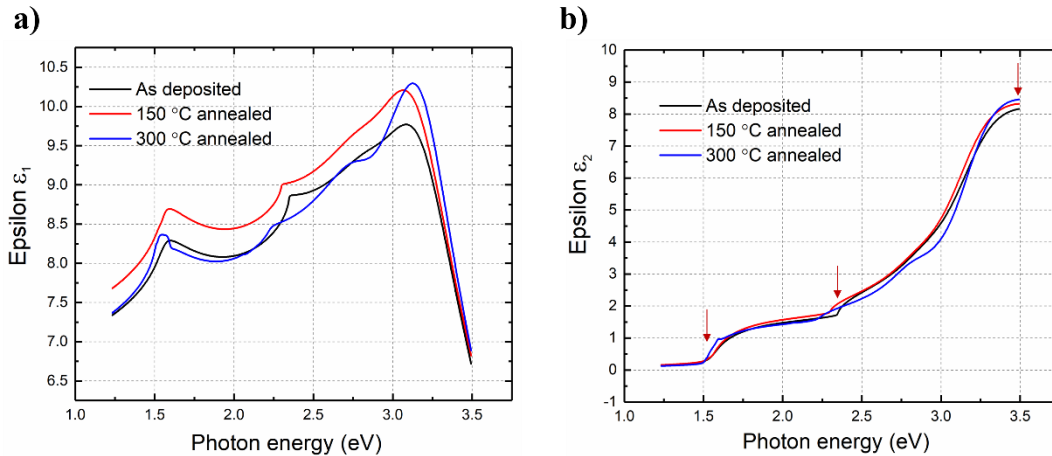
Figure 5.9. The evolution of real (ε_1) and imaginary (ε_2) components of dielectric function for as-deposited and annealed CdZnTe thin film samples.

Moreover, as presented in Figure 5.9 (b), the imaginary part of the dielectric function does not reach zero value below the absorption edge. The theoretical expectations indicate that ε_2 must be zero in the $hv < E_g$ region. The nonzero ε_2 behavior in the

below absorption edge could be explained considering the intrinsic contributions and stoichiometric deviations [1].

Refractive index and extinction coefficient spectra, given in Figure 5.10, also reveal the distinct critical point structures related to the inter-band transitions. The refractive index was significantly changed after the annealing process at 300 °C, indicating a phase change and Zn evaporation. The most substantial peak in n(E) was related mainly to the E_1 transitions. The E_0 transitions were also found to provide a weak peak in the n(E) dispersion [29]. The small glitch for the 300 °C annealed sample at 1.5 eV was not physical, and it is related to the model that has been used to fit the measured data.

a)   b)
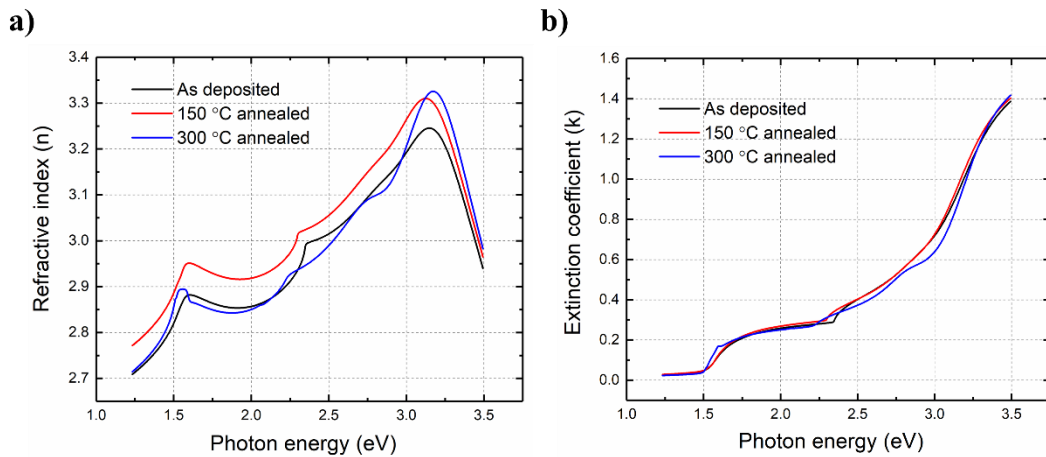
Figure 5.10. The variation of refractive index and extinction coefficient of CdZnTe thin films.

Absorption coefficient α (cm^{-1}) and normal incidence reflectivity R (using Eqn. 2.8 and Eqn. 2.9) with respect to post-annealing treatment were calculated. Figure 5.11 (a) reveals that at shorter wavelengths (higher energies), the absorption coefficient increases for all CdZnTe thin films, and the calculated absorption coefficient value is around 10^5 cm^{-1} in the 2.5-3.5 eV. The bandgap energy was slightly decreased as the annealing temperature increased, shifting the fundamental absorption edge to a longer wavelength [1]. The reflectivity R(E) spectra have also revealed the distinct critical point structures in Figure 5.11 (b).
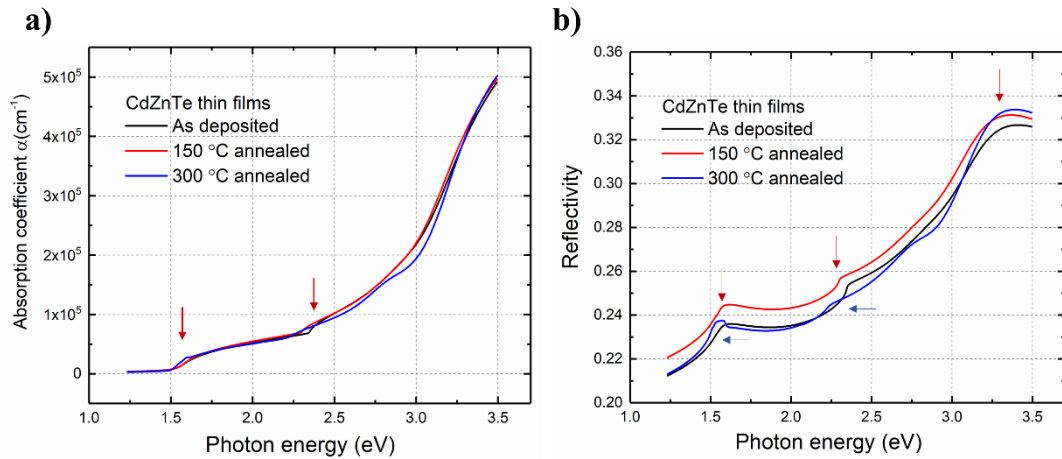
Figure 5.11. The change in absorption coefficient α (cm^{-1}) and normal incidence reflectivity for as-deposited, 150 °C and 300 °C annealed CdZnTe thin film samples.

The calculated absorption coefficients using UV-Vis Spectroscopy and VASE measurements for as-deposited and annealed CdZnTe samples were used to determine the bandgap of the films. Bandgap obtained from ellipsometer analysis has almost the same bandgap energies calculated from transmission measurements. The bandgap of as-deposited and 150 °C annealed CdZnTe samples was ~1.54 eV, while the bandgap of 300 °C annealed CdZnTe sample significantly decreased, as shown in Figure 5.12.
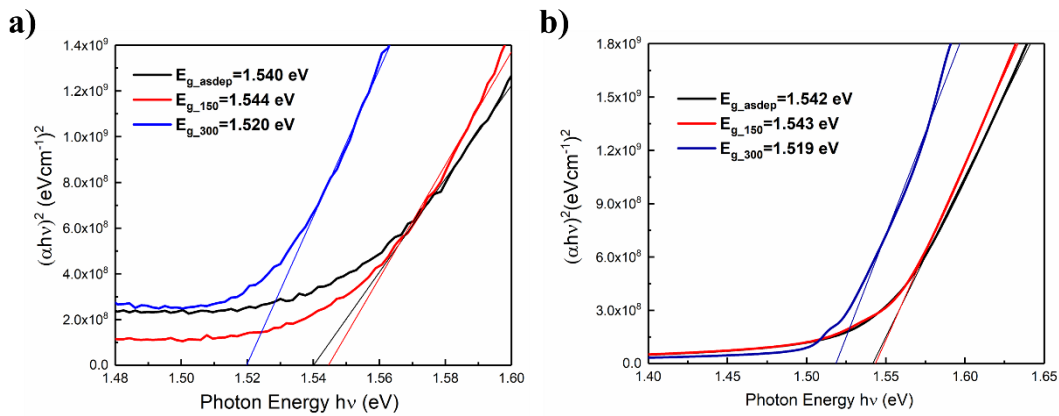
Figure 5.12. (αhν)^2 vs. hν plots of different annealing temperatures for CdZnTe thin films obtained from (a) transmission and (b) ellipsometer analysis.

CHAPTER 6

DEVICE CHARACTERIZATION OF CdS/CdZnTe THIN FILMS FOR SOLAR CELL APPLICATIONS

CdS and CdZnTe thin films with different thicknesses were fabricated by a thermal evaporation method, and electrical characterizations were performed. The thickness of the CdZnTe absorber layers was reduced to an extreme limit. Several advantages could be attained by reducing the thickness of the CdZnTe absorber layer for solar cell application. The most important benefit is reducing materials usage, especially materials such as Te, a low earth abundance material, and Cd, heavy metal with toxicity properties. Additionally, low cost of operation and reduced power consumption with reduced deposition time and decreased post-deposition processes were achieved using a thin CdZnTe absorber layer. In this study, CdS/CdZnTe solar cells with thin absorber layers were discussed. Three different CdS thicknesses of 100 nm, 120 nm and 150 nm have been studied. Additionally, CdZnTe thicknesses of 800 nm and 1500 nm have been deposited on 120 nm CdS thin films. Finally, $CdCl_2$ treatment has been performed for all CdS/CdZnTe devices, which is a vital process in the fabrication of high-efficiency and good-quality solar cells. The highest short-circuit current density was obtained in the CdS/CdZnTe device using the 120 nm CdS film as a window layer with an 800 nm CdZnTe absorber layer. Therefore, an annealing process was applied to this device after contact deposition to investigate the effect of temperature on the device parameters. The fill factors of fabricated devices were higher than 35%, and the best Voc value was obtained for 1500 nm thick CdZnTe with 280 mV. Low device performance was obtained using CdS/CdZnTe solar cells with submicron absorber layer thicknesses due to shunting problem, high series resistance, incomplete photon absorption, and fully depleted CdZnTe absorber layer. Therefore, possible reasons for the low performance were also discussed.

6.1   Introduction

Even though CdTe is the leading thin film material for solar cell applications with 22.1% efficiency [7], higher efficiencies could be reached by a tandem cell design with two-cell structures of optimum bandgaps of 1.7 eV for the top cell and 1.1 eV for the bottom cell [12], [111]. The addition of Zn to CdTe, resulting in the ternary compound cadmium zinc telluride ($Cd_{1-x}Zn_xTe$), improves the quality of the material and makes p-type doping much easier [8], [9]. $Cd_{1-x}Zn_xTe$ is a promising candidate as the top cell due to its direct tunable bandgap (from 1.45 eV to 2.26 eV), high absorption coefficient ($>10^5$ cm^{-1}), and high atomic numbers (Cd:48, Zn:30, Te:52) [62], [112]. Several techniques have been used for the deposition of $Cd_{1-x}Zn_xTe$ thin films, including molecular-beam epitaxy, magnetron sputtering, closed-space sublimation, and thermal vacuum evaporation. In this study, to obtain the desired film quality at low substrate temperatures with a low cost of operation and reduced power consumption, the thermal evaporation method was employed to fabricate both CdS and CdZnTe layers. Additionally, this study utilized thin CdZnTe (<2μm) films that are cost-effective due to the less material usage.

Although CdZnTe material has extremely important properties enabling it to be used for various critical industrial applications, the efficiencies of CdS/CdZnTe based solar cells are limited to about 10% [35]–[37]. Additionally, when solar cells are fabricated with submicron absorber layer thicknesses, cell performance is generally reduced considerably owing to the incomplete optical absorption in the thin absorber layer [113], [114]. Indeed, a recent study shows that thin CdS/CdTe solar cells produced by the thermal evaporation method with thicknesses of 100/500 nm yielded a conversion efficiency of 3.73%, with R_S, R_{sh}, V_{oc}, J_{sc} and FF values as 12.5 Ωcm^2, 636 Ωcm^2, 577.8 mV, 11.724 mA/cm^2 and 55.12%, respectively [115]. However, there are rather few studies conducted to explain the low performance of thin CdS/CdZnTe devices. CdZnTe thin films have been widely characterized regarding their structural, optical, and morphological properties [50], [76], [116], [117]. Nevertheless, very few attempts have been carried out to investigate the effect of both

94

CdS and CdZnTe film thicknesses on device parameters [118]–[120]. In this study, the electrical properties of CdS-CdZnTe thin films were examined according to various CdS and CdZnTe layer thicknesses and the post-deposition annealing process after contact formation.

6.2 Experimental Details

Fabrication of CdS/CdZnTe thin film heterojunction solar cell devices consisted of several steps. First, Indium-tin-oxide (ITO) coated glass substrates were thoroughly cleaned. Then, CdS window layers with different thicknesses were deposited on ITO-coated glass substrates by thermal evaporation with CdS powder (99.99%) as source material. CdS window layer has a bandgap energy of E_g=2.4 eV and a high doping level of 2×10^{18} cm^{-3} with n-type conductivity. Then, the CdZnTe absorber layer was deposited onto the CdS window layer. The absorber layer is the most important component in the solar cell structure since the charge carrier generation and separation occur in the absorber layer [121]. Since higher carrier concentration was produced in the CdS layer compared to the CdZnTe layer, a depletion region was mainly formed within CdZnTe. CdZnTe layers with different thicknesses were thermally evaporated on CdS/ITO/glass substrates using single-crystal pieces with 99.999% purity. In order to eliminate shunting problems, deposition of CdZnTe was performed in two steps. The first CdZnTe layer was deposited by an evaporation process with a lower deposition rate, and then the second CdZnTe layer was deposited by a standard evaporation process. The bilayer structure was expected to provide good adhesion properties resulting in compact and uniform CdZnTe layers without pinholes and cracks among grain boundaries. These dense and smooth CdZnTe thin films could solve the shunt problem. During all deposition processes, the chamber pressure was held at 10^{-6} mbar, and the substrate temperatures were kept at room temperature. Simultaneously, CdS and CdZnTe thin films were also deposited on glass substrates with the same deposition parameters to enable the characterization of structural and optical properties of the films. Additionally, wet

CdCl$_2$ treatment followed by an annealing process has been carried out for all CdS/CdZnTe thin film solar cell devices to activate the interface between the CdS and CdZnTe films. Finally, deposition of the Au layer was performed using Cu shadow masks with dots of a 500 µm radius. Since Cu diffusion causes instabilities by extending deeply into the thin absorber layer [63], only Au metal was deposited as the back electrical contact to complete the device. Finally, an annealing process at 200 °C under an N$_2$ atmosphere was applied after contact deposition to investigate the effect of temperature on device parameters. The fabrication steps for CdS/CdZnTe thin film heterojunction solar cells are shown in Figure 6.1.
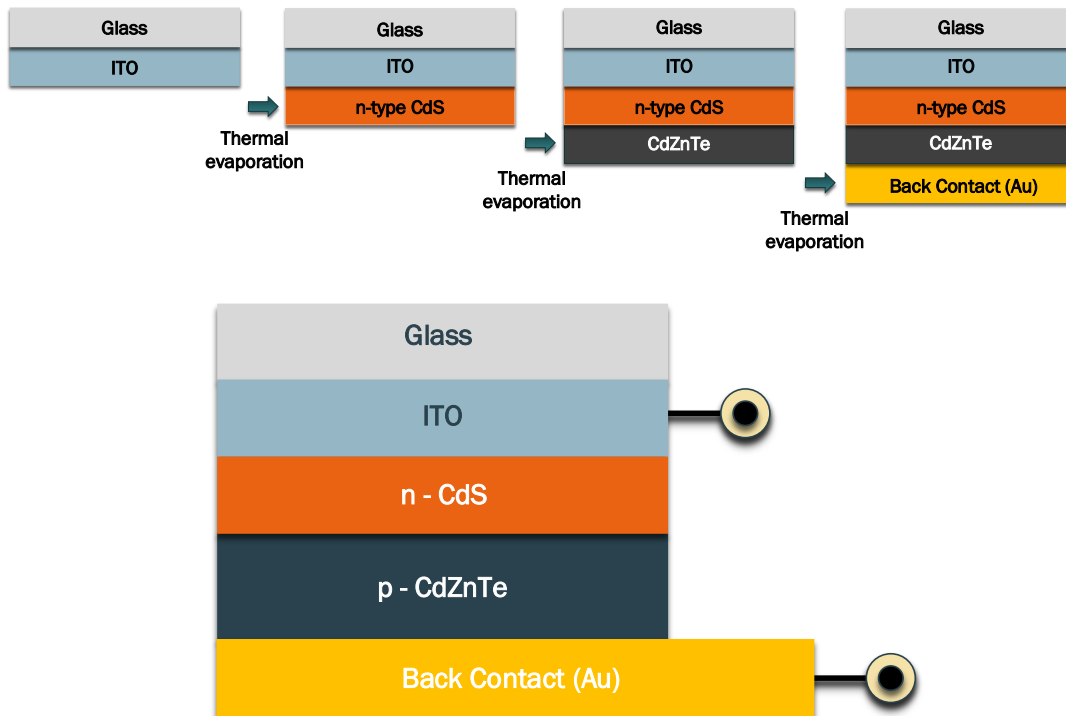
Figure 6.1. Fabrication steps for CdS/CdZnTe thin film solar cells.

Rectification properties of ITO/CdS/CdZnTe/Au solar cells, including the ideality factor (n) and potential barrier height (Φ_b) were obtained by current-voltage measurements under dark conditions. Related measurements under illuminated conditions were investigated to assess device parameters such as series resistance

(R_s), shunt resistance (R_{sh}), open-circuit voltage (V_{oc}), short circuit current density (J_{sc}), and fill factor (FF).

6.3   Result and Discussion

6.3.1   Structural and optical analysis of CdS thin films

Thin Cadmium Sulphide (CdS) films have been used as window material in CdZnTe solar cells. Even though CdS is the most commonly used heterojunction partner to CdZnTe, there is a lattice mismatch between CdS and CdZnTe, initiating a considerable amount of defects at the interface of the junction [122]. Additionally, CdS thin films should be comparatively thin to prevent current losses due to the absorption of higher photon energies. In this study, the bandgap of CdS thin films was around ~2.4 eV, so photons with ~515 nm wavelength could be absorbed. However, very thin CdS formation can be complex due to the pinhole formation resulting in shunting problems [79]. At room temperature conditions, CdS can have cubic (sphalerite), hexagonal (wurtzite), or mixed crystalline phases [123]. Nevertheless, the hexagonal structure of CdS is more stable and considered advantageous for solar cell applications. CdS with a hexagonal wurtzite crystal structure have the bulk lattice constants of a = b = 4.142 Å, c = 6.724 Å, $\alpha = \beta = 90.0°$, and $\gamma = 120.0°$. In this study, CdS films were deposited on glass and ITO substrates using the thermal evaporation method. Characterization of structural and optical analyses of CdS thin films on glass substrates was performed using XRD and transmission measurements.

Figure 6.2 reveals the XRD pattern of CdS thin films with different thicknesses having a hexagonal crystal structure. The preferential peak observed at ~26.2° corresponds to the CdS (002) plane, while an additional peak with much lower intensity appears at 47.5°, related to the CdS (103) plane. The peak intensity of the preferred CdS (002) orientation was observed to increase with increasing thickness, attributed to the improved crystallinity.
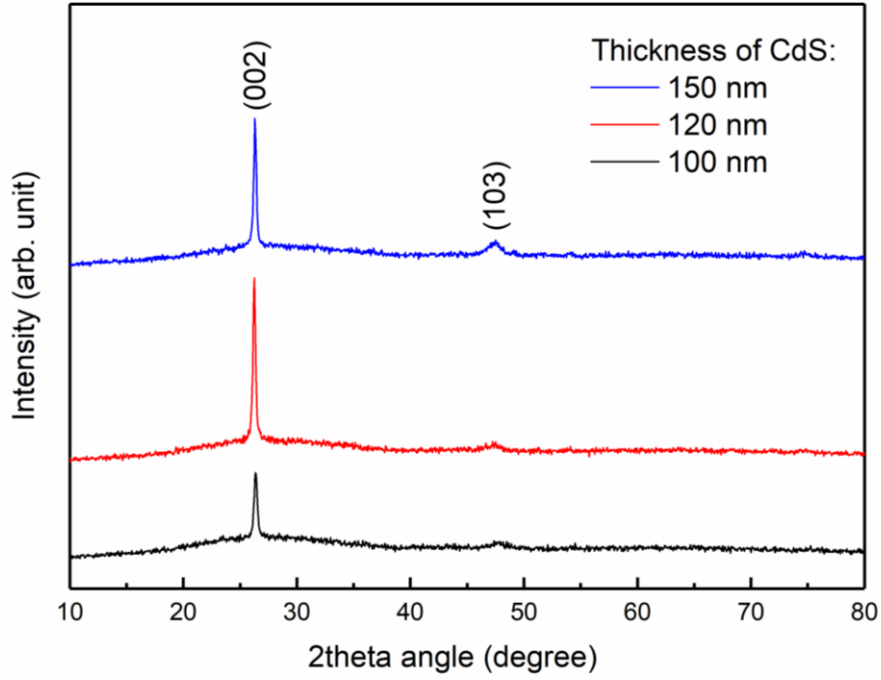
Figure 6.2. XRD pattern for various thicknesses of CdS thin films, having a hexagonal crystal structure.

Moreover, the XRD spectral analysis was used to extract valuable information about several crystallographic properties of thin films, including crystal phases, the out-of-plane and in-plane lattice constant c, and a of the hexagonal unit cell, crystalline size evolution, dislocation densities and micro-strain of the as-deposited CdS films. The lattice spacing of (hkl) oriented hexagonal wurtzite crystals is given as

$$\frac{1}{d^2} = \frac{4}{3}\left(\frac{h^2 + hk + k^2}{a^2}\right) + \frac{l^2}{c^2} \qquad \text{Equation 6.1}$$

and the equivalent lattice constant of a cubic crystal can be co-related by

$$a_{hex} = \left(\frac{1}{2}\right)^{\frac{1}{2}} a_{cubic} \qquad \text{Equation 6.2}$$

And,

$$c_{hex} = \left(\frac{4}{3}\right)^{\frac{1}{2}} a_{cubic} \qquad \text{Equation 6.3}$$

The structural parameters, including lattice constants, FWHM, average crystalline size, dislocation density, micro-strain values of CdS films with different thicknesses, were calculated and displayed in Table 6.1.

Table 6.1 Structural parameters of CdS thin films with different thicknesses.

Parameters	100 nm CdS	120 nm CdS	150 nm CdS
2θ of (002) peak degree (°)	26.2	26.2	26.3
Lattice constant (Å)	$c_{hex} = 6.80$ $a_{cubic} = 5.89$	$c_{hex} = 6.79$ $a_{cubic} = 5.88$	$c_{hex} = 6.70$ $a_{cubic} = 5.86$
FWHM (°)	0.27	0.25	0.25
Crystalline size (nm)	31.3	34.6	33.9
Dislocation density δ $(\times 10^{10}\ cm^{-2})$	10.2	8.3	8.7
Micro-strain ε $(\times 10^{-3})$	5.1	4.6	4.7

The calculated structural parameters in Table 6.1 indicate that 120 nm CdS thin film had the best structural properties. A slight decrease was observed in dislocation density and micro-strain for CdS with 120 nm thickness thanks to the relative enhancement in crystallinity and a slight increase in crystalline size. Moreover, the dislocation density and micro-strain of 100 nm CdS film was considerably high, indicating poor crystalline quality. Additionally, it was observed that CdS (~5.9 Å) and CdZnTe (~6.4 Å) had different lattice constants. Therefore, CdS/CdZnTe heterojunction suffered from a significant lattice mismatch of around 9%.

The transmittance behavior of CdS thin films on glass substrates is given in Figure 6.3. The transmittance of CdS was higher than 80% for wavelengths from 650 to 1000 nm. The bandgap energies are shown in the inset of Figure 6.3. The bandgap of 120 nm and 150 nm thick CdS was 2.40 eV, while 100 nm thick CdS had a slightly larger bandgap energy of 2.42 eV. Bandgap energy values for the ITO/CdS/CdZnTe/Au solar cell were used to draw the band diagram, which is shown in Figure 6.4.
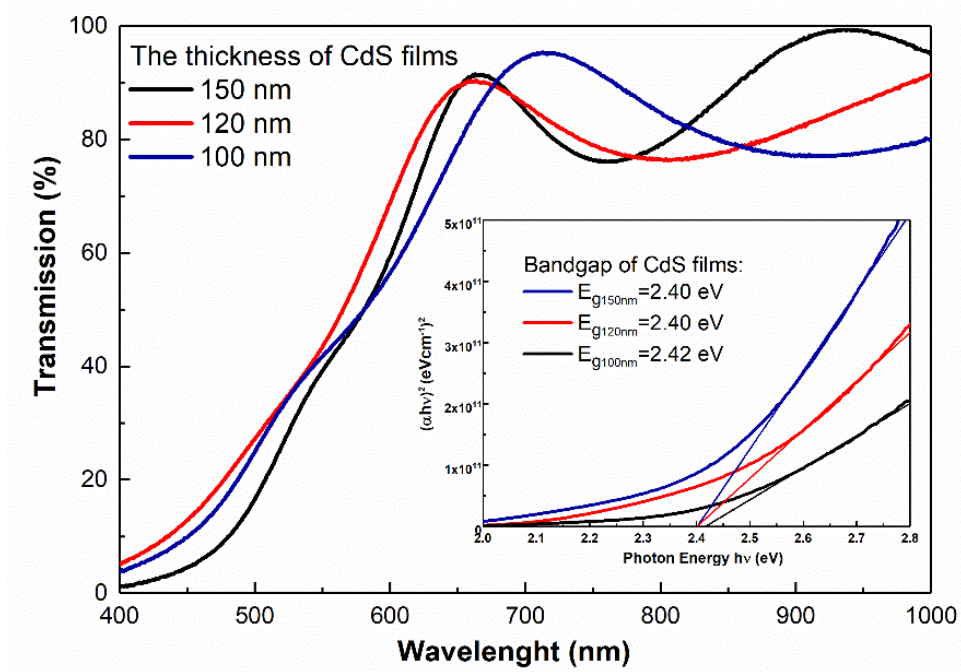
Figure 6.3. Transmittance spectra and $(\alpha h\nu)^2$ vs. $h\nu$ plots for CdS films with different thicknesses.
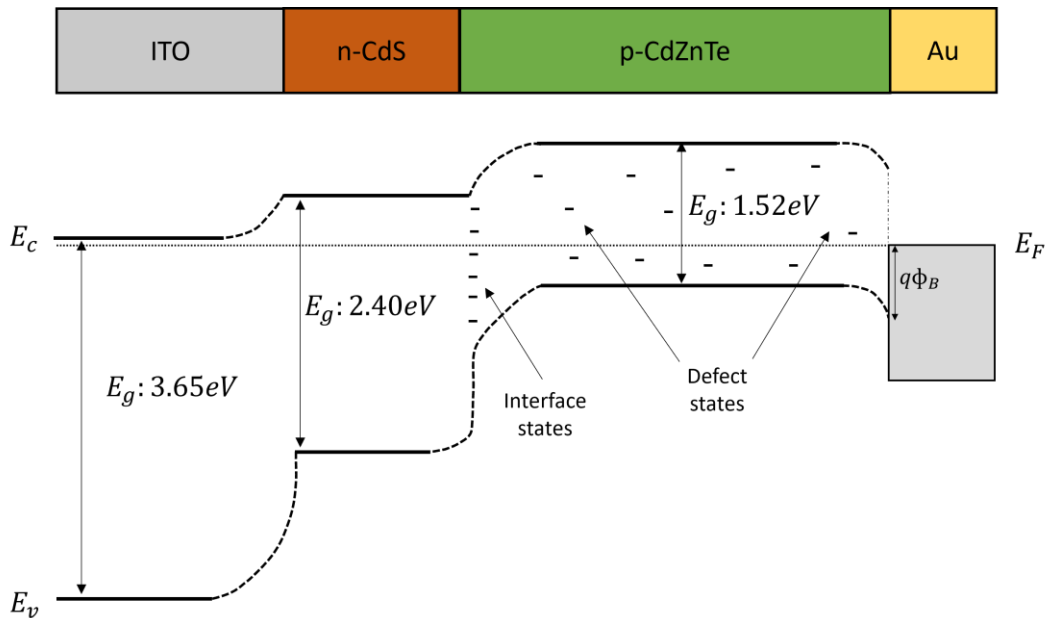
Figure 6.4. Proposed bandgap diagram for the ITO/CdS/CdZnTe/Au solar cell.

6.3.2 Current-Voltage Characteristics for CdS/CdZnTe Solar Cell Devices

Five ITO/CdS/CdZnTe/Au solar cell devices have been characterized in terms of current-voltage measurements both under dark and illuminated conditions, and device parameters have been calculated accordingly. Figure 6.5 demonstrates the current-voltage characteristics of all devices under dark conditions, which exhibited good rectifying properties.
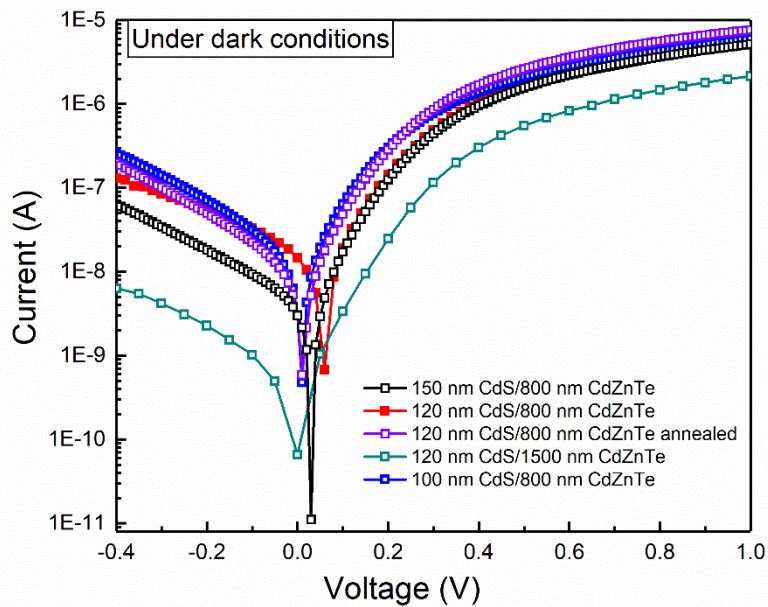
Figure 6.5. Current-Voltage characteristics under dark conditions.

The performance of solar cells is described using three main parameters, which are, J_{sc}, V_{oc} and FF. Figure 6.6 indicates the current density-voltage (J-V) curves of the ITO/CdS/CdZnTe/Au solar cells with differing CdS thicknesses. It is obvious that the window layer thickness affects mainly J_{sc}. Figure 6.7 and Figure 6.8 illustrate the J-V curves of the ITO/CdS/CdZnTe/Au solar cells with various CdZnTe absorber layer thicknesses and the effect of the post-deposition annealing process after contact formation, respectively. The thickness of the absorber layer and annealing process highly affect the solar cell parameters; V_{oc}, J_{sc} and FF. Finally, the device performance results for each device are tabulated in Table 6.2. The n and Φ_b values

were calculated from the dark current-voltage curve using Equation 2.28 and Equation 2.29. Series resistance, R_s and shunt resistance, R_{sh}, values were obtained from the slopes of the current density-voltage curve under illumination at $V = 0$ and at $I = 0$, respectively.
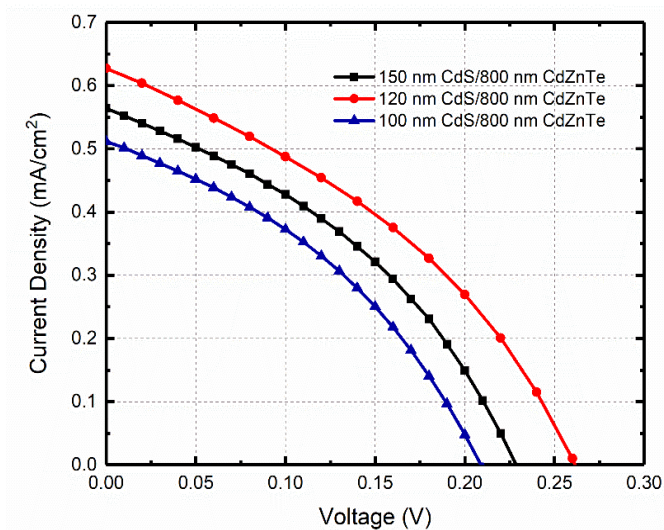
Figure 6.6. Current Density-Voltage plot under AM1.5 illumination for different CdS film thicknesses.
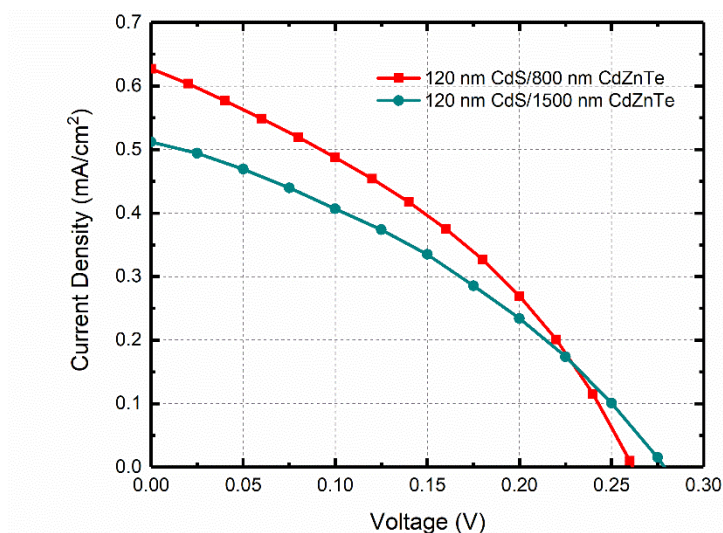
Figure 6.7. Current Density-Voltage plot under AM1.5 for different CdZnTe film thicknesses.
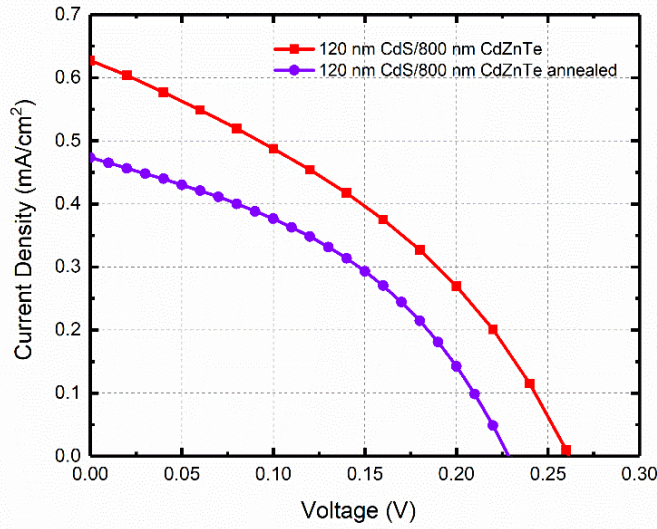
Figure 6.8. Current Density-Voltage plot under AM1.5 illumination after the post-deposition annealing process.

Table 6.2 Device parameters of CdS/CdZnTe from I-V measurements in the dark and under illumination.

Sample	n	Φ_B (eV)	R_s (Ωcm^2)	R_{sh} (Ωcm^2)	V_{oc} (mV)	J_{sc} (mA/cm^2)	FF
150nm CdS/800nm CdZnTe	1.59	0.79	79.9	824.3	213	0.58	38.8
120nm CdS/800nm CdZnTe	1.47	0.82	81.7	895.8	262	0.65	37.4
Annealed 120nm CdS/800nm CdZnTe	1.36	0.80	74.7	1181.4	229	0.48	41.4
120nm CdS/1500nm CdZnTe	2.00	0.82	83.7	939.6	280	0.51	35.6
100nm CdS/800nm CdZnTe	1.71	0.78	90.8	819.8	224	0.47	37.0

As tabulated in Table 6.2, the best diode ideality factor, n, is obtained for 120 nm CdS/800 nm CdZnTe after the annealing process. The rest of the devices have a high ideality factor, much greater than unity, deteriorating device parameters. Current in an ideal p-n junction, the ideality constant has a value near unity. Deviation from unity in the value of n is ascribed as the presence of defects in the CdZnTe absorber layer and at the CdS/CdZnTe interface [124].

Potential barrier height Φ_B for diodes are in the range between 0.78 to 0.82 eV. Both 120 nm CdS/800 nm CdZnTe and 120 nm CdS/1500 nm CdZnTe devices have a relatively higher potential barrier and, as a result, high V_{oc}. The maximum V_{oc} is obtained for the device with the 1500 nm thick CdZnTe absorber layer with 280 mV. The relatively large V_{oc} values for ITO/CdS/CdZnTe/Au devices indicate an efficient separation of carriers in the structure. In general, obtained FF values are higher than 35%. The Fill Factor is mainly affected by high series resistance. Additionally, lattice mismatch increases the number of interfacial defect states, deteriorating the device performance by raising carrier recombination losses. Recombination in the depletion region can reduce FF by increasing n and decreasing V_{oc}.

The series resistance of all CdS/CdZnTe devices is significantly high. R_s depends on the thickness of the CdS window layer, and it decreased as the thickness of the CdS increased [125]. The lowest R_s value is obtained for annealed 120 nm CdS/800 nm CdZnTe device which has the highest fill factor value. Annealing process improves not only the adhesion of metal contact but also the interface/junction properties. The best cell efficiency obtained after annealing was around 0.1%. On the other hand, the highest R_s value is found for 100 nm CdS/800 nm CdZnTe with the lowest R_{sh} and FF. As the thickness of the CdS window layer decreases, series resistance of the device becomes more apparent. Additionally, it can be deduced that the series resistance and shunt resistance of the device can considerably reduce the fill factor. In a solar cell, current is controlled by R_s value. The major contributions of R_s originate from the bulk resistance of p- and n-type regions and metal resistance [126]. FF and J_{sc} decrease rapidly with a modest increase in R_s. Additionally, the low value of R_{sh} can be attributed to the potential point defects generated in the n-CdS/p-CdZnTe heterojunction during the deposition of CdZnTe layer. As the value of R_{sh} is lowered, the leakage paths for the photo-generated charge carriers are maximized. Consequently, the amount of current loss through the leakage path is increased and the current that flows through the external circuit will decrease. The 100 nm CdS/800 nm CdZnTe device has relatively lower shunt resistance and higher series resistance, hence, the short circuit current and FF are the lowest.

CHAPTER 7

ELECTRICAL CHARACTERIZATION OF CdZnTe/Si DIODE STRUCTURE

Temperature-dependent current-voltage $(I - V)$, and frequency-dependent capacitance-voltage $(C - V)$ and conductance-voltage $(G - V)$ measurements were performed in order to analyze the diode characteristics of CdZnTe/Si structure. Obtained profiles enable us to understand the different characteristics of the diode structure, such as the carrier conduction mechanism and the nature of the interfacial layer. Over the temperature range between 220 and 340 K, taking into consideration the disparity in the forward-biased current, the diode parameters such as saturation current (I_0), zero-bias barrier height (Φ_{B0}) and ideality factor (n) have been obtained. The barrier height increased (0.53 eV to 0.80 eV) while the ideality factor decreased (4.63 to 2.79) with increasing temperature from 220 K to 340 K, indicating improvement in the junction characteristics at high temperatures. Due to the inhomogeneity in barrier height, the conduction mechanism was investigated by Gaussian distribution analysis. Hence, the mean zero-bias barrier height $(\overline{\Phi}_{B0})$ and zero-bias standard deviation (σ_0) were calculated as 1.31 eV and 0.18, respectively. Moreover, for holes in p-type Si, the Richardson constant was found to be 32.09 A cm^{-2}K^{-2} via a modified Richardson plot. Using the capacitance-voltage $(C - V)$ and conductance-voltage $(G - V)$ characteristics, series resistance (R_s) and density of interfacial traps (D_{it}) have also been investigated in detail. A decreasing trend for R_s and D_{it} profiles with increasing frequency were observed due to the impurities at the CdZnTe/Si interface and interfacial layer between the front metal contact and CdZnTe film.

7.1 Introduction

CdZnTe is a ternary II-VI semiconductor material with a high atomic number that provides strong absorption [127], [128]. It also has excellent optoelectronic properties and low leakage current due to its wide bandgap properties. CdZnTe is used in many important applications, such as solar cells, photodiodes, photoconductors, room temperature gamma-ray, X-ray detectors, infrared windows, and light-emitting diodes. In this study, a detailed analysis of the electrical properties of the CdZnTe/Si structure has been examined, and it has been stated that Si semiconductor material could be a proper heterojunction partner. The reasoning behind the production of CdZnTe/Si diode was the fact that the properties of Si material are very well-known, which assists the evaluation of the electrical response of the film in the junction.

National Renewable Energy Laboratory (NREL) and EPIR Technologies conducted studies to develop CdZnTe-based top cells grown on p-Si solar cells as a platform to manufacture high-efficiency tandem cells [129]. Additionally, CdZnTe thin films deposited on Si substrates by molecular-beam epitaxy (MBE) have been studied to facilitate the production of HgCdTe IR detectors [130]. MOVPE growth of thick CdZnTe epitaxial layers on Si was also analyzed for nuclear radiation detection applications [131]. In accordance with the corresponding studies, it is necessary to examine the electrical properties of the thermally evaporated CdZnTe/Si diode in a wide range of temperatures and frequencies for possible future applications. Therefore, we have conducted temperature-dependent $I - V$, frequency dependent $C - V$ and $G - V$ measurements under dark conditions. Temperature dependent $I - V$ measurements were performed in order to analyze the dominant conduction mechanisms through the junction and to determine the main diode parameters. In addition, frequency-dependent $C - V$ and $G - V$ measurements have been conducted to investigate junction properties and to understand the effect of the deep levels on the capacitance. Long-lived traps were essentially needed to identify the physical

106

processes in the diode, correlation between the formation of deep traps and potential degradation mechanisms were explored by extended range of frequencies [132].

7.2   Experimental Details

CdZnTe/Si diode structure was prepared on p-type Si substrate having (100) orientation and l $\Omega\cdot$cm bulk resistivity with 2×10^{16} cm^{-3} doping concentration. The RCA-cleaned substrate was etched in a 10% HF solution for 10 seconds instantly and loaded into the deposition chamber. Al back contact was thermally evaporated and annealed at 450 °C under continuous N_2 flow to enhance the ohmicity of Al-contact. Then, the CdZnTe layer was thermally deposited with a chamber pressure of 1×10^{-6} mbar at room temperature. The CdZnTe crystal pieces, which were used as source material, were obtained from the ingots produced by the VGF method in METU-CGL with a purity of 99.999% [133]. The evaporation rate and film thickness were monitored by InficonXTM/2 quartz crystal monitor, and CdZnTe film was deposited with a 5 Å/s evaporation rate, and the final film thickness of this layer was measured as ~750 nm by Dektak 6M profilometer. The resistivity of CdZnTe film was around 2×10^3 $\Omega\cdot$cm, which was measured using a Hall effect measurement system. Deposited CdZnTe/Si was dipped into a solution of 2.1 g $CdCl_2$ in 100 ml methanol and annealed for 15 min at 300 °C under an N_2 atmosphere prior to Au front contact formation. $CdCl_2$ treatment is a critical step in order to improve the device's performance. Then, 100 nm thick Au front contact was deposited using electron-beam evaporation, and the fabricated structure was annealed at 100 °C to enhance the adhesion of the contacts to the film surface. The cross-section illustration of the Au/CdZnTe/Si/Al diode structure is shown in Figure 7.1.
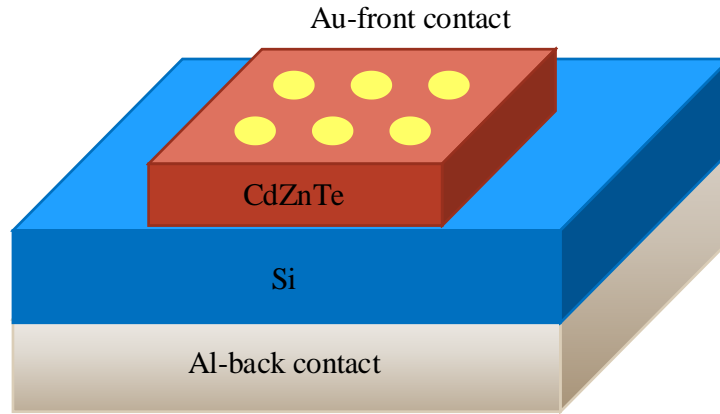
Figure 7.1. Schematic cross-section of Au/ CdZnTe/Si/Al diode structure.

The temperature-dependent $I - V$ measurements were performed for the bias voltage of $\pm$ 3 V in the temperature range of 220-340 K. Additionally, the room temperature $C - V$ and $G - V$ measurements were carried out in a wide frequency range from 1 to 1000 kHz.

7.3   Result and Discussion

7.3.1   Temperature-Dependent Current-Voltage Analysis

Temperature-dependent $I - V$ measurements were performed to determine the dominant conduction mechanisms and obtain the main diode parameters. Zero bias barrier height (Φ_{B0}) and ideality factor (n) were the two crucial parameters determined from $I - V$ plot using thermionic emission (TE) theory. The forward-biased current can be modeled using Equation 2.27 [134]. Figure 7.2 shows the $I - V$ characteristics of CdZnTe/Si diode structure at various ambient temperatures. According to the measurement results, the forward current was higher than the reverse-biased current for all temperature values, and the diode had good rectifying behavior. The ratio of forward current to reverse current (I_F/I_R) gives the rectification factor (RF), which was two orders of magnitude.

108
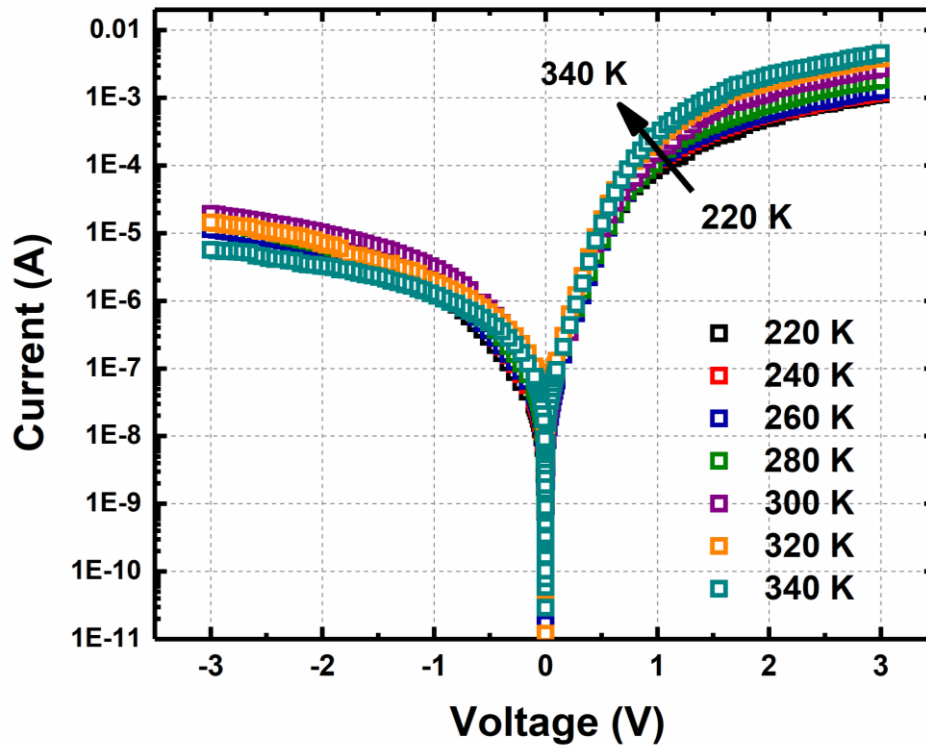
Figure 7.2. I-V characteristics of CdZnTe/Si diode structure at various ambient temperatures.

Intercepts of the $I - V$ plot with the current axis give the value of the reverse saturation current I_0 values at any given temperature. I_0 value was used to estimate the Φ_{B0} values by applying Equation 2.29 where the effective Richardson constant, A^* value for p-type Si was used as $32\ \mathrm{Acm^{-2}\,k^2}$ under the assumption of uniform barrier height formation in the diode [134]. The obtained n, I_0, and Φ_{B0} values for each temperature are tabulated in Table 7.1. The increase in Φ_{B0} and decrease in n with increasing temperature indicated an improvement in the junction [124]. The increase in Φ_{B0} with temperature provided smaller leakage current and, therefore, an increase in the rectification behavior. However, at lower temperatures, the ideality factor much greater than unity resulted in the deterioration of the device parameters [135].

Table 7.1 Diode parameters of CdZnTe/Si structure under dark conditions in the temperature range of 220-340 K.

Temperature (K)	Ideality factor (n)	Saturation current (I_0) (A)	Barrier Height Φ_{B0} (eV)
220	4.63	1.68×10^{-8}	0.53
240	4.10	1.72×10^{-8}	0.58
260	3.76	2.16×10^{-8}	0.62
280	3.50	2.73×10^{-8}	0.66
300	3.18	2.77×10^{-8}	0.71
320	2.94	2.84×10^{-8}	0.76
340	2.79	3.95×10^{-8}	0.80

Figure 7.3 shows the temperature dependence of n, Φ_{B0} and R_s of CdZnTe/Si heterojunction diode. Figure 7.3 (a) illustrates that as the ambient temperature rose, the ideality factor of the diode reduced. At lower temperatures, the ideality factor was much greater than unity resulting in deterioration of the device parameters. As shown in Figure 7.3 (b), Φ_{B0} for diode increased with increasing temperature. Increase in Φ_{B0} and decrease in n with increasing temperature indicated an improvement in the junction [124]. The series resistance of the diode must be minimal so that power is not lost to heat as a result of ohmic losses. Series resistance (R_s) was primarily dominated by bulk resistivity and contact resistance. The series resistance of the CdZnTe/Si heterojunction diode was decreased significantly as the ambient temperature was increased, as shown in Figures 7.3 (c). The increase of R_s with decreasing temperature was caused by factors responsible for an increase in n and the lack of free carriers at low temperatures.
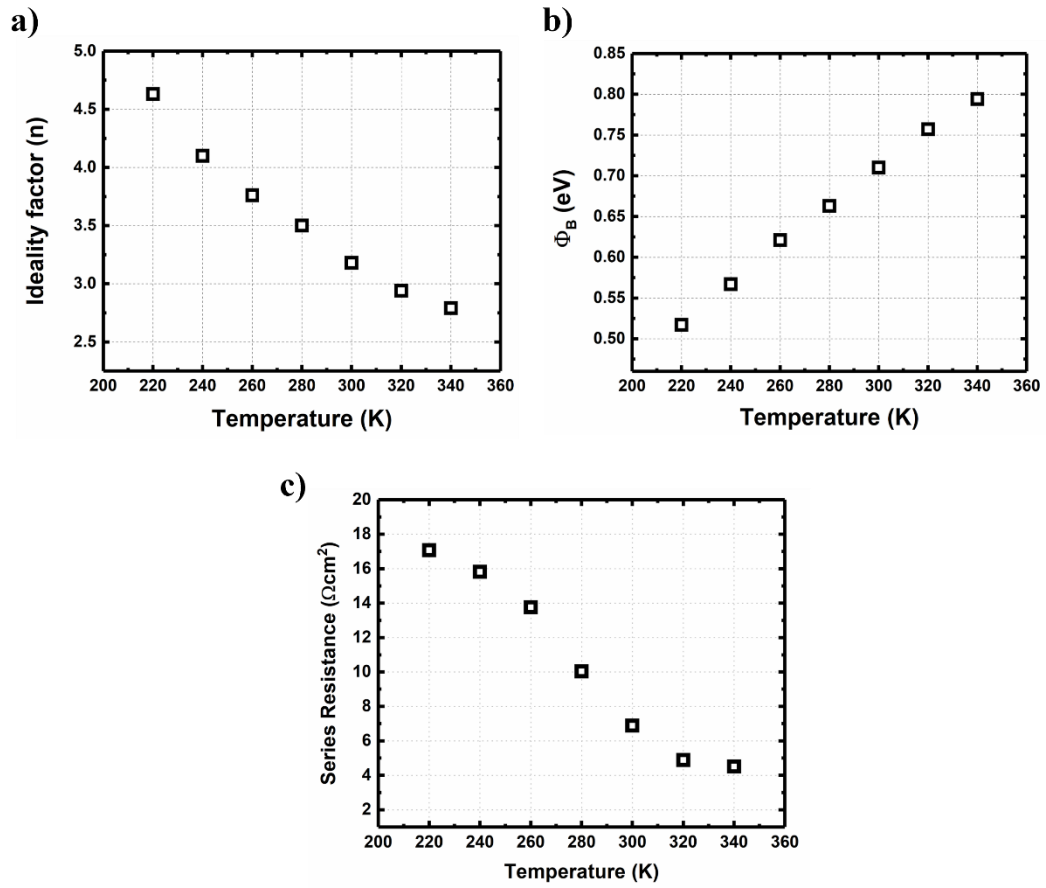
Figure 7.3. Variation of a) ideality factor, b) barrier height, and c) series resistance with various ambient temperatures for CdZnTe/Si heterojunction diode.

Because of the observed temperature dependency in the analysis, the current transport at low temperatures was controlled by the current flowing across the patches of low barrier heights, resulting in a higher n value [136]. An obvious increase in n and a decrease in Φ_{B0} at low temperatures were probably initiated by inhomogeneous barrier formation from low barrier patches [137]. However, TE theory is based on homogeneous barrier height formation in the junction. Considering the inhomogeneous barrier height formation and deviation from TE theory, Gaussian distribution (GD) of barrier height was studied based on a mean value $\bar{\Phi}_{B0}$ with the standard deviation of σ_0 to explain the carrier transport mechanism across the junction [138]–[141]. This approximation has been achieved by determining the degree of barrier height variation under Tung's theoretical

111

approach [142] and a good linear relationship between Φ_{B0} and n is obtained in Figure 7.4. In Tung's model, bias and temperature dependent diode parameters extracted from bias and temperature independent patch parameters [142].

$$I = AA^*T^2\exp\left[\left(-\frac{qV}{kT}\right)\left(\Phi - \frac{q\sigma_0^2}{2kT}\right)\right]\exp\left(\frac{qV}{n_{ap}kT}\right)\left[1 - \exp\left(-\frac{qV}{kT}\right)\right] \qquad \text{Equation 7.1}$$
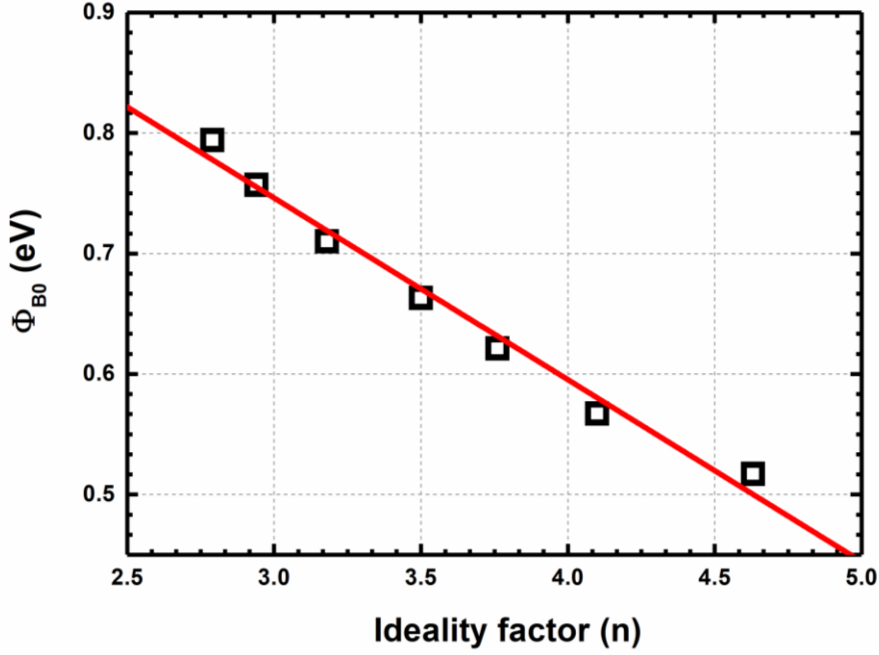
Figure 7.4. The linear relation between barrier height and ideality factor for CdZnTe/Si diode structure.

GD model was used to describe the potential fluctuations considering a continuous barrier distribution at the interface. Using the GD model, the total current was expressed as a sum of the current flows in all individual barrier patches [143]. Therefore, the total junction current dominated by low barrier patches is given as:

with modified reverse saturation current,

$$I_0 = AA^*T^2\exp\left(-\frac{q\Phi_{ap}}{kT}\right) \qquad \text{Equation 7.2}$$

where n_{ap} and Φ_{ap} are the apparent ideality factor and apparent barrier height, respectively. Using GD function, Φ_{ap} can be expressed as the temperature variation in Φ_{B0}:

$$\Phi_{ap} = \overline{\Phi}_{B0} - \frac{q\sigma_0^2}{2kT} \qquad \text{Equation 7.3}$$

As represented in Figure 7.5 (a), Φ_{B0} had a linear relation with $q/2kT$ and from the analysis of intercept and slope, $\overline{\Phi}_{B0}$ and σ_0 have been determined, respectively. The value of σ_0 was found to be 0.18, while the $\overline{\Phi}_{B0}$ value was obtained as 1.31 eV. In the GD model, σ_0, which was a measure of the barrier homogeneity, shows 14% deviation from the mean value $\overline{\Phi}_{B0}$. According to the obtained values, the forward-biased current mechanism in CdZnTe/Si diode confirmed a junction with GD of barrier height due to inhomogeneity of the interface layer and non-uniformity of interface charges. According to the GD model, ρ_2 and ρ_3, the coefficients indicating the voltage deformation of the barrier height distribution can be extracted from the following equation

$$\left(\frac{1}{n_{ap}} - 1\right) = -\rho_2 + \frac{q\rho_3}{2kT} \qquad \text{Equation 7.4}$$

While Equation 7.4 examines the relationship between temperature and n, Figure 7.5 (b) shows the corresponding voltage deformation of the GD of the barrier height with respect to n. The voltage coefficients were determined from the intercept and slope of the straight line as, $\rho_2 = 0.0153$ V and $\rho_3 = 0.387$, respectively.
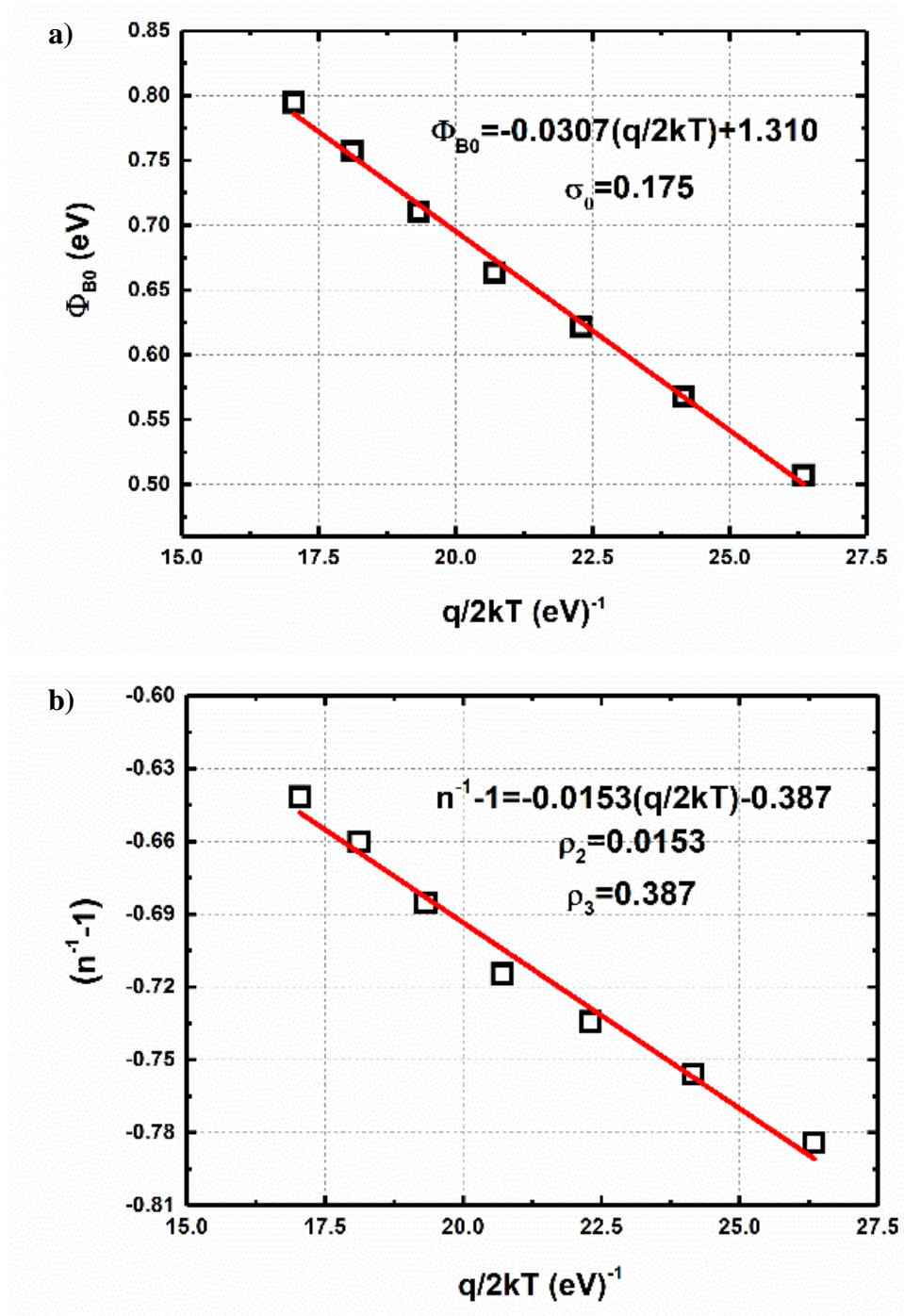
Figure 7.5. Plot of (a) Φ_{B0} vs. q/2kT and (b) $(n^{-1}-1)$ vs. q/2kT for CdZnTe/Si diode structure.

The barrier height patchiness was not only used to describe the varying barrier heights but also to calculate changing Richardson constants [49]. Therefore, modified Richardson constant A^* was calculated for GD type inhomogeneous barrier height. Using Eq. 1, modified A^* can be determined as

$$\left(\frac{I_0}{T^2}\right) - \left(\frac{q^2\sigma_s^2}{2k^2T^2}\right) = \ln(AA^*) - \frac{q\overline{\Phi}_{B0}}{kT} \qquad \text{Equation 7.5}$$

The modified Richardson plot using Equation 7.5 is given in Figure 7.6. The $\overline{\Phi}_{B0}$ and A^* values were found as 1.32 eV and 32.095 Acm^{-2}k^{-2} from the slope and intercept of the $\ln\left[(I_0/T^2) - (q^2\sigma_0^2)/(2k^2T^2)\right]$ vs. q/kT plot, respectively. The value of $\overline{\Phi}_{B0}$ obtained using Equations 7.3 and 7.5 were found to be very similar. Even the inhomogeneity of the barrier height existed in the diode, the modified A^* value was in accordance with the reported values [144].
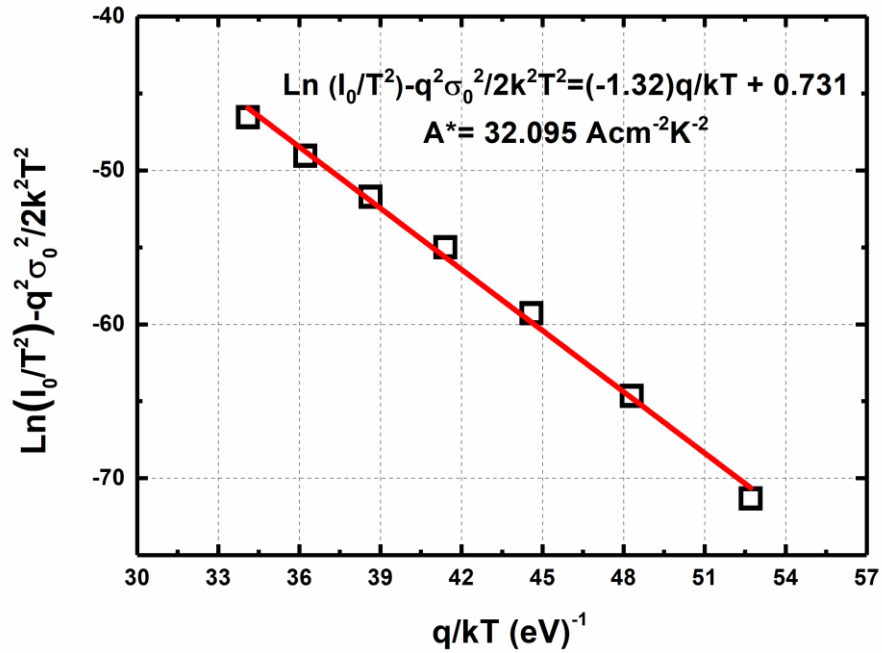
Figure 7.6. ln[(I$_0$/T^2)-(q^{2}σ$_0$^{2})/(2k^{2}T^2)] vs. q/kT for CdZnTe/Si diode structure.

7.3.2 Frequency-Dependent Capacitance-Voltage Analysis

In this study, the frequency dependence of $C - V$ and $G - V$ characteristics of Au/CdZnTe/Si/Al diode structure have been investigated in the frequency range of 1 kHz – 1000 kHz and voltage range of ± 3 V. Frequency-dependent analysis provided essential information about the relaxation mechanism of the interface states and the nature of the electrical conduction mechanism [145], [146]. Illustrated in Figure 7.7 (a) and Figure 7.7 (b), the capacitance and conductance of the diode showed sensitivity to applied voltage and frequency. Capacitance values were decreasing with increasing frequency. Obtained higher capacitance values at low frequencies in Figure 7.7 (a) can be related to the carrier charges at surface traps and their relaxation time since they can easily follow the ac signal and generate excessive capacitance [147]. Capacitance at high frequency represents the response of free carriers, while capacitance at low frequency represents the response of not only free carriers but also deep trap levels [147]–[149]. A significant amount of deep trap levels may co-exist with the shallow levels and contribute noticeably to the space charge [150]. The CdZnTe film may be non-intentionally doped, which suggests that free carriers are due to the defects. These defects may be intrinsic to the polycrystalline CdZnTe or due to extrinsic impurities such as Cl resulting from CdCl$_2$ treatment [151]. Ideally, the $C - V$ and $G - V$ characteristics are expected to be independent of frequency. Several mechanisms can give rise to a frequency dependent capacitance and conductance such as deep traps in CdZnTe, Cl diffusion, interface traps and high series resistance [152], [153]. On the other hand, it was observed that conductance value increases with increase of frequency in the forward bias region. The increase in conductance for higher frequencies may be an indication of improvement in conduction mechanism. The presence of spike at 0 V for all frequencies was probably resulted from the localized states that are contributing to electrical conductivity.

116
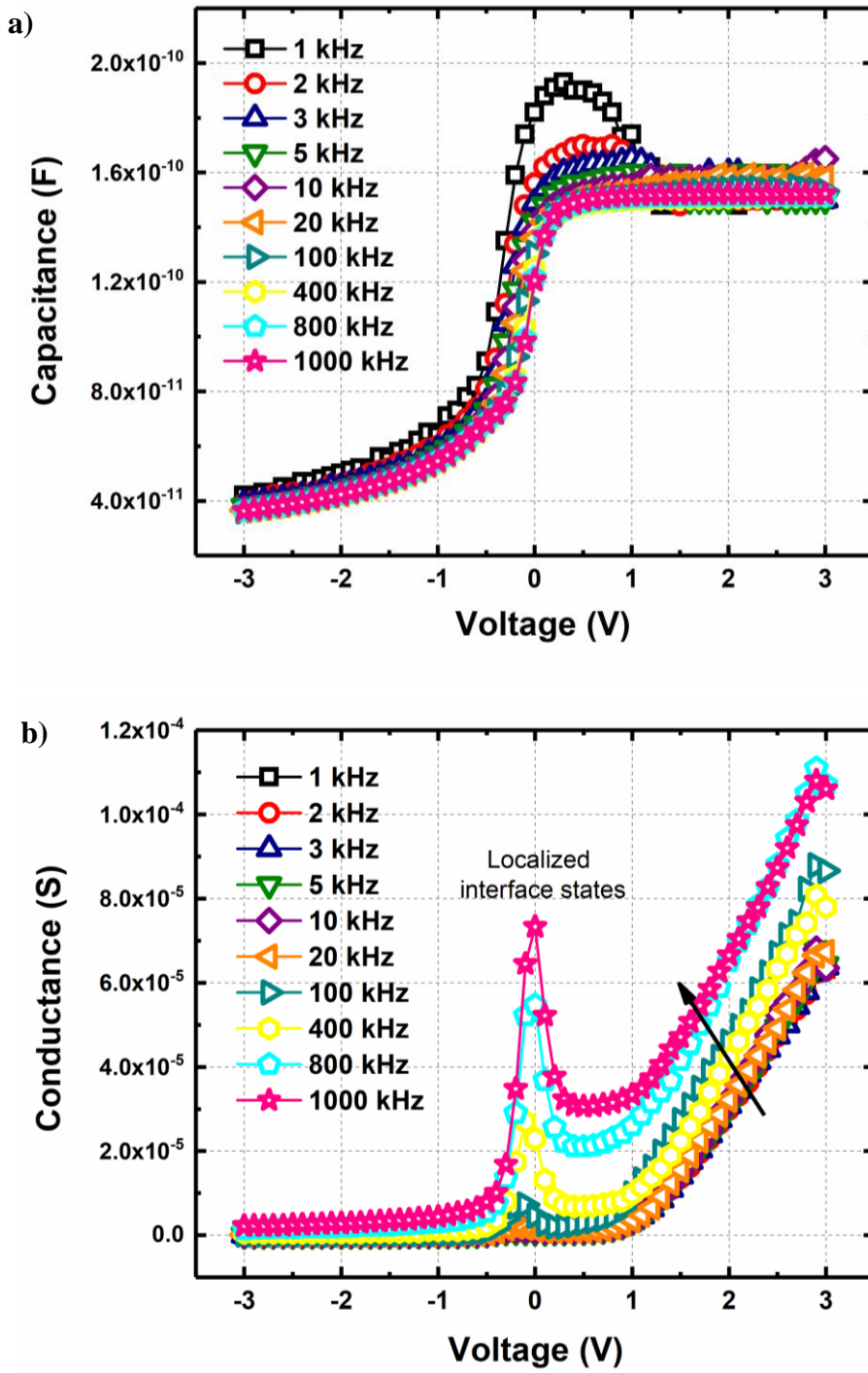
Figure 7.7. Frequency dependence of (a) C-V and (b) G-V plots of CdZnTe/Si diode structure at room temperature.

Additionally, R_s (series resistance) and D_{it} (Density of interface traps) were important parameters that have significantly changed both the $C - V$ and $G - V$ characteristics from ideal cases [152]. R_s parameter was effective in the forward bias region for high frequencies, while D_{it} was effective at low frequencies.

7.3.2.1   Series Resistance (R$_s$)

It should be noted that the value of series resistance can affect both capacitance and conductance characteristics. The value of voltage-dependent resistance R_i can be extracted in the total measurement range as

$$R_i = \frac{G_m}{G_m^2 + (\omega C_m)^2}$$ Equation 7.6

where ω $(2\pi f)$ is the angular frequency, and C_m and G_m are measured capacitance and conductance values. Though this approach evaluates the effect of parasitic resistance, at sufficiently high frequencies $(f \geq 300\ kHz)$ and in the positive voltage region, it can be used to calculate the R_s values [140], [141], [152].

The applied bias voltage and frequency dependence profile of the R_s was evaluated according to Equation 7.6 for high frequencies, and its characteristic behavior was presented in Figure 7.8. As shown in the figure, the value of R_s was increased with decreasing frequencies as a result of impurities at the CdZnTe/Si interface, CdZnTe layer and metal contact.
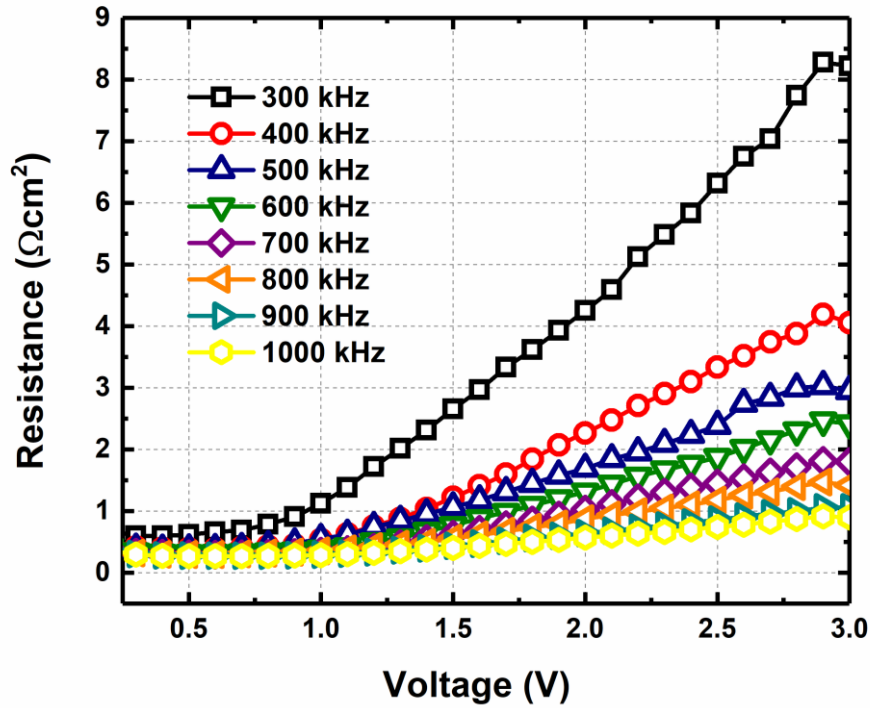
Figure 7.8. R_s at different frequencies for forward bias region of CdZnTe/Si diode structure under dark conditions at room temperature.

7.3.2.2   The Density of Interface Traps (D_{it})

D_{it} is attributed to the discontinuity of the lattice structure, surface preparation, interfacial layer, and impurities in the semiconductor [47]. In this study, two standard methods have been used to calculate D_{it}, namely the Hill-Coleman method and the high-low frequency capacitance (C_{HF}-C_{LF}) method [154].

The Hill-Coleman approximation technique is a quantitative method used to obtain the density of interface traps [73]. According to this approximation, frequency-dependent $C-V$ and corresponding $G/w-V$ plots are required for the estimation of D_{it}. As a result, frequency dependence distribution of D_{it} can be determined as [154];

$$D_{it} = \left(\frac{2}{qA}\right)\frac{(G_m/w)_{max}}{((G_m/w)_{max}/C_i)^2 + (1 - C_m/C_i)^2}, \quad C_i = C_m\left[1 + \frac{G_m}{wC_m}\right] \qquad \text{Equation 7.7}$$

where q is the elementary charge, ω ($2\pi f$) is the angular frequency, A is the diode area, G_m/w is the max-peak value of the measured conductance as shown in Figure 7.9 (a), C_m is the corresponding measured capacitance value and C_i is the interfacial capacitance.

The conductance can be considered as a measure of the interface trap density. It indicates loss mechanisms resulting from the capture of interface traps and the emission of carriers [155]. To determine the distribution of density of interface trap, G/w is calculated using each $C - V$ and $G - V$ plots at several modulation frequencies. $G/w - V$ was then plotted to extract the maximum value of G/w at each frequency which in turn gives rise to D_{it}.

The frequency distribution of the calculated D_{it} values are given in Figure 7.9 (b), and the profile of the D_{it} has shown a decreasing behavior when the applied frequency increased. When interface traps live at the interface, device performance deteriorates due to these traps and their lifetime [155]. At low frequencies, the interface traps can follow the ac signal and cause an increase in calculated D_{it}. Nevertheless, interface traps at high frequencies cannot follow an ac signal [73]. It can be deduced that the interface trap density is strongly frequency-dependent [156]. Additionally, there was a peak at about 10 kHz, corresponding to the frequencies of mainly localized defect traps.
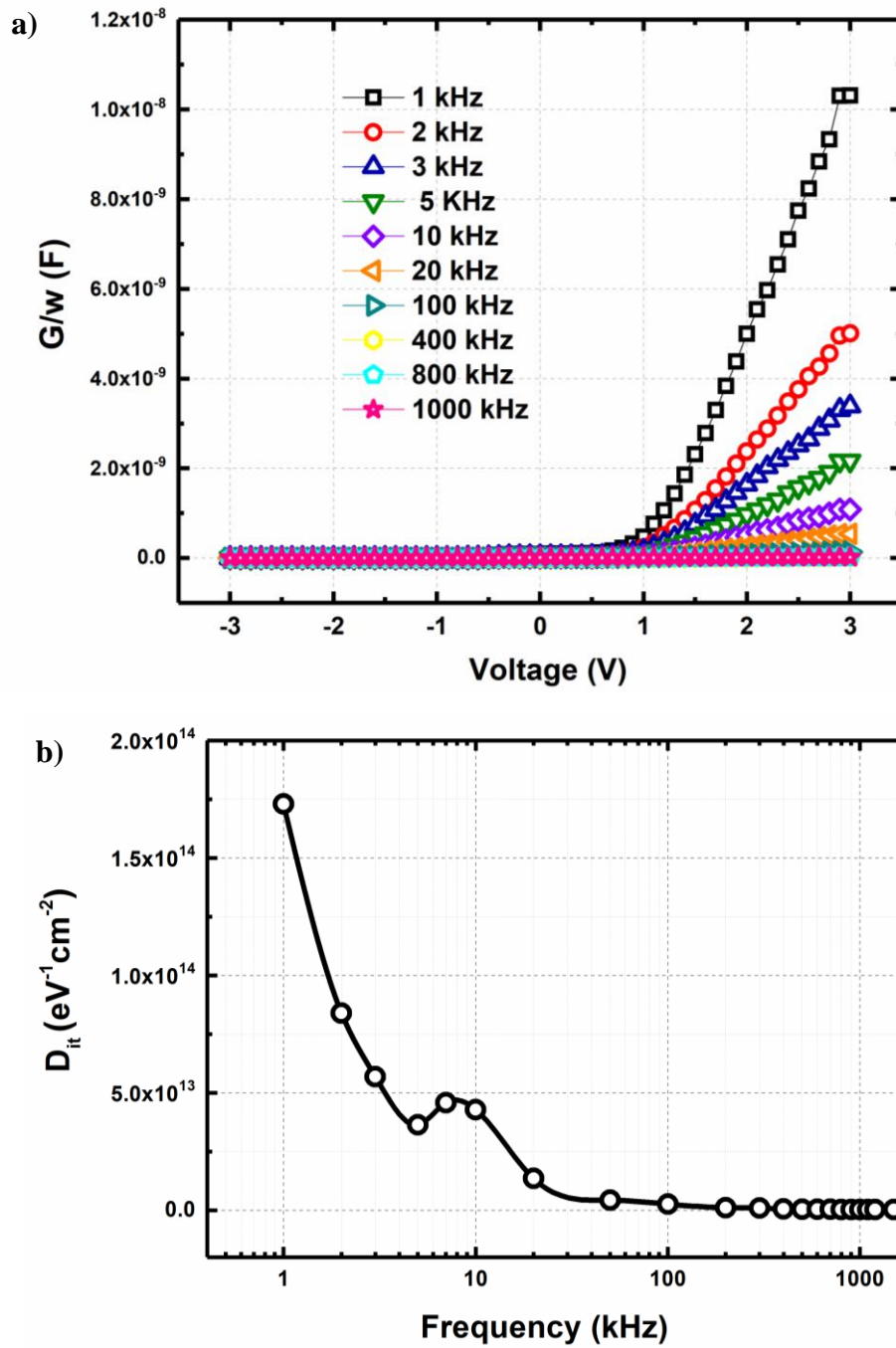
Figure 7.9. Plots of (a) G/w-V and (b) Corresponding frequency-dependent distribution of D_{it} using Hill-Coleman method for CdZnTe/Si diode.

The second method used to calculate the density of the interface traps is the C_{HF}-C_{LF} method [157], [158]. The equivalent circuits for low- and high-frequency capacitance are given in Figures 7.10 (a) and (b), respectively.
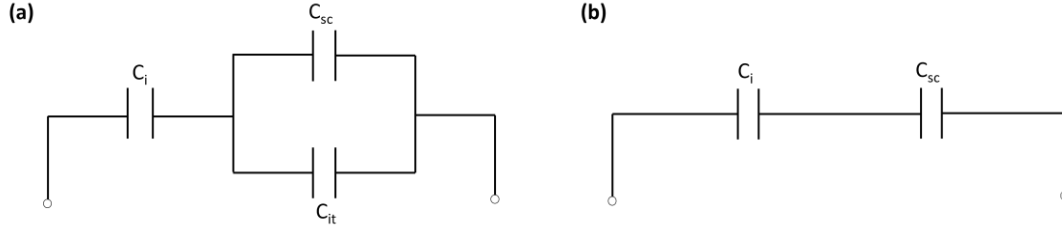
Figure 7.10. (a) Low-frequency capacitance and (b) high-frequency capacitance equivalent circuits.

The total capacitance at low-frequency, C_{LF}, given in Figure 7.10 (a), is obtained by

$$C_{LF}^{-1} = C_i^{-1} + (C_{sc} + C_{it})^{-1} \qquad \text{Equation 7.8}$$

For a low-frequency capacitance circuit, the space charge capacitance (C_{sc}) and the interface trap capacitance (C_{it}) are in parallel connections. In contrast, the interface layer capacitance (C_i) is connected in series. Since the interface states cannot follow AC signal variation at high frequencies, the C_{it} does not contribute to the total capacitance. Therefore, the total capacitance at high frequency is given as

$$C_{HF}^{-1} = C_i^{-1} + C_{sc}^{-1} \qquad \text{Equation 7.9}$$

By combining Equation 7.8 and Equation 7.9, one can get the density of the interface traps (D_{it}), which is related to the interface trap capacitance (C_{it}) as

$$qAD_{it} = C_{it} = \left[\left(C_{LF}^{-1} - C_i^{-1} \right)^{-1} - \left(C_{HF}^{-1} - C_i^{-1} \right)^{-1} \right] \qquad \text{Equation 7.10}$$

where q is the elementary charge and A is the diode area. The measured high (1000 kHz) and low (1 kHz) frequency $C - V$ curves for the CdZnTe/p-Si diode structure are given in Figure 7.11. The variation of D_{it} obtained from the C_{HF}-C_{LF} capacitance method as a function of voltage is illustrated in Figure 7.12. Figure 7.12

also presents a sharp peak at about 0.2 V, which could be described by the activation of the localized interface state at that voltage. These interface states have caused a dispersion between 1 kHz and 1000 kHz frequencies, which was apparent in Figure 7.11. The maximum values of D_{it} estimated from Hill-Coleman and C_{HF}-C_{LF} capacitance methods are ~$1.75x10^{14}$ and ~$7.80x10^{12}$ $eV^{-1}cm^{-2}$, respectively. The density obtained by the Hill-Coleman method is more significant than that obtained by the C_{HF}-C_{LF} capacitance method [159]. The C_{HF}-C_{LF} capacitance method requires precise capacitance measurements and sufficiently high frequencies; therefore, it has limitations in measuring accurate density values [49].
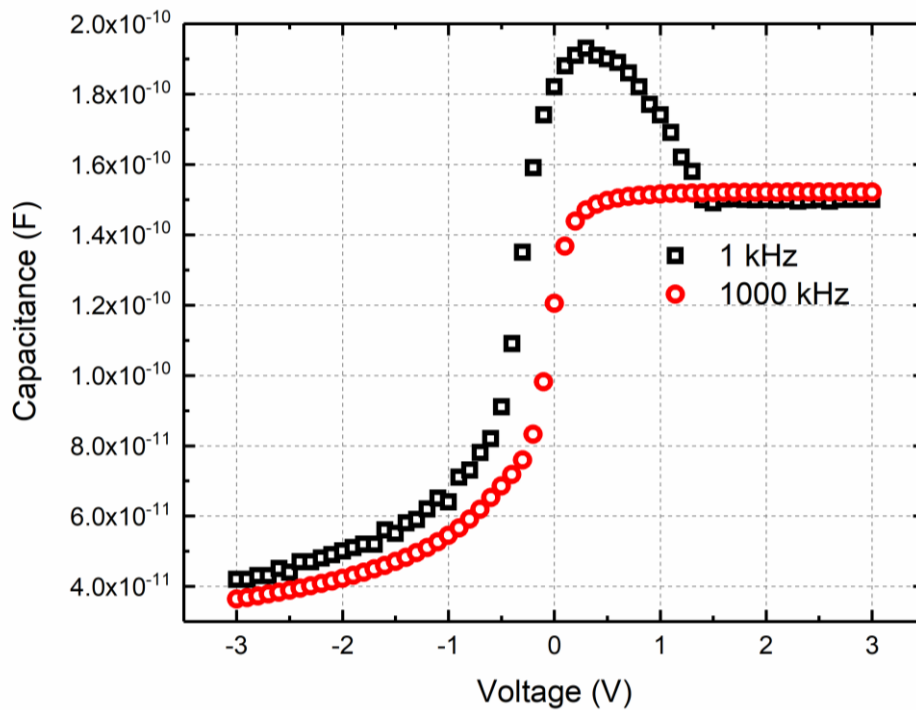
Figure 7.11. Measured high- and low-frequency C-V curves for CdZnTe/Si diode structure having an offset due to interface traps.
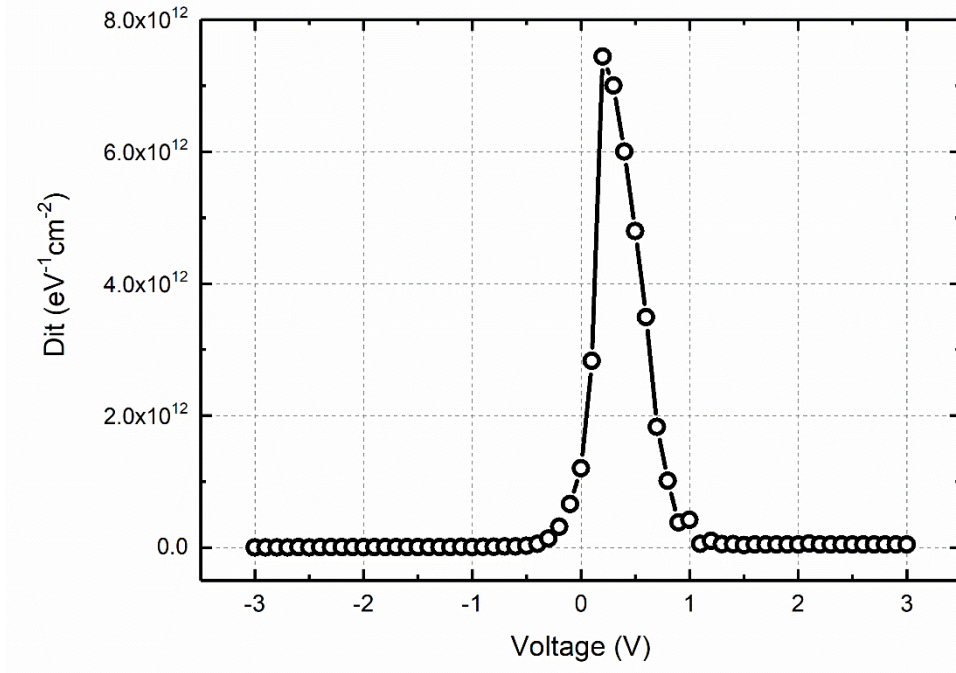
Figure 7.12. The density of interface states using the C_{HF}-C_{LF} capacitance method.

7.3.2.3   Mott-Schottky plot

Capacitance-voltage measurements were also employed to determine the carrier density and depletion width of the CdZnTe/Si heterojunction. The local slope of the Mott-Schottky plot ($1/C^2$-V plot at 1000 kHz) given in Figure 7.13 (a) is inversely proportional to the carrier density. If an abrupt junction with p+-n or n+-p formation is of concern, the variation in the built-in potential and depletion region will be mainly inside the lightly doped region. It was assumed that CdZnTe/Si was a pp+ type heterojunction. Thus, the carrier density in the CdZnTe layer was probed since the carrier density was relevant to the least doped region. For a one-sided pp+ junction;

$$N(W) = -\frac{2}{q\varepsilon_s\varepsilon_0 A^2}\frac{dV}{d(C^{-2})} \qquad\qquad W = A\frac{\varepsilon_s\varepsilon_0}{C_0} \qquad\qquad \text{Equation 7.11}$$

where W is the depletion layer width for a zero-bias voltage, ε_s is the dielectric constant (10.9 for CdZnTe), ε_0 is the vacuum permittivity (8.854×10^{-14} Fcm^{-1}), A is

124

the device area, C_0 is the capacitance for a zero-bias voltage, N is the density of shallow impurities at the edge of the depletion region.

For a uniformly doped one-sided junction, as shown in Figure 7.13, the intercept of the Mott–Schottky curve with the V-axis is equal to built-in potential, $V_{bi} - kT/q$. Additionally, the carrier concentration for p-CdZnTe was determined from the slope of the plot as N_a = 8.6×10^{14} cm^{-3} with a depletion width of ~630 nm. Using built-in potential ($V_{bi} = 0.47\ V$), the barrier height Φ_B can be calculated as

$$\Phi_B = V_{bi} + \frac{kT}{q} \ln\left(\frac{N_v}{N_a}\right) \qquad \text{Equation 7.12}$$

where N_v is the effective density of states in the conduction band ($N_v = 1.8x10^{19}\ cm^{-3}$) [160]. The barrier height was calculated using Equation 7.12, which gives a value of ~0.72 eV. The value of barrier height obtained from C-V measurements was checked for self-consistency with the dark I -V parameter at room temperature. Similar barrier height Φ_B value was obtained from both C-V and I-V measurements at room temperature.
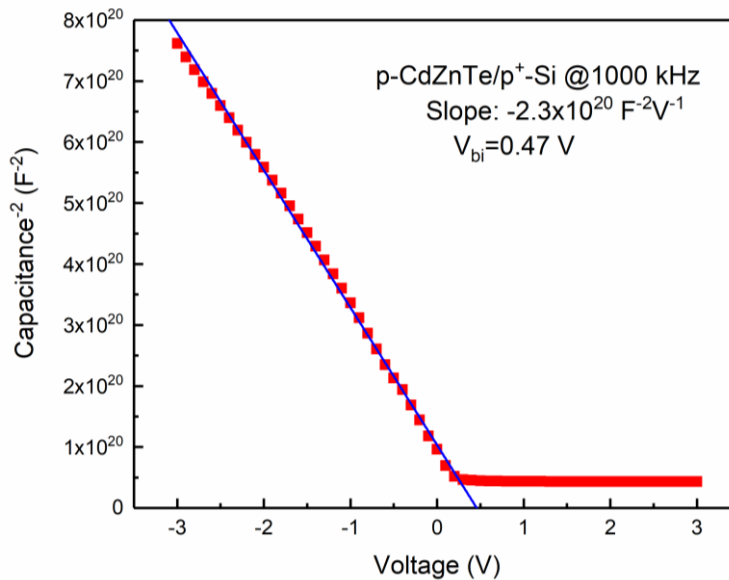
Figure 7.13. Mott-Schottky plot at 1000 kHz for CdZnTe/Si diode.

CHAPTER 8

CONCLUSION

This study focuses on the fabrication of high-quality CdZnTe thin films and material characterization strategies, including structural, morphological, optical, and electrical properties, along with device fabrication, investigation of device operation, and challenges encountered in the development of CdZnTe-based thin film devices.

In the first part of the study, we have reported the structural, optical, morphological and electrical properties of CdZnTe thin films deposited on soda-lime glass substrates at different substrate temperatures by the thermal evaporation method. Uniform and pinhole-free CdZnTe thin films were successfully obtained. The structure of the deposited films was found to be polycrystalline with a cubic zinc-blende structure. Each film had a preferred orientation along (111) directions. As the substrate temperature increased, the quality of the film was observed to increase. When the effect of different film thicknesses is of concern, semitransparent thin films (≤ 2.0 µm) had good structural and optical properties with a transmittance value higher than 75% in the near-infrared region around 1000 nm. The experimental results have revealed that annealing treatment plays an essential role in enhancing the physical properties of CdZnTe thin films. As the annealing temperature increased, the preferential XRD peak intensity increased along with other peak intensities. From optical absorption measurements, it was found that the bandgap of CdZnTe films decreased with the increase of substrate and annealing temperatures. As a result, the optical bandgap of the thin films can be tuned as desired by tailoring substrate and annealing temperatures. Finally, the effect of $CdCl_2$ treatment on the physical properties of CdZnTe thin films has been analyzed. A significant enhancement in crystallinity and grain growth has been obtained after $CdCl_2$ treatment, followed by annealing under both N_2 and air ambient. However, when CdZnTe thin film is of concern, a careful investigation should be carried out since it

was observed that the high affinity of Zn to O_2 resulted in the formation of n-type ZnO on the surface. Although $CdCl_2$ treatment is necessary to obtain high efficiencies in CdTe solar cells, the effect of $CdCl_2$ on CdZnTe solar cells was discovered to be much more complicated. Additionally, Hall effect measurements have been conducted to obtain electrical transport properties such as charge carriers, carrier concentration, electrical conductivity, and resistivity of CdZnTe thin films after $CdCl_2$ treatment. It was observed that electrons were predominant (n-type) for as-deposited and annealed CdZnTe thin films, while holes were dominant (p-type) for CdZnTe films after $CdCl_2$ treatment. Moreover, the carrier concentration increased, while resistivity decreased after $CdCl_2$ treatment.

After optimizing CdZnTe thin film growth parameters, the effect of annealing on the surface chemical compositional and optical dielectric properties of the CdZnTe absorber layer was studied by X-ray photoelectron spectroscopy (XPS) and variable angle spectroscopic ellipsometry (VASE). XPS depth analysis of atomic compositions has revealed a stoichiometric CdZnTe distribution in bulk, while the interface of the films was dominated by nature oxides and carbon contamination after the annealing. The variation of the refractive index n, extinction coefficient k, complex dielectric functions, absorption coefficient, reflectivity at a normal incident, and the layer thickness d of CdZnTe thin films were obtained using VASE analysis. Although the thickness of CdZnTe was ultra-thin and the crystalline grain size was relatively small, convenient dielectric function spectra were obtained. The electronic structure of CdZnTe thin films and their dominant optical transitions were revealed by critical point energies and their possible physical origins. The dielectric-function spectra possess distinctive energy structures at E_0, $E_0+\square_0$, and E_1 critical points equivalent to interband transitions. After annealing, the incorporation of oxides on the surface and into the bulk was confirmed by XPS and VASE analysis. Additionally, Transmission and VASE analyses have shown that the bandgap of the films decreased significantly after annealing at 300 °C due to the slight stoichiometric deviations and increase in crystalline size.

After characterization of the films, ITO/CdS/CdZnTe/Au devices were fabricated and characterized by current-voltage measurements under dark and illuminated conditions. Dark characteristics have shown diode-like behavior with an ideality factor between 1.36 and 2.00. In general, all devices have low J_{sc} values. It was observed that the thickness of the CdS window layer mainly affects the J_{sc}. The reason for low J_{sc} can be attributed to the high resistance, which increases with decreasing CdS thickness. In contrast, increasing the thickness of the CdZnTe layer enhanced the V_{oc} value of the device due to the efficient separation of the carriers. Even though annealing did not improve the V_{oc} or J_{sc}, it has enhanced the interface/junction properties and crystallinity of the films, resulting in high FF. It can be concluded that using thin CdS/CdZnTe layers has negatively influenced the performance of the device, while post-annealing treatment relatively improved the performance. The best cell efficiency was obtained to be around 0.1%, and devices suffered from high series resistance with low J_{sc} and FF. The low performance of the device can be attributed to the following reasons: (1) incomplete photon absorption resulting from the thin absorber layer; (2) recombination losses due to the interfacial defects originating from the lattice mismatch between CdS and CdZnTe; (3) FF losses due to poor diode quality, high series resistance, and electrical shunting.

In the last part of the study, an alternative CdZnTe/Si structure was fabricated for possible future device applications. In order to understand the carrier conduction mechanism and the nature of the interfacial layer of the CdZnTe/Si structure, temperature-dependent $I - V$ and frequency-dependent $C - V$ and $G - V$ profiles were investigated. $I - V$ analysis has indicated that the junction behavior has shown good rectification property. Hence, Si material can be considered a promising heterojunction partner to CdZnTe. However, the barrier height was observed to be inhomogeneous, which caused a noticeable increase in the ideality factor and a decrease in the barrier height at low temperatures. Inhomogeneity of the barrier height was observed to have a Gaussian Distribution behavior with the mean zero-bias barrier height ($\overline{\Phi}_{B0}$) and zero-bias standard deviation (σ_0) as 1.31 eV and 0.18, respectively. Additionally, using a modified Richardson plot, the modified

Richardson constant A^* was calculated as $32.09\,\mathrm{A\,cm^{-2}\,K^{-2}}$, which was approximately the same as the theoretical value for p-Si. Moreover, capacitance results have shown sensitivity to frequency. R_s value was observed to be more dominant in the impedance measurements at high frequencies in the forward bias region while D_{it} was dominant at low frequencies and the depletion region. Such non-uniformity in CdZnTe/Si structure was expected due to the diffusion mechanism of the extrinsic impurities such as Cl and the distribution of deep level traps from the complex nature of CdZnTe deposition and processing.

Further studies should be planned to improve the efficiency of CdZnTe-based devices. Appropriate window layer selection, proper surface passivation, and suitable back contact formation could be implemented to achieve good performance.

REFERENCES

[1]   Safa Kasap and Peter Capper, *Springer Handbook of Electronic and Photonic Materials*. Switzerland: Springer, 2017.

[2]   A. J. Strauss, "The physical properties of cadmium telluride," *Rev. Phys. Appl.*, vol. 12, no. 2, pp. 167–184, 1977.

[3]   A. Luque and S. Hegedus, *Handbook of Photovoltaic Science and Engineering*. 2011.

[4]   A. Bosio, N. Romeo, S. Mazzamuto, and V. Canevari, "Polycrystalline CdTe thin films for photovoltaic applications," *Prog. Cryst. Growth Charact. Mater.*, pp. 1–33, 2006, doi: 10.1016/j.pcrysgrow.2006.09.001.

[5]   B. E. McCandless and J. R. Sites, "Cadmium Telluride Solar Cells," in *Handbook of Photovoltaic Science and Engineering*, S. H. A. Luque, Ed. John Wiley & Sons, Ltd., 2003, pp. 600–641.

[6]   D. Bonnet, "CdTe Thin-Film PV Modules," in *Solar Cells*, Elsevier, 2013, pp. 225–260.

[7]   "NREL cell efficiency chart for thin film technologies," *NREL*, 2019. [Online]. Available: https://www.nrel.gov/pv/cell-efficiency.html. [Accessed: 05-May-2021].

[8]   T. Baron, K. Saminadayar, and N. Magnea, "Nitrogen doping of Te-based II-VI compounds during growth by molecular beam epitaxy," *J. Appl. Phys.*, vol. 83, no. 3, pp. 1354–1370, 1998, doi: 10.1063/1.366838.

[9]   T. Baron, S. Tatarenko, K. Saminadayar, N. Magnea, and J. Fontenille, "Plasma nitrogen doping of ZnTe, Cd1-xZnxTe, and CdTe by molecular beam epitaxy," *Appl. Phys. Lett.*, vol. 65, no. 10, pp. 1284–1286, 1994, doi: 10.1063/1.112096.

[10]   A. Rohatgi, R. Sudharsanan, S. A. Ringel, and M. H. MacDougal, "Growth and process optimization of CdTe and CdZnTe polycrystalline films for high efficiency solar cells," *Sol. Cells*, vol. 30, no. 1–4, pp. 109–122, 1991, doi: 10.1016/0379-6787(91)90043-O.

[11] F. K. Alfadhili *et al.*, "Potential of CdZnTe Thin Film Back Buffer Layer for CdTe Solar Cells," in *IEEE Photovoltaic Specialists Conference*, 2019, pp. 140–143, doi: 10.1109/PVSC40753.2019.8981338.

[12] R. Dhere, T. Gessert, J. Zhou, S. Asher, J. Pankow, and H. Moutinho, "Investigation of CdZnTe for Thin-Film Tandem Solar Cell Applications," *Mater. Res. Soc. Symp. Proc.*, vol. 763, no. April, pp. 409–414, 2003, doi: 10.1557/proc-763-b8.25.

[13] C. S. Ferekides, R. Mamazza, U. Balasubramanian, and D. L. Morel, "Cd1-XZnXTe thin films and junctions," *Thin Solid Films*, vol. 480–481, pp. 471–476, 2005, doi: 10.1016/j.tsf.2004.11.069.

[14] S. Chusnutdinow, V. P. Makhniy, T. Wojtowicz, and G. Karczewski, "Electrical properties of p-ZnTe/n-CdTe photodiodes," *Acta Phys. Pol. A*, vol. 122, no. 6, pp. 1077–1079, 2012, doi: 10.12693/APhysPolA.122.1077.

[15] Y. Zhang *et al.*, "A novel intermediate layer for Au/CdZnTe/FTO photoconductive structure," *Appl. Surf. Sci.*, vol. 388, pp. 589–592, 2016, doi: 10.1016/j.apsusc.2015.09.194.

[16] C. Szeles, "CdZnTe and CdTe materials for X-ray and gamma ray radiation detector applications," *Phys. Status Solidi Basic Res.*, vol. 241, no. 3, pp. 783–790, 2004, doi: 10.1002/pssb.200304296.

[17] S. del Sordo, L. Abbene, E. Caroli, A. M. Mancini, A. Zappettini, and P. Ubertini, "Progress in the development of CdTe and CdZnTe semiconductor radiation detectors for astrophysical and medical applications," *Sensors*, vol. 9, no. 5, pp. 3491–3526, 2009, doi: 10.3390/s90503491.

[18] J. Zázvorka, J. Franc, L. Beran, P. Moravec, J. Pekárek, and M. Veis, "Dynamics of native oxide growth on CdTe and CdZnTe X-ray and gamma-ray detectors," *Sci. Technol. Adv. Mater.*, vol. 17, no. 1, pp. 792–798, 2016, doi: 10.1080/14686996.2016.1250105.

[19] P. Bouchut, "High-efficiency infrared light emitting diodes made in liquid phase epitaxy and molecular beam epitaxy HgCdTe layers," *J. Vac. Sci. Technol. B Microelectron. Nanom. Struct.*, vol. 9, no. 3, p. 1794, 1991, doi:

10.1116/1.585801.

[20]   A. Zappettini, "Cadmium telluride and cadmium zinc telluride," in *Single Crystals of Electronic Materials: Growth and Properties*, Elsevier Ltd, 2019, pp. 273–301.

[21]   S. Adachi, "Properties of Cd(Zn)Te Relevant to Use as Substrates," in *Mercury Cadmium Telluride: Growth, Properties and Applications*, Peter Capper and Garland James, Eds. John Wiley & Sons, L td., 2011.

[22]   R. Triboulet and P. Siffert, *CdTe and Related Compounds; Physics, Defects, Hetero- and Nano-structures, Crystal Growth, Surfaces and Applications*. Oxford: Elsevier, 2010.

[23]   J. Crocco, "Crystal Growth & Technology, Device Fabrication, and Material Properties of Cd(Zn)Te for Radiation Detector Applications," Universidad Autonoma de Madrid, 2012.

[24]   Q. Zheng, "Preparation and Development of CdTe and CdZnTe Detectors for Gamma Ray Radiation Applications," 2012.

[25]   M. C. Veale, "Charge Transport and low Temperature Phenomena in Single Crystal CdZnTe," University of Surrey, 2009.

[26]   J. R. Chelikowsky and M. L. Cohen, "Nonlocal pseudopotential calculations for the electronic structure of eleven diamond and zinc-blende semiconductors," *Phys. Rev. B*, vol. 14, no. 2, pp. 556–582, 1976, doi: 10.1103/PhysRevB.14.556.

[27]   S. M. Z. Islam, "Optical Properties of Solar Cells Based on Zinc(hydr)oxide and its Composite with Graphite oxide Sensitized by Quantum Dots," p. CUNY Academic Works, 2014.

[28]   P. Capper and J. W. Garland, *Mercury Cadmium Telluride Growth, Properties and Applications*. United Kingdom: John Wiley & Sons, Ltd., 2011.

[29]   S. Adachi, T. Kimura, and N. Suzuki, "Optical properties of CdTe: Experiment and modeling," *J. Appl. Phys.*, vol. 74, no. 5, pp. 3435–3441, 1993, doi: 10.1063/1.354543.

[30]   J. T. Benhlal, K. Strauch, R. Granger, and R. Triboulet, "Temperature

dependence of the dielectric function and of the parameters of critical point transitions of CdTe," *Opt. Mater. (Amst).*, vol. 12, no. 1, pp. 143–156, 1999, doi: 10.1016/S0925-3467(98)00019-6.

[31] S. M. Sze and K. N. Kwok, *Physics of Semiconductor Devices*, vol. 10. Hoboken, New Jersey: John Wiley & Sons, 2007.

[32] L. Sun, L. Shi, and C. Wang, "Investigations of Phonons in Zinc Blende and Wurtzite by Raman Spectroscopy," *Appl. Mol. Spectrosc. to Curr. Res. Chem. Biol. Sci.*, 2016, doi: 10.5772/64194.

[33] R. Scheer and H. Schock, *Chalcogenide Photovoltaics: Physics, Technologies, and Thin Film Devices*. Wiley-VCH Verlag GmbH & Co. KGaA, 2011.

[34] K. Guergouri, R. Triboulet, A. Tromson-Carli, and Y. Marfaing, "Solution hardening and dislocation density reduction in CdTe crystals by Zn addition," *J. Cryst. Growth*, vol. 86, no. 1–4, pp. 61–65, 1988, doi: 10.1016/0022-0248(90)90699-L.

[35] B. E. McCandless, "Cadmium zinc telluride films for wide band gap solar cells," *Conf. Rec. IEEE Photovolt. Spec. Conf.*, pp. 488–491, 2002, doi: 10.1109/pvsc.2002.1190565.

[36] S. H. Lee, A. Gupta, S. Wang, A. D. Compaan, and B. E. McCandless, "Sputtered Cd1-xZnxTe films for top junctions in tandem solar cells," *Sol. Energy Mater. Sol. Cells*, vol. 86, no. 4, pp. 551–563, 2005, doi: 10.1016/j.solmat.2004.09.008.

[37] B. E. McCandless, W. A. Buchanan, and G. M. Hanket, "Thin film cadmium zinc telluride solar cells," in *4th World Conference on Photovoltaic Energy Conference*, 2006, doi: 10.1109/WCPEC.2006.279496.

[38] P. Dingus, J. Garnett, S. Wang, and C. Chong, "Low cost single crystal CdZnTe-Silicon tandem PV," *Renew. Energy*, vol. 168, pp. 659–667, 2021, doi: 10.1016/j.renene.2020.12.087.

[39] M. Carmody *et al.*, "Single-crystal II-VI on Si single-junction and tandem solar cells," *Appl. Phys. Lett.*, vol. 96, no. 15, 2010, doi: 10.1063/1.3386529.

134

[40] S. Adachi, *Optical properties of crystalline and amorphous semiconductors: Materials and Fundamental Principles*, vol. 5, no. 11. Springer, 1999.

[41] M. Ohring, "Optical Properties of Materials," in *Engineering Materials Science*, 1995.

[42] S. Adachi, *Properties of Semiconductor Alloys: Group-IV, III-V and II-VI Semiconductors*. John Wiley & Sons, Ltd., 2009.

[43] J. L. Gray, "The Physics of the Solar Cell," in *Handbook of Photovoltaic Science and Engineering*, 2011, pp. 82–129.

[44] U. K. Mishra and J. Singh, *Semiconductor Device Physics and Design*. The Netherlands: Springer, 2008.

[45] D. A. Neamen, *Semiconductor physics and devices: basic principles*. McGraw-Hill, 2003.

[46] S. J. Fonash, "Semiconductor–semiconductor Heterojunction Cells," in *Solar Cell Device Physics*, 2010, pp. 183–262.

[47] S. M. Sze, *Semiconductor Devices, Physics and Technology*, 2nd ed. John Wiley & Sons, 2002.

[48] B. L. Sharma, *Metal-Semiconductor Schottky Barrier Junctions and Their Applications*. New York: Plenum Press, 1984.

[49] Dieter K. Schroder, *Semiconductor material and device characterization*, Third Edit. New Jersey: John Wiley & Sons Inc., 2006.

[50] X. Gao, X. Zhu, H. Sun, D. Yang, P. Wangyang, and S. Zhu, "Preparation and characterization of CdZnTe multilayer films by repeated RF magnetron sputtering," *J. Mater. Sci. Mater. Electron.*, vol. 28, no. 5, pp. 4467–4474, 2017, doi: 10.1007/s10854-016-6079-8.

[51] N. Amin, A. Yamada, and M. Konagai, "Effect of ZnTe and CdZnTe alloys at the back contact of 1-μm-thick CdTe thin film solar cells," *Jpn. J. Appl. Phys.*, vol. 41, no. 5A, pp. 2834–2841, 2002, doi: 10.1143/jjap.41.2834.

[52] Y. V. Znamenshchykov, V. V. Kosyak, A. S. Opanasyuk, V. O. Dorda, P. M. Fochuk, and A. Medvids, "Raman characterisation of Cd1-xZnxTe thick polycrystalline films obtained by the close-spaced sublimation," *Acta Phys.*

Pol. A, vol. 132, no. 4, pp. 1430–1435, 2017, doi: 10.12693/APhysPolA.132.1430.

[53] G. G. Rusu, M. Rusu, and M. Girtan, "Optical characterization of vacuum evaporated CdZnTe thin films deposited by a multilayer method," *Vacuum*, vol. 81, no. 11–12, pp. 1476–1479, 2007, doi: 10.1016/j.vacuum.2007.04.003.

[54] K. Prabakar, S. Venkatachalam, Y. L. Jeyachandran, S. K. Narayandass, and D. Mangalaraj, "Optical constants of vacuum evaporated Cd0.2Zn0.8Te thin films," *Sol. Energy Mater. Sol. Cells*, vol. 81, no. 1, pp. 1–12, 2004, doi: 10.1016/j.solmat.2003.08.008.

[55] A. Romeo, E. Artegiani, and D. Menossi, "Low substrate temperature CdTe solar cells: A review," *Sol. Energy*, vol. 175, pp. 9–15, 2018, doi: 10.1016/j.solener.2018.02.038.

[56] M. Chakraborty and M. S. J. Hashmi, "Simultaneous vacuum evaporation for CZT thin film fabrication," *Adv. Mater. Process. Technol.*, vol. 5, no. 4, pp. 645–652, 2019, doi: 10.1080/2374068X.2019.1666503.

[57] R. Asthana, A. Kumar, and N. Dahotre, "Materials Processing and Manufacturing Science," *Mater. Process. Manuf. Sci.*, 2006, doi: 10.1016/B978-0-7506-7716-5.X5000-6.

[58] N. Amin, M. R. Karim, and Z. A. ALOthman, "Impact of CdCl2 Treatment in CdTe Thin Film Grown on Ultra-thin Glass Substrate via Close Space Sublimation," *crystals*, vol. 11, no. 390, pp. 1–16, 2021.

[59] N. Spalatu, M. Krunks, and J. Hiie, "Structural and optoelectronic properties of CdCl2 activated CdTe thin films modified by multiple thermal annealing," *Thin Solid Films*, vol. 633, pp. 106–111, 2017, doi: 10.1016/j.tsf.2016.09.042.

[60] R. Dhere, T. Gessert, J. Zhou, S. Asher, J. Pankow, and H. Moutinho, "Investigation of CdZnTe for Thin-Film Tandem Solar Cell Applications," *Mater. Res. Soc. Symp. Proc.*, vol. 763, pp. 409–414, 2003, doi: 10.1557/proc-763-b8.25.

[61] Z. Bai and D. Wang, "Oxidation of CdTe thin film in air coated with and without a CdCl 2 layer," *Phys. Status Solidi Appl. Mater. Sci.*, vol. 209, no.

10, pp. 1982–1987, 2012, doi: 10.1002/pssa.201228107.

[62] A. Rohatgi, R. Sudharsanan, S. A. Ringel, and H. C. Chou, "High-Efficiency Cadmium Telluride and Zinc Telluride Based Thin-Film Solar Cells," Golden, Colorado, 1992.

[63] K. D. Dobson, I. Visoly-Fisher, G. Hodes, and D. Cahen, "Stability of CdTe/CdS thin-film solar cells," *Sol. Energy Mater. Sol. Cells*, vol. 62, no. 3, pp. 295–325, 2000, doi: 10.1016/S0927-0248(00)00014-3.

[64] S. G. Kumar and K. S. R. K. Rao, "Physics and chemistry of CdTe/CdS thin film heterojunction photovoltaic devices: Fundamental and critical aspects," *Energy Environ. Sci.*, vol. 7, no. 1, pp. 45–102, 2014, doi: 10.1039/c3ee41981a.

[65] Y. Waseda, E. Matsubara, and K. Shinoda, *X-Ray Diffraction Crystallography*. Berlin: Springer, 2011.

[66] O. Ueda and S. J. Pearton, *Materials and reliability handbook for semiconductor optical and electron devices*. New York: Springer, 2013.

[67] J. Álvarez-García, V. Izquierdo-Roca, and A. Pérez-Rodríguez, "Raman Spectroscopy on Thin Films for Solar Cells," in *Advanced Characterization Techniques for Thin Film Solar Cells*, 2011, pp. 365–386.

[68] E. Garcia-Caurel, A. De Martino, J. P. Gaston, and L. Yan, "Application of spectroscopic ellipsometry and mueller ellipsometry to optical characterization," *Appl. Spectrosc.*, vol. 67, no. 1, pp. 1–21, 2013, doi: 10.1366/12-06883.

[69] M. Losurdo *et al.*, "Spectroscopic ellipsometry and polarimetry for materials and systems analysis at the nanometer scale: State-of-the-art, potential, and perspectives," *J. Nanoparticle Res.*, vol. 11, no. 7, pp. 1521–1554, 2009, doi: 10.1007/s11051-009-9662-6.

[70] V. M. Airaksinen, *Silicon Wafer and Thin Film Measurements*. Elsevier Inc., 2015.

[71] H. G. Tompkins and E. A. Irene, *Handbook of Ellipsometry*. 2005.

[72] D. Abou-Ras, M. Nichterwitz, M. J. Romero, and S. S. Schmidt, "Electron

Microscopy on Thin Films for Solar Cells," in *Advanced Characterization Techniques for Thin Film Solar Cells*, vol. 1–2, 2016, pp. 371–420.

[73] Dieter K. Schroder, *Semiconductor Material and Device Characterization, Third Edition*. John Wiley & Sons, 2005.

[74] H. Xu, R. Xu, J. Huang, J. Zhang, K. Tang, and L. Wang, "The dependence of Zn content on thermal treatments for Cd 1-x Zn x Te thin films deposited by close-spaced sublimation," *Appl. Surf. Sci.*, vol. 305, no. June, pp. 477–480, 2014, doi: 10.1016/j.apsusc.2014.03.117.

[75] Y. V. Znamenshchykov *et al.*, "The surface morphology, structural properties and chemical composition of Cd1−xZnxTe polycrystalline thick films deposited by close spaced vacuum sublimation," *Mater. Sci. Semicond. Process.*, vol. 63, no. January, pp. 64–71, 2017, doi: 10.1016/j.mssp.2017.02.004.

[76] E. Yilmaz, E. Tuğay, A. Aktağ, I. Yildiz, M. Parlak, and R. Turan, "Surface morphology and depth profile study of Cd1-xZnxTe alloy nanostructures," *J. Alloys Compd.*, vol. 545, pp. 90–98, 2012, doi: 10.1016/j.jallcom.2012.08.028.

[77] I. M. Dharmadasa *et al.*, "Improvement of composition of CdTe thin films during heat treatment in the presence of CdCl2," *J. Mater. Sci. Mater. Electron.*, vol. 28, no. 3, pp. 2343–2352, 2017, doi: 10.1007/s10854-016-5802-9.

[78] D. Janardhana, S. N. Jayaramu, W. D. Roos, W. Purcell, and H. C. Swart, "Influences of substrate temperatures and oxygen partial pressures on the crystal structure, morphology and luminescence properties of pulsed laser deposited bi2o3:Ho3+ thin films," *Coatings*, vol. 10, no. 12, pp. 1–29, 2020, doi: 10.3390/coatings10121168.

[79] N. K. Das *et al.*, "Effect of substrate temperature on the properties of RF sputtered CdS thin films for solar cell applications," *Results Phys.*, vol. 17, no. January, pp. 0–7, 2020, doi: 10.1016/j.rinp.2020.103132.

[80] V. V. Artamonov, M. Y. Valakh, V. V. Strel'chuk, A. Baidullaeva, and P. E.

Mozol', "Raman scattering by tellurium films on CdTe single crystals," *J. Appl. Spectrosc.*, vol. 48, no. 6, pp. 653–655, 1988, doi: 10.1007/BF01133668.

[81]   S. A. Hawkins *et al.*, "Light-induced tellurium enrichment on CdZnTe crystal surfaces detected by Raman spectroscopy," *J. Electron. Mater.*, vol. 37, no. 9, pp. 1438–1443, 2008, doi: 10.1007/s11664-008-0448-x.

[82]   J. Huang *et al.*, "Growth and properties of CdZnTe films on different substrates," *Surf. Coatings Technol.*, vol. 364, no. October, pp. 444–448, 2019, doi: 10.1016/j.surfcoat.2018.10.083.

[83]   A. Medvid', N. Litovchenko, A. Mychko, and Y. Naseka, "Exciton quantum confinement in nanocones formed on a surface of CdZnTe solid solution by laser radiation," *Nanoscale Res. Lett.*, vol. 7, no. 1, pp. 1–4, 2012, doi: 10.1186/1556-276X-7-514.

[84]   F. A. Akgul, G. Akgul, H. H. Gullu, H. E. Unalan, and R. Turan, "Improved diode properties in zinc telluride thin film-silicon nanowire heterojunctions," *Philos. Mag.*, vol. 95, no. 11, pp. 1164–1183, 2015, doi: 10.1080/14786435.2015.1026296.

[85]   Y. Du *et al.*, "One-Dimensional van der Waals Material Tellurium: Raman Spectroscopy under Strain and Magneto-Transport," *Nano Lett.*, vol. 17, no. 6, pp. 3965–3973, 2017, doi: 10.1021/acs.nanolett.7b01717.

[86]   S. Khatun, A. Banerjee, and A. J. Pal, "Nonlayered tellurene as an elemental 2D topological insulator: Experimental evidence from scanning tunneling spectroscopy," *Nanoscale*, vol. 11, no. 8, pp. 3591–3598, 2019, doi: 10.1039/c8nr09760g.

[87]   L. C. Teague, S. A. Hawkins, M. C. Duff, M. Groza, V. Buliga, and A. Burger, "AFM characterization of raman laser-induced damage on CdZnTe crystal surfaces," *J. Electron. Mater.*, vol. 38, no. 8, pp. 1522–1527, 2009, doi: 10.1007/s11664-009-0763-x.

[88]   T. Çolakoğlu, M. Parlak, and S. Özder, "Investigation of optical parameters of Ag-In-Se thin films deposited by e-beam technique," *J. Non. Cryst. Solids*,

vol. 354, no. 30, pp. 3630–3636, 2008, doi: 10.1016/j.jnoncrysol.2008.03.014.

[89] S. Mathuri, K. Ramamurthi, and R. Ramesh Babu, "Effect of substrate temperature on the structural and optical properties of CdSe thin film deposited by electron beam evaporation technique," *J. Mater. Sci. Mater. Electron.*, vol. 5, no. 3, 2013, doi: 10.1007/s10854-016-4740-x.

[90] S. Shanmugan and D. Mutharasu, "Studies on morphological change and optical properties for various Zn concentrations in CdTe thin film prepared by stacked elemental layer method," *J. Alloys Compd.*, vol. 509, no. 5, pp. 2143–2148, 2011, doi: 10.1016/j.jallcom.2010.10.169.

[91] D. Geethalakshi and N. Muthukumarasamy, "Effect of annealing on structural and optical properties of CdTe Thin films," *J. Nanosci. Nanotechnol.*, vol. 1, no. 1, pp. 23–29, 2012, doi: 10.1007/978-3-319-29096-6_12.

[92] T. M. Shimpi *et al.*, "Effect of the cadmium chloride treatment on RF sputtered Cd 0.6Zn0.4Te films for application in multijunction solar cells," *J. Vac. Sci. Technol. A Vacuum, Surfaces, Film.*, vol. 34, no. 5, p. 051202, 2016, doi: 10.1116/1.4960979.

[93] D. E. Swanson *et al.*, "CdCl2 passivation of polycrystalline CdMgTe and CdZnTe absorbers for tandem photovoltaic cells," *J. Appl. Phys.*, vol. 123, no. 20, 2018, doi: 10.1063/1.5023811.

[94] I. M. Dharmadasa, "Review of the CdCl 2 treatment used in CdS/CdTe thin film solar cell development and new evidence towards improved understanding," *Coatings*, vol. 4, no. 2, pp. 282–307, 2014, doi: 10.3390/coatings4020282.

[95] I. M. Dharmadasa and A. A. Ojo, "Unravelling complex nature of CdS/CdTe based thin film solar cells," *J. Mater. Sci. Mater. Electron.*, vol. 28, no. 22, pp. 16598–16617, 2017, doi: 10.1007/s10854-017-7615-x.

[96] I. M. Dharmadasa *et al.*, "Fabrication of CdS/CdTe-based thin film solar cells using an electrochemical technique," *Coatings*, vol. 4, no. 3, pp. 380–415, 2014, doi: 10.3390/coatings4030380.

[97] T. A. Gessert, "Cadmium telluride photovoltaic thin film: CdTe," in

Comprehensive Renewable Energy, vol. 1, no. February, Elsevier Ltd., 2012, pp. 423–438.

[98]   S. Hofmann, *Auger- and X-Ray Photoelectron Spectroscopy in Material Science*. Springer, 2013.

[99]   J. A. Woollam, B. D. Johs, C. M. Herzinger, J. N. Hilfiker, R. A. Synowicki, and C. L. Bungay, "Overview of variable-angle spectroscopic ellipsometry (VASE): I. Basic theory and typical applications," *Opt. Metrol. A Crit. Rev.*, vol. 10294, p. 1029402, 1999, doi: 10.1117/12.351660.

[100]   L. A. de Montmorillon, P. Delaye, J. C. Launay, and G. Roosen, "Comparative study of CdTe and GaAs photorefractive performances from 1 μm to 1.55 μm," *Opt. Mater. (Amst).*, vol. 4, no. 2–3, pp. 233–236, 1995, doi: 10.1016/0925-3467(94)00065-4.

[101]   M. H. Engelhard, T. C. Droubay, and Y. Du, "X-ray photoelectron spectroscopy applications," *Encycl. Spectrosc. Spectrom.*, pp. 716–724, 2016, doi: 10.1016/B978-0-12-409547-2.12102-X.

[102]   J. C. Dupin, D. Gonbeau, P. Vinatier, and A. Levasseur, "Systematic XPS studies of metal oxides, hydroxides and peroxides," *Phys. Chem. Chem. Phys.*, vol. 2, no. 6, pp. 1319–1324, 2000, doi: 10.1039/a908800h.

[103]   H. Khallaf *et al.*, "Investigation of chemical bath deposition of CdO thin films using three different complexing agents," *Appl. Surf. Sci.*, vol. 257, no. 22, pp. 9237–9242, 2011, doi: 10.1016/j.apsusc.2011.04.060.

[104]   F. Debbagh, E. L. Ameziane, M. Azizan, M. Brunel, and T. T. A. Nguyen, "Some annealing effects on r.f. sputtered Cu/Te/CdTe structure," *Mater. Sci. Eng. B*, vol. 38, no. 3, pp. 223–227, 1996, doi: 10.1016/0921-5107(95)01442-X.

[105]   R. M. Krishna, "Crystal Growth , Characterization and Fabrication of CDZNTE-Based Nuclear Detectors," University of South Carolina, 2013.

[106]   M. Shen *et al.*, "Luminescent properties of CdTe quantum dots synthesized using 3-mercaptopropionic acid reduction of tellurium dioxide directly," *Nanoscale Res. Lett.*, vol. 8, no. 1, p. 1, 2013, doi: 10.1186/1556-276x-8-253.

[107] S. Adachi *et al.*, "Related content Optical Constants of Zn1-xCdxTe Ternary Alloys: Experiment and Modeling," *Jpn. J. Appl. Phys.*, vol. 32, no. 8R, p. 3496, 1993.

[108] S. Adachi and K. Sato, "Numerical derivative analysis of the pseudodielectric functions of znte," *Jpn. J. Appl. Phys.*, vol. 31, no. 12 R, pp. 3907–3912, 1992, doi: 10.1143/JJAP.31.3907.

[109] K. Sato and S. Adachi, "Optical properties of ZnTe," *J. Appl. Phys.*, vol. 73, no. 2, pp. 926–931, 1993, doi: 10.1063/1.353305.

[110] O. Castaing, J. T. Benhlal, R. Granger, and R. Triboulet, "Critical point parameters deduced from the dielectric function in HgZnTe and CdZnTe alloys," *J. Cryst. Growth*, vol. 159, no. 1–4, pp. 1112–1116, 1996, doi: 10.1016/0022-0248(95)00874-8.

[111] C. Zhou, H. Chung, X. Wang, and P. Bermel, "Design of CdZnTe and crystalline silicon tandem junction solar cells," *IEEE J. Photovoltaics*, vol. 6, no. 1, pp. 301–308, 2016, doi: 10.1109/JPHOTOV.2015.2481598.

[112] M. Koç, G. Kartopu, and S. Yerci, "Combined Optical-Electrical Optimization of Cd1-xZnxTe/Silicon Tandem Solar Cells," *Materials (Basel).*, vol. 13, no. 1860, pp. 1–16, 2020, doi: 10.3390/ma13081860.

[113] N. R. Paudel, K. A. Wieland, and A. D. Compaan, "Ultrathin CdS/CdTe solar cells by sputtering," *Sol. Energy Mater. Sol. Cells*, vol. 105, pp. 109–112, 2012, doi: 10.1016/j.solmat.2012.05.035.

[114] N. R. Paudel, K. A. Wieland, and A. D. Compaan, "Improvements in ultra-thin CdS/CdTe solar cells," in *37th photovoltaic specialists conference*, 2011, pp. 2784–2786.

[115] R. Keshav and M. G. Mahesha, "Investigation on performance of CdTe solar cells with CdS and bilayer ZnS/CdS windows grown by thermal evaporation technique," *Int. J. Energy Res.*, vol. 45, no. 5, pp. 7421–7435, 2021, doi: 10.1002/er.6325.

[116] H. W. Yao, J. C. Erickson, H. B. Barber, R. B. James, and H. Hermon, "Optical properties of Cd0.9Zn0.1Te studied by variable angle spectroscopic

ellipsometry between 0.75 and 6.24 eV," *J. Electron. Mater.*, vol. 28, no. 6, pp. 760–765, 1999, doi: 10.1007/s11664-999-0067-1.

[117] S. Chander and M. S. Dhaka, "Enhanced structural, electrical and optical properties of evaporated CdZnTe thin films deposited on different substrates," *Mater. Lett.*, vol. 186, no. August 2016, pp. 45–48, 2017, doi: 10.1016/j.matlet.2016.09.093.

[118] S. Chander and M. S. Dhaka, "Effect of thickness on physical properties of electron beam vacuum evaporated CdZnTe thin films for tandem solar cells," *Phys. E Low-Dimensional Syst. Nanostructures*, vol. 84, pp. 112–117, 2016, doi: 10.1016/j.physe.2016.05.045.

[119] D. M. Zeng, W. Q. Jie, H. Zhou, Y. G. Yang, and F. Chen, "Effect of film thickness on the structural and physical properties of CdZnTe thin films," *Adv. Mater. Res.*, vol. 194–196, pp. 2312–2316, 2011, doi: 10.4028/www.scientific.net/AMR.194-196.2312.

[120] S. J. Ikhmayies, "The influence of thickness on the optical parameters of thermally evaporated CdS thin films," in *TMS Annual Meeting*, 2014, pp. 383–390, doi: 10.1002/9781118889879.ch48.

[121] M. Powalla and D. Bonnet, "Thin-film solar cells based on the polycrystalline compound semiconductors CIS and CdTe," *Adv. Optoelectron.*, vol. 2007, 2007, doi: 10.1155/2007/97545.

[122] A. B. Pressman, "Electrical properties of Cadmium Telluride Thin Film Solar Cells Activated with Magnesium Chloride," University of Liverpool, 2017.

[123] K. Deka and M. P. C. Kalita, "Microstructure analysis of chemically synthesized wurtzite-type CdS nanocrystals," *Pramana - J. Phys.*, vol. 86, no. 5, pp. 1119–1126, 2016, doi: 10.1007/s12043-015-1132-3.

[124] S. S. Hegedus and W. N. Shafarman, "Thin-film solar cells: device measurements and analysis," *Prog. Photovoltaics Res. Appl.*, vol. 12, no. 23, pp. 155–176, 2004, doi: 10.1002/pip.518.

[125] A. Cantas *et al.*, "Importance of CdS buffer layer thickness on Cu2ZnSnS4-based solar cell efficiency," *J. Phys. D. Appl. Phys.*, vol. 51, no. 27, p. aac8d3,

2018, doi: 10.1088/1361-6463/aac8d3.

[126] R. W. Miles, K. M. Hynes, and I. Forbes, "Photovoltaic solar cells: An overview of state-of-the-art cell development and environmental issues," *Prog. Cryst. Growth Charact. Mater.*, vol. 51, no. 1–3, pp. 1–42, 2005, doi: 10.1016/j.pcrysgrow.2005.10.002.

[127] D. Bonnet and P. Meyers, "Cadmium-telluride - Material for thin film solar cells," *J. Mater. Res.*, vol. 13, no. 10, pp. 2740–2753, 1998, doi: 10.1557/JMR.1998.0376.

[128] L. Kosyachenko, "Efficiency of Thin-Film CdS/CdTe Solar Cells," in *Solar Energy*, no. February, Radu D. Rugescu, Ed. IntechOpen, 2010.

[129] M. Carmody and A. Gilmore, "High efficiency single crystal CdTe solar cells," *NREL Subcontract Rep.*, no. May, pp. 1–43, 2011.

[130] T. J. de Lyon, "CdZnTe on Si(001) and Si(112): Direct MBE Growth for Large-Area HgCdTe Infrared Focal-Plane Array Applications," *J. Electrochem. Soc.*, vol. 141, no. 10, p. 2888, 1994, doi: 10.1149/1.2059251.

[131] M. Niraula *et al.*, "MOVPE growth of thick single crystal CdZnTe epitaxial layers on Si substrates for nuclear radiation detector development," *IEEE Trans. Nucl. Sci.*, vol. 60, no. 4, pp. 2859–2863, 2013, doi: 10.1109/TNS.2013.2263841.

[132] D. Grecu, U. Jayamaha, G. Rich, and V. G. Karpov, "Admittance spectroscopy of CdTe-based solar cells," *Conf. Rec. IEEE Photovolt. Spec. Conf.*, pp. 680–683, 2000, doi: 10.1109/PVSC.2000.915957.

[133] Ö. B. Balbasi *et al.*, "CdZnTe bulk crystal growth and temperature modeling studies at METU-CGL," in *Proc. SPIE 10762, Hard X-Ray, Gamma-Ray, and Neutron Detector Physics XX, 107620R*, 2018, no. September 2018, p. 29, doi: 10.1117/12.2323409.

[134] S. M. Sze and D. C. Mattis, "Physics of Semiconductor Devices," *Phys. Today*, vol. 23, 1970, doi: 10.1063/1.3022205.

[135] A. A. Ojo, W. M. Cranton, and I. M. Dharmadasa, *Next Generation Multilayer Graded Bandgap Solar Cells*. Cham, Switzerland: Springer, 2019.

[136] F. E. Jones, B. P. Wood, J. A. Myers, C. Daniels-Hafer, and M. C. Lonergan, "Current transport and the role of barrier inhomogeneities at the high barrier n-InP | poly(pyrrole) interface," *J. Appl. Phys.*, vol. 86, no. 11, pp. 6431–6441, 1999, doi: 10.1063/1.371707.

[137] Ş. Aydoğan, M. Sağlam, and A. Türüt, "On the barrier inhomogeneities of polyaniline/p-Si/Al structure at low temperature," *Appl. Surf. Sci.*, vol. 250, no. 1–4, pp. 43–49, 2005, doi: 10.1016/j.apsusc.2004.12.020.

[138] C. Bozkaplan, A. Tombak, M. F. Genişel, Y. S. Ocak, and K. Akkilic, "The influence of substrate temperature on RF sputtered CdS thin films and CdS/p-Si heterojunctions," *Mater. Sci. Semicond. Process.*, vol. 58, no. October 2016, pp. 34–38, 2017, doi: 10.1016/j.mssp.2016.11.023.

[139] M. Terlemezoglu, O. Bayrakli, H. H. Güllü, T. Çolakoğlu, D. E. Yildiz, and M. Parlak, "Analysis of current conduction mechanism in CZTSSe/n-Si structure," *J. Mater. Sci. Mater. Electron.*, vol. 29, no. 7, pp. 5264–5274, 2018, doi: 10.1007/s10854-017-8490-1.

[140] H. H. Güllü, M. Terlemezoğlu, O. Bayrakli, D. E. Yildiz, and M. Parlak, "Investigation of carrier transport mechanisms in the Cu-Zn-Se based hetero-structure grown by sputtering technique," *Can. J. Phys.*, vol. 96, no. 7, pp. 816–825, 2018, doi: 10.1139/cjp-2017-0777.

[141] B. O. Sürücü, H. H. Güllü, M. Terlemezoglu, D. E. Yildiz, and M. Parlak, "Determination of current transport characteristics in Au-Cu/CuO/n-Si Schottky diodes," *Phys. B Condens. Matter*, vol. 570, no. June, pp. 246–253, 2019, doi: 10.1016/j.physb.2019.06.024.

[142] R. T. Tung, "Recent advances in Schottky barrier concepts," *Mater. Sci. Eng. R Reports*, vol. 35, no. 1–3, pp. 1–138, 2001, doi: 10.1016/S0927-796X(01)00037-7.

[143] R. T. Tung, "Electron transport at metal-semiconductor interfaces: General theory," *Phys. Rev. B*, vol. 45, no. 23, pp. 13509–13523, 1992, doi: 10.1103/PhysRevB.45.13509.

[144] R. C. Neville and J. J. Loferski, "Solar Energy Conversion: The Solar Cell,"

Phys. Today, vol. 35, no. 4, pp. 65–65, 1982, doi: 10.1063/1.2915018.

[145] A. Bothwell, "DEVELOPMENT AND ADVANCEMENT OF THIN CdTe-BASED SOLAR CELLS FOR PHOTOVOLTAIC PERFORMANCE IMPROVEMENTS," Colorado State University, 2020.

[146] N. Shukla and D. K. Dwivedi, "Dielectric relaxation and AC conductivity studies of Se90Cd10-xInx glassy alloys," *J. Asian Ceram. Soc.*, vol. 4, no. 2, pp. 178–184, 2016, doi: 10.1016/j.jascer.2016.02.003.

[147] Y. Badali, Ş. Altındal, and İ. Uslu, "Dielectric properties, electrical modulus and current transport mechanisms of Au/ZnO/n-Si structures," *Prog. Nat. Sci. Mater. Int.*, vol. 28, no. 3, pp. 325–331, 2018, doi: 10.1016/j.pnsc.2018.05.003.

[148] M. J. Deen and F. Pascal, "Electrical characterization of semiconductor materials and devices," *Springer Handbooks*, p. 1, 2017, doi: 10.1007/978-3-319-48933-9_20.

[149] L. C. Kimerling, "Influence of deep traps on the measurement of free-carrier distributions in semiconductors by junction capacitance techniques," *J. Appl. Phys.*, vol. 45, no. 4, pp. 1839–1845, 1974, doi: 10.1063/1.1663500.

[150] J. V. Li *et al.*, "Theoretical analysis of effects of deep level, back contact, and absorber thickness on capacitance-voltage profiling of CdTe thin-film solar cells," *Sol. Energy Mater. Sol. Cells*, vol. 100, no. May, pp. 126–131, 2012, doi: 10.1016/j.solmat.2012.01.003.

[151] J. S. Park, S. Kim, Z. Xie, and A. Walsh, "Point defect engineering in thin-film solar cells," *Nat. Rev. Mater.*, vol. 3, no. 7, pp. 194–210, 2018, doi: 10.1038/s41578-018-0026-7.

[152] Ş. Altindal, A. Tataroğlu, and I. Dökme, "Density of interface states, excess capacitance and series resistance in the metal-insulator-semiconductor (MIS) solar cells," *Sol. Energy Mater. Sol. Cells*, vol. 85, no. 3, pp. 345–358, 2005, doi: 10.1016/j.solmat.2004.05.004.

[153] J. Poortmans and V. Arkhipov, *Thin Film Solar Cells Fabrication, Characterization and Applications*. John Wiley and Sons, 2006.

[154] W. A. Hill and C. C. Coleman, "A single-frequency approximation for interface-state density determination," *Solid. State. Electron.*, vol. 23, no. 9, pp. 987–993, Sep. 1980, doi: 10.1016/0038-1101(80)90064-7.

[155] R. Engel-Herbert, Y. Hwang, and S. Stemmer, "Comparison of methods to quantify interface trap densities at dielectric/III-V semiconductor interfaces," *J. Appl. Phys.*, vol. 108, no. 12, 2010, doi: 10.1063/1.3520431.

[156] O. Rejaiba, A. F. Braña de Cal, and A. Matoussi, "A comprehensive study on the interface states in the ECR-PECVD SiO2/p-Si MOS structures analyzed by different method," *Phys. E Low-Dimensional Syst. Nanostructures*, vol. 109, no. January, pp. 84–92, 2019, doi: 10.1016/j.physe.2019.01.008.

[157] L. E. Black, *New Perspectives on Surface Passivation: Understanding the Si-Al2O3 Interface*. Switzerland: Springer International Publishing, 2016.

[158] A. Tataroğlu and Ş. Altindal, "Analysis of electrical characteristics of Au/SiO2/n-Si (MOS) capacitors using the high-low frequency capacitance and conductance methods," *Microelectron. Eng.*, vol. 85, no. 11, pp. 2256–2260, 2008, doi: 10.1016/j.mee.2008.07.001.

[159] R. J. Singh and R. S. Srivastava, "Distribution of surface states based on Hill and Coleman conductance technique," *Pramana*, vol. 18, no. 2, pp. 137–143, 1982, doi: 10.1007/BF02847983.

[160] Y. Chen *et al.*, "The Influence of Conduction Band Offset on CdTe Solar Cells," *J. Electron. Mater.*, vol. 47, no. 2, pp. 1201–1207, 2018, doi: 10.1007/s11664-017-5850-9.

CURRICULUM VITAE

PERSONAL INFORMATION

Surname, Name: Doğru Balbaşı, Çiğdem
Nationality: Turkish (TC)
Date and Place of Birth: 4 February 1988, Hatay
email: cdogru@metu.edu.tr

EDUCATION

Degree	Institution	Year of Graduation
MS	METU Physics	2015
BS	METU Physics Education	2012
High School	Hüseyin Özbuğday High School, Hatay	2005

WORK EXPERIENCE

Year	Place	Enrollment
2019-Present	METU MEMS CENTER	Senior Researcher
2014-2019	METU Physics Department	Research Assistant
2013-2014	METU Physics Department	Scientific Project Specialist

FOREIGN LANGUAGES

Advanced English, Beginner Arabic, Beginner Spanish.

AWARDS

June 2017	METU Ph.D. Course Performance Award (ODTÜ Doktora Programı Ders Performans Ödülü)
June 2012	Highest ranked student of Physics Education Department (ODTÜ Fizik Öğretmenliği Bölüm Birinciliği Ödülü)

PUBLICATIONS

1. Ö.B. Balbasi, Yasin Ergunt, **Ç. Doğru**, M. Kabukcuoglu, M. Ünal, M. Parlak and R. Turan., "CdZnTe bulk crystal growth and temperature modeling studies at METU-CGL," SPIE Proceedings Volume 10762, Hard X-Ray, Gamma-Ray, and Neutron Detector Physics XX; 107620R (2018).https://doi.org/10.1117/12.2323409.

2. M. Terlemezoglu, Ö. Bayraklı Sürücü, **C. Dogru**, H. H. Güllü, E. H. Ciftpinar, Ç. Erçelebi, and M. Parlak., "CZTSSe thin films fabricated by single step deposition for superstrate solar cell applications," J. Mater. Sci. Mater. Electron., pp. 1–6, (2019).

3. **C. Dogru Balbasi,** M. Terlemezoglu, H.H. Gullu, D.E. Yıldız, and M. Parlak., "Electrical characterization of CdZnTe/Si diode structure," Appl. Phys. A., 126, 614 (2020). https://doi.org/10.1007/s00339-020-03772-3.

4. **C. Dogru Balbasi** and M. Parlak. "Device Characterization of Thermally Evaporated CdS/CdZnTe Thin Films for Solar Cell Applications," IEEE Xplore Proceedings, International Conference on Photovoltaic Science and Technologies (PVCon) (2020).

POSTER PRESENTATIONS

1. **C. Dogru,** Ö. Bayraklı, M. Terlemezoglu and M. Parlak. "The Effect of $CdCl_2$ Treatment on CdZnTe Thin Films," European Materials Research Society-Spring Meeting, 2017.

2. **C. Dogru**, M. Terlemezoglu, Ö. Bayraklı, H. H. Güllü and M. Parlak. "The Effect of Substrate Temperature on CdZnTe thin films," European Materials Research Society-Spring Meeting, 2018.

3. **C. Dogru**, M. Terlemezoglu, Ö. Bayraklı, H.H. Güllü, M. Demir, M. Parlak. "Deposition and Characterization of CdZnTe Thin Films for Solar Cell Applications," International Conference on Photovoltaic Science and Technologies (PVCon), 2018.

4. **C. Dogru Balbasi** and M. Parlak. "Device Characterization of Thermally Evaporated CdS/CdZnTe Thin Films for Solar Cell Applications," International Conference on Photovoltaic Science and Technologies (PVCon), 2020.

HOBBIES

Watercolor painting, Origami, Yoga, Formula 1, Hiking, Cooking, Watching Movies.